TECHNISCHE
UNIVERSITÄT
WIEN
Vienna University of Technology

DIPLOMARBEIT

Optical Response of Superconducting Transmission Line Resonators

Ausgeführt am Atominstitut
der Technischen Universität Wien

unter der Anleitung von
Univ.-Prof. Dipl.-Ing. Dr. Hannes-Jörg Schmiedmayer
Dr. Johannes B. Majer

durch
Roman L. Voglauer
Sonnengasse 11
3161 St. Veit a. d. Gölsen

Wien, 11. September 2013 Roman Voglauer

Kurzfassung

Zu Beginn des letzten Jahrhunderts veränderte sich mit dem Aufkommen der Theorie der Quantenmechanik der Blick auf die Welt dramatisch. Gegenwärtig wird mit großem Aufwand versucht die besonderen Eigenschaften quantenmechanischer Zustände auch auf dem Gebiet der Informatik auszunutzen. Die Aufgabe besteht im Finden eines passenden Kandidaten für ein kohärent kontrollierbares "Qubit", das quantenmechanische Analogon zum klassischen Bit. Die Schwierigkeit besteht vor allem aufgrund der widersprüchlichen Anforderungen an ein solches Qubit. Auf der einen Seite wird ein gut isoliertes System benötigt, um Information langfristig zu speichern, auf der anderen Seite sollte ein Qubit natürlich auch leicht ansprechbar und manipulierbar sein. Eine Möglichkeit diese Bedingungen zu erfüllen bilden die sogenannten hybriden Quantensysteme, bei denen versucht wird unterschiedliche Quantensysteme geschickt zu kombinieren.

Der Ansatz unserer Gruppe ist es einen Defekt im Diamant (das NV^- Zentrum) mit anderen Quantensystem (z. B. ein supraleitendes Qubit) durch supraleitende Mikrowellenresonatoren zu verbinden. Das NV^- Zentrum würde hierbei als Langzeitspeicher fungieren wohingegen das supraleitende Qubit die Rolle einer schnellen Prozessoreinheit übernehmen würde. Da NV^- Zentren optisch in den Grundzustand gepumpt werden können, ist die Integration eines Lasers in den experimentellen Aufbau eine erstrebenswerte Erweiterung. Der Diamant wird in unseren Experimenten direkt auf dem supraleitenden Mikrowellenresonator platziert, daher ist es wesentlich den Einfluss des Lichtes auf die Resonatoren zu untersuchen.

In der vorliegenden Arbeit wird die optische Anregung von Quasiteilchen und Zwei-Niveau-System in supraleitenden Resonatoren erforscht. Die Eigenschaften der Mikrowellenresonatoren werden in Abhängigkeit von kontinuierlicher als auch gepulster Bestrahlung gemessen. Ausgewertet werden der Frequenz- und Phasenschub, die Änderung der Güte und der Amplitude aufgrund des Lichteinflusses. Besonders hervorzuheben sind die Messungen des zeitabhängigen Verhaltens von Zwei-Niveau-Systemen sowie des Anregungs- und Relaxationsprozesses von Quasiteilchen. Weiters wird auch die Auswirkung kontinuierlicher Bestrahlung mit dem Einfluss von Temperaturänderungen und auch der Mikrowellen-Messleistung verglichen.

Der nächste Schritt wird die Durchführung der gleichen Art von Experimenten mit einem Diamanten auf dem supraleitenden Mikrowellenresonator sein.

Abstract

At the beginning of the last century the theory of quantum mechanics radically changed the view of the physical world. Currently a lot of research is done trying to utilize the special properties of quantum mechanics for computation. The task is to find a suitable candidate for a coherently controllable "qubit", the quantum mechanical analog to a classical bit. One great difficulty lies in the diametrically opposed requirements for a well isolated system, to retain the stored information, on the one hand and an easily accessible system on the other hand. One possibility to reconcile those opposing needs are so-called hybrid quantum systems where different quantum systems are combined to fulfill both requirements at the same time.

In our group the goal is to connect a defect in diamond (the NV^-center) with another quantum system (e. g. a superconducting qubit) via superconducting microwave resonators. The NV^- center would serve as a long time quantum memory and the superconducting qubit as a fast processing unit. Since NV^-centers can be optically polarized into the ground state the integration of laser light is a worthwhile addition to our experimental setup. Given that the diamond sample is positioned directly on top of the superconducting microwave resonator it is of importance to investigate the impact of light onto the resonators.

In this master thesis we study the optical excitation of quasiparticles and two-level fluctuators (TLFs) inside superconducting resonators. Therefore, we measure the properties of superconducting resonators both under continuous and pulsed light irradiation. The findings are attained through measurements of the resonance frequency and phase shift, the change in quality factor and amplitude due to light exposure. The main results are the measurements of the time-dependent behavior of two-level fluctuator and quasiparticle excitation and relaxation processes. Furthermore we compare the influence of a continuous light flux with effects of a change in temperature or microwave probing power.

The next step will be to conduct the same type of experiments with a diamond sample mounted on the superconducting microwave resonator.

Contents

1. Introduction

> "I think I can safely say that nobody understands quantum mechanics."
> Richard Feynman

Unlike anything else, the theory of quantum mechanics challenged our perception of the world. Before the advent of quantum theory many physicists believed the overall framework of physics to be nearly completed. However, accumulating problems emerging from the classical theories, like e. g. the prediction of the ultraviolet catastrophe for black body radiation, forced physicist to abandon the classical picture and forge new ideas. The concepts of quantum mechanics, e. g. the wave-particle duality or the spin, are often difficult to grasp and sometimes simply counterintuitive, leading to quotes like the one mentioned above.

Today quantum mechanics plays an essential role in the understanding of the microscopic world, but only recently it started gaining importance in the field of computation and information processing. The research of the past decades has shown that the technical implementation of a "quantum" computer is challenging but the development of quantum algorithms might be even harder [NC10]. So why should we even care about quantum computation?

Not taking into account purely scientific reasons, quantum algorithms promise a substantial speed-up for certain computational tasks, e. g. integer factorization [Sho94] or searching an unstructured database [Gro96]. This increase of performance is all the more important since classically operating devices are on the brink of reaching physical dimensions where quantum effects come into play and further miniaturization is not feasible [NC10].

In analogy to the classical bit, the basic unit of information in a "quantum" computer is a quantum bit or in short "qubit". This qubit has to fulfill specific criteria [DiV00] in order to become a suitable candidate for quantum computation. The technical challenge arises from the conflicting requirements of those criteria. We want to be able to easily manipulate the qubit so that information can be written onto or read from this qubit. Then again we also want a well isolated qubit capable of storing quantum information for long times. This means as little interaction with the surrounding environment as possible, which is a direct contradiction to the first requirement.

From the attempt to reconcile those demands the concept of hybrid quantum systems has been developed. The basic idea is to use a combination of different quantum systems, rather than trying to fulfill all requirements with a single system.

Our approach is to use nitrogen-vacancy (NV^-) centers in diamond that we want to connect via superconducting coplanar waveguide (CPW) resonators to another qubit system, e. g. a superconducting qubit. The CPW resonators act as a bus system, transferring quantum information to and in between the different qubit systems. With regard to the previous paragraph, the NV^-center can be considered as the quantum memory responsible for the storage of information while the superconducting qubit would correspond to a fast quantum processor. What makes the NV^-center so interesting for quantum computation are the long coherence times even at room temperature and the ability to use the optical transitions to read out and polarize its spin state [Nöb13; Ams12]. This optical read-out of NV^-centers implies the introduction of laser light into the system. An important precondition is of course the knowledge about the consequences of the laser light on the other components of the hybrid quantum system.

The aim of this master thesis is to study the effects of laser irradiation on CPW resonators. To understand the response of CPW resonators to optical perturbations we will first start with the fundamentals of transmission line theory in the subsequent chapter before we then move on to microwave resonators in general and CPW resonators in particular in the third chapter. The next chapter treats the basic principles of superconductors. Chapters five and six will be devoted to the two most important mechanisms governing the resonator response, quasiparticle excitations and two-level fluctuators (TLFs). With that, the theory section of this thesis will be concluded and we turn to the description of the experimental setup in chapter seven. Subsequently, in chapter eight, the measurement results are gathered and discussed. At last the final chapter will provide a summary of the most significant results and offer a brief outlook at current and future developments regarding the work of this thesis.

2. Transmission line theory

When analyzing a circuit whose dimensions are small or of equal size compared to the electrical wavelength it is possible to think of this circuit as a sequence of individual components which are stacked together. The reason is that the phase difference of the electromagnetic fields in the circuit can be neglected, so that voltages and currents can be assigned to every point uniquely.[1]

However, if the circuit dimensions are on the order of the wavelength this picture of interconnected components breaks down and a different approach has to be taken. One possibility would be to solve Maxwell's equations for the whole circuit. Often this can be very time consuming as well as complicated and yields more information than is needed for most practical applications.

Because of this it is easier to analyze high frequency circuits with the aid of transmission line theory which can be seen either as an extension to circuit theory or a specialization of Maxwell's equation. The subsequent section will follow in a large part the treatment of Pozar [Poz11].

2.1. The lumped-element circuit model for transmission lines

Although transmission lines don't fulfill the aforementioned criterion to be much smaller than the wavelength they can be seen as a connection of many infinitesimal lumped elements of length Δz. In this case the familiar concept of resistors, conductances, capacitors and inductances as well as Kirchhoff's circuit laws can be reintroduced and applied. The lumped-element circuit model of a two-wire transmission line (see Fig. 2.1) consists of a series resistance R_l, a shunt conductance G_l, a series inductance L_l and a shunt capacitance C_l (these circuit elements are measured per unit length as indicated by the index l). R_l accounts for the losses due to finite conductivity of the conductors, while G_l represents the losses because of the dielectric in between the conductors. L_l describes the total self-inductance and C is the capacitance that arises due to the proximity of the two conductors. If we apply Kirchhoff's voltage and current law to the circuit and take the limit $\Delta z \to 0$ we receive the telegrapher equations

$$\frac{\partial v(z,t)}{\partial z} = -R_l i(z,t) - L_l \frac{\partial i(z,t)}{\partial t}\,, \tag{2.1}$$

$$\frac{\partial i(z,t)}{\partial z} = -G_l v(z,t) - C_l \frac{\partial v(z,t)}{\partial t}\,, \tag{2.2}$$

---

[1] A circuit with these properties can be described by Kirchhoff's circuit laws, which can be derived as the low-frequency limit of Maxwell's equations.

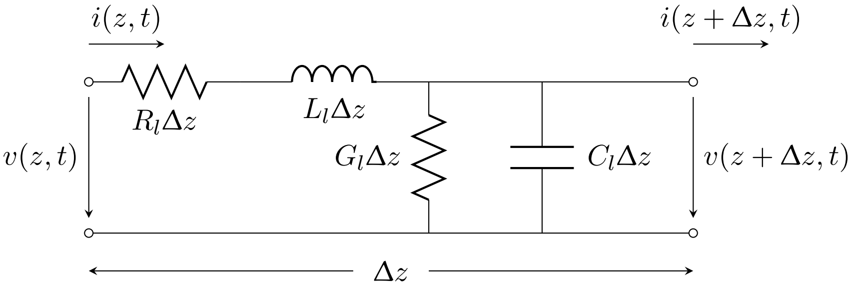

Figure 2.1.: Lumped-element equivalent circuit of a piece of transmission line with the length Δz. All circuit elements are measured per unit length. R_l describes the resistance due to the finite conductivity of both conductors, the conductance G_l represents dielectric losses, L_l is the total self-inductance of the short piece of transmission line and C_l is the capacitance between the two conductors. Applying Kirchhoff's circuit laws yields equations for the voltage $v(z,t)$ and current $i(z,t)$.

for the voltage $v(z,t)$ and the current $i(z,t)$. It is interesting to note that we could have gotten exactly the same result but starting out with Maxwell's equation instead of the lumped-element circuit model. By introducing cosine-based phasors[2] $V(z)$ and $I(z)$ the telegrapher equations can be transformed into wave equations for voltage and current

$$\frac{d^2V(z)}{dz^2} - \gamma^2 V(z) = 0\,, \tag{2.3}$$

$$\frac{d^2I(z)}{dz^2} - \gamma^2 I(z) = 0\,. \tag{2.4}$$

The complex propagation constant γ is given by

$$\gamma = \alpha + \mathrm{j}\beta = \sqrt{(R_l + \mathrm{j}\omega L_l)(G_l + \mathrm{j}\omega C_l)}\,, \tag{2.5}$$

where the real part α is the attenuation constant and the imaginary part β is called propagation constant or wave number. The propagation constant is dependent on the frequency f of the wave via the angular frequency $\omega = 2\pi f$. Solving Eq. (2.3) and (2.4), then inserting the solution into the phasor form of Eq. (2.1) and (2.2) leads to

$$V(z) = V_0^+ \mathrm{e}^{-\gamma z} + V_0^- \mathrm{e}^{\gamma z}\,, \tag{2.6}$$

$$I(z) = \frac{\gamma}{R_l + \mathrm{j}\omega L_l}\left(V_0^+ \mathrm{e}^{-\gamma z} - V_0^- \mathrm{e}^{\gamma z}\right)\,, \tag{2.7}$$

with a wave traveling in positive z-direction ($\propto \mathrm{e}^{-\gamma z}$) and one in negative z-direction ($\propto \mathrm{e}^{\gamma z}$). From this equation we can also determine the wavelength $\lambda = \frac{2\pi}{\beta}$ and the phase velocity $v_\mathrm{p} = \frac{\omega}{\beta} = \lambda f$ of the line.

---

[2] $v(z,t) = \mathrm{Re}[V(z)\mathrm{e}^{\mathrm{j}\omega t}]$ and $i(z,t) = \mathrm{Re}[I(z)\mathrm{e}^{\mathrm{j}\omega t}]$

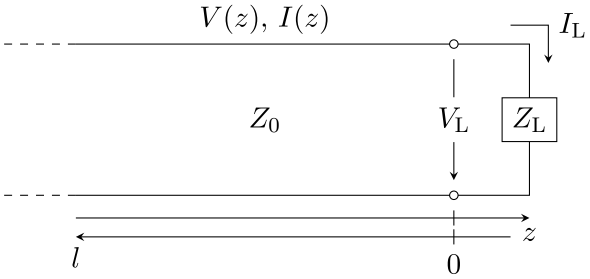

Figure 2.2.: A transmission line with a characteristic impedance Z_0 that is terminated with an arbitrary impedance Z_L. If $Z_\mathrm{L} \neq Z_0$ a part of an incoming wave $V_0^+ \mathrm{e}^{-\mathrm{j}\gamma z}$ will be reflected at $z = -l = 0$.

The ratio of voltage to current also allows us to define the characteristic impedance

$$Z_0 = \frac{R_l + \mathrm{j}\omega L_l}{\gamma} = \sqrt{\frac{R_l + \mathrm{j}\omega L_l}{G_l + \mathrm{j}\omega C_l}} \,. \tag{2.8}$$

For small losses or in the high frequency regime Eq. (2.8) can be approximated by

$$Z_0 \approx \sqrt{\frac{L_l}{C_l}} \,. \tag{2.9}$$

2.2. The terminated transmission line

If a transmission line with a characteristic impedance Z_0 is terminated by a load impedance Z_L (see Fig. 2.2) an incoming wave $V_0^+ \mathrm{e}^{-\mathrm{j}\gamma z}$ will be reflected at $z = -l = 0$, unless $Z_\mathrm{L} = Z_0$. This can easily be seen from the definition of the impedance $Z(z) = V(z)/I(z)$. At $z = 0$ the impedance has to be $Z_\mathrm{L} = V(0)/I(0) = \frac{V_0^+ + V_0^-}{V_0^+ - V_0^-} Z_0$. No reflections implies $V_0^- = 0$ which then yields $Z_\mathrm{L} = Z_0$.

For arbitrary load impedances Z_L the input impedance at a distance l from the load can be expressed as[3]

$$Z(l) = \frac{Z_\mathrm{L} + Z_0 \tanh(\gamma l)}{Z_0 + Z_\mathrm{L} \tanh(\gamma l)} Z_0 \,. \tag{2.10}$$

2.3. The scattering matrix

When dealing with microwave networks and transmission lines the direct measurement of voltages and currents can prove very difficult because the magnitude and phase of traveling or standing waves have to be obtained. Another complication arises from the

---

[3] We get Eq. (2.10) by expressing the ratio V_0^+/V_0^- through the impedances Z_L and Z_0 and substituting $z = -l$.

fact that unique voltages and currents can only be defined for transverse electromagnetic (TEM) waves [Poz11]. Therefore, a more suitable picture is to consider incident and reflected waves and measuring transmission and reflection coefficients. This is what the scattering matrix S represents, it connects the reflected voltage amplitudes with the incident ones.

Suppose we have a network with N ports[4] then the incoming voltage amplitudes V_n^+ of port n and the outbound amplitudes V_n^- would be connected via

$$\begin{pmatrix} V_1^- \\ V_2^- \\ \vdots \\ V_N^- \end{pmatrix} = \begin{pmatrix} S_{11} & S_{12} & \cdots & S_{1N} \\ S_{21} & S_{22} & \cdots & S_{2N} \\ \vdots & \vdots & \ddots & \vdots \\ S_{N1} & S_{N2} & \cdots & S_{NN} \end{pmatrix} \cdot \begin{pmatrix} V_1^+ \\ V_2^+ \\ \vdots \\ V_N^+ \end{pmatrix} . \tag{2.11}$$

From Eq. (2.11) we see that the elements of the S-matrix can be obtained by calculating

$$S_{ij} = \left. \frac{V_i^-}{V_j^+} \right|_{V_k^+ = 0 \text{ for } k \neq j} . \tag{2.12}$$

According to this definition the scattering matrix element for transmission from first to the second port is given by S_{21}.

---

[4] A port means a two-terminal pair.

3. Microwave resonators

Today microwave resonators are present in numerous devices like filters and oscillators. In the research area superconducting microwave resonators have attracted a lot of interest in recent years mainly because of their use as photon detectors for astronomy [Day+03] and as a “quantum bus” to read out or transfer quantum information in the field of circuit quantum electrodynamics [Wal+04; Maj+07].

Starting from a parallel resonant circuit the upcoming sections will explain the fundamentals of superconducting coplanar waveguide resonators, which are used in our experiments. A good review of superconducting microresonators is given by Zmuidzinas [Zmu12].

3.1. Parallel resonant circuit

As can be seen from Fig. 3.1 the parallel resonant circuit consists of a resistor R, an inductor L and a capacitor C. The input impedance of this resonator is given by

$$Z(\omega) = \left(\frac{1}{R} + \mathrm{j}\left(\omega C - \frac{1}{\omega L}\right)\right)^{-1} , \tag{3.1}$$

and average power delivered to the circuit can be calculated via

$$P_\mathrm{loss}(\omega) = \frac{1}{2}\,\mathrm{Re}\left[VI^*\right] = \frac{1}{2}\,\mathrm{Re}\left[|V|^2\left(\frac{1}{R} + \mathrm{j}\left(\frac{1}{\omega L} - \omega C\right)\right)\right] = \frac{1}{2}\frac{|V|^2}{R} . \tag{3.2}$$

The complex fraction that appears in Eq. (3.2) stems from the electric and magnetic energy which is stored in the capacitor and the inductor [Poz11]:

$$W_\mathrm{e} = \frac{1}{4}|V|^2 C , \tag{3.3}$$

$$W_\mathrm{m} = \frac{1}{4}\frac{|V|^2}{\omega^2 L} . \tag{3.4}$$

When the magnetic energy equals the electric energy, the circuit is on resonance and energy will periodically oscillate between capacitor and inductor. With the condition $W_\mathrm{e} = W_\mathrm{m}$ we obtain the resonance frequency[1]

$$\omega_0 = \frac{1}{\sqrt{LC}} , \tag{3.5}$$

---

[1] Although strictly speaking f_0 is the resonance frequency, since the difference is just a factor of 2π, we won’t really distinguish between a frequency f and the corresponding angular frequency $\omega = 2\pi f$.

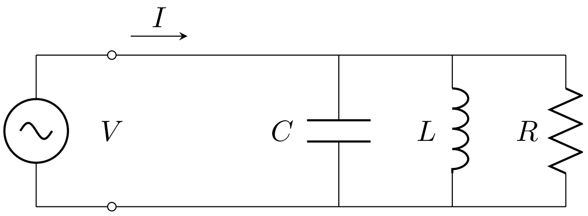

Figure 3.1.: A parallel RLC resonant circuit.

where the power P_{loss}, which is dissipated at the resistor R, exhibits a maximum (see Fig. 3.2). Another property to characterize resonators is the quality factor

$$Q = \omega \frac{W_{\mathrm{stored}}}{P_{\mathrm{loss}}}\,, \tag{3.6}$$

which is proportional to the ratio of the electric and magnetic energy stored in the circuit to the energy loss per second. Due to its definition the quality factor describes the number of oscillations between magnetic and electric field until the stored energy drops to 1/e of its original value. At resonance, where $W_{\mathrm{stored}} = W_{\mathrm{e}} + W_{\mathrm{m}} = 2W_{\mathrm{m}}$, Eq. (3.6) becomes

$$Q_{\mathrm{int}} = \frac{R}{\omega_0 L} = \omega_0 RC\,, \tag{3.7}$$

and is called unloaded or internal quality factor of the resonant circuit. The internal quality factor contains many different loss channels of the resonator. The most important ones are the dielectric loss due to damping of oscillating dipole moments, radiative loss, quasiparticle excitation and two-level fluctuator loss. Since we are especially interested in the last two loss mechanisms they will be explained in detail in Ch. 5 and 6. When the circuit is connected to some external circuitry the total quality factor of the complete circuit will be lowered because of additional losses and can be expressed as

$$\frac{1}{Q_{\mathrm{tot}}} = \frac{1}{Q_{\mathrm{int}}} + \frac{1}{Q_{\mathrm{ext}}}\,. \tag{3.8}$$

From the internal and external quality factor we can define the coupling coefficient $g = Q_{\mathrm{int}}/Q_{\mathrm{ext}}$ and distinguish three cases [Poz11]:

- $g < 1$: the resonator is *undercoupled* which means that internal losses dominate.
- $g = 1$: the resonator is *critically coupled*, at the resonance frequency the resonator's impedance is matched to the external circuit and maximum power can be transferred.
- $g > 1$: the resonator is *overcoupled*, meaning that the loss is primarily determined by the coupling to the external circuitry.

The reason why we started the description of microwave resonators with a parallel RLC lumped element resonator is that near the resonance frequency a transmission line

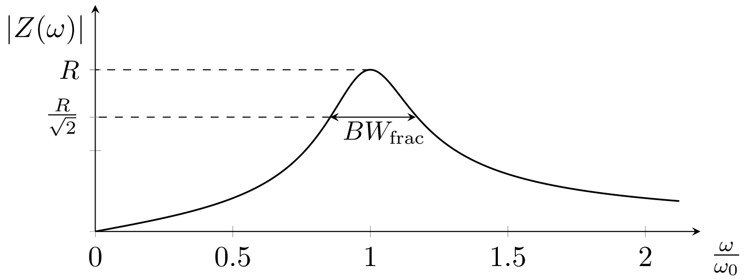

Figure 3.2.: The plot shows the magnitude of the impedance $Z(\omega)$ of the parallel resonant circuit from Fig. 3.1 near the resonance frequency ω_0. The frequency interval where $P_{\mathrm{loss}} = \frac{P_{\mathrm{max}}}{2}$ is called the half-power fractional bandwidth BW_{frac} (see Appendix B).

resonator can be represented by a parallel resonant circuit. At frequencies $\omega = \omega_0 + \Delta\omega$, where $\Delta\omega$ is small, a Taylor expansion for the impedance (see Appendix B) from Eq. (3.1) yields

$$Z \approx \frac{R}{1 + 2\mathrm{j}\Delta\omega RC} = \frac{R}{1 + 2\mathrm{j}Q_{\mathrm{int}}\Delta\omega/\omega_0}\,, \tag{3.9}$$

and as we will see in the subsequent section this is very similar to the expression derived for transmission line resonators.

3.2. Half wave transmission line resonator

In Section 2.2 we have seen that impedance mismatches at the end of a transmission line will cause reflections which lead to the formation of standing waves on the line. If there are mismatches on both ends of the line, a transmission line resonator is formed.

For an open-circuited transmission line the load impedance $Z_{\mathrm{L}} = \infty$ and Eq. (2.10) simplifies to

$$Z(l) = Z_0 \coth\left((\alpha + \mathrm{j}\beta)\, l\right) = Z_0 \frac{1 + \mathrm{j}\tan\beta l \tanh\alpha l}{\tanh\alpha l + \mathrm{j}\tan\beta l}\,, \tag{3.10}$$

in the last step we have applied the addition theorem for coth to separate α and β.

If we consider a low-loss transmission line resonator of length $l = \lambda/2$, close to resonance $\omega = \omega_0 + \Delta\omega$ Eq. (3.10) can be expanded similar to Eq. (3.9), which results in[2]

$$Z \approx \frac{Z_0}{\alpha l + \mathrm{j}\pi\Delta\omega/\omega_0}\,. \tag{3.11}$$

Comparing this expression with Eq. (3.9) illustrates why it is possible to model a transmission line resonator with a parallel lumped element resonator. From this comparison we can also extract the relations between the lumped element parameters and

---

[2] The assumptions to get this equation are small losses, so that $\tanh\alpha l \approx \alpha l$, and ω close to resonance, so that $\tan\beta l = \tan\beta\lambda/2 = \tan\left(\pi + \frac{\Delta\omega\pi}{\omega_0}\right) = \tan\frac{\Delta\omega\pi}{\omega_0} \approx \frac{\Delta\omega\pi}{\omega_0}$. Finally, taking only the first order of the expansion eliminates the imaginary part of the numerator and we get Eq. (3.11).

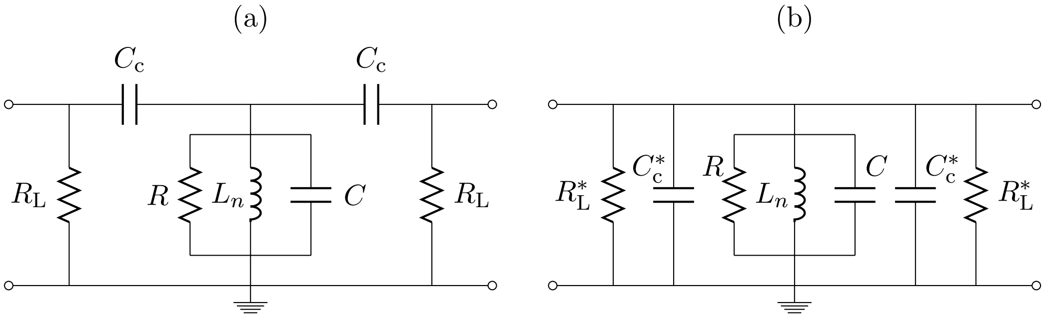

Figure 3.3.: (a) Parallel RLC circuit representation of a symmetrically coupled transmission line resonator with coupling capacitance C_c (b) and the corresponding Norton equivalent circuit.

the transmission line parameters[3] [Göp+08; Ams12]

$$R = \frac{Z_0}{\alpha l}\,, \quad C = \frac{C_l l}{2}\,, \quad L_n = \frac{2 L_l l}{n^2 \pi^2}\,, \quad Q_{\text{int}} = \frac{n\pi}{2\alpha l}\,. \tag{3.12}$$

The natural number n in the last two equations considers the fact that not only the fundamental resonance frequency $\omega = \omega_0$, but also higher harmonics $\omega = n\omega_0$ can be excited on a half wave transmission line resonator. The coupling of the resonator to a transmission line can be introduced via coupling capacitors C_c and load resistors R_L (see Fig. 3.3). The effects on the overall quality factor Q_{tot} can best be described after the transformation to the Norton equivalent circuit shown in Fig. 3.3(b), where $R_L^* = \frac{1+\omega_n^2 C_c^2 R_L^2}{\omega_n^2 C_c^2 R_L}$ and $C_c^* = \frac{C_c}{1+\omega_n^2 C_c^2 R_L^2}$. Since the total resistance is now given by $R_{\text{tot}} = (1/R + 2/R_L^*)^{-1}$ and the capacitance is $C_{\text{tot}} = C + 2C_c^*$ the resulting quality factor is

$$Q_{\text{tot}} = \omega_n^* R_{\text{tot}} C_{\text{tot}} = \omega_n^* \frac{C + 2C_c^*}{1/R + 2/R_L^*} \approx \omega_n \frac{C}{1/R + 2/R_L^*}\,, \tag{3.13}$$

with $\omega_n^* = 1/\sqrt{L_n\,(C + 2C_c^*)}$. The approximation in Eq. (3.13) is valid if the coupling capacitance is small in comparison with the capacitance of the resonator. From Eq. (3.8) the external quality factor is then determined by $Q_{\text{ext}} = \omega_n R_L^* C/2$.

3.3. Scattering parameter S_{21} of a transmission line resonator

Since we won't measure impedances but scattering parameters in the experiment, we will now derive an expression for S_{21}. Circuit theory tells us that the scattering parameter S_{21} of a two-port network (see Fig. 3.4) with a parallel impedance Z and characteristic impedances Z_0 is [Poz11]

$$S_{21} = \frac{2Z}{2Z + Z_0}\,. \tag{3.14}$$

---

[3] See Appendix C.

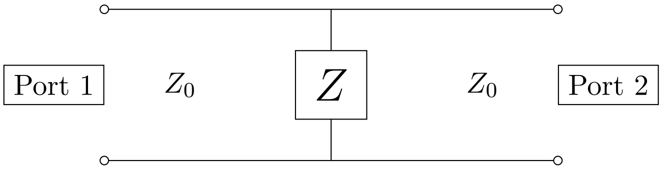

Figure 3.4.: For a two-port network consisting of a parallel impedance Z connected to two transmission lines with a characteristic impedance Z_0 the scattering parameter S_{21} can be written as $S_{21} = \frac{2Z}{2Z+Z_0}$ [Poz11].

With the results from the last section the impedance of the capacitively coupled resonator from Fig. 3.3 reads

$$Z = \frac{R_{\text{tot}}}{1 + 2\text{j}Q_{\text{tot}}\Delta\omega^*/\omega_n^*} \tag{3.15}$$

$$= \frac{R_{\text{tot}}\left(1 - 2\text{j}Q_{\text{tot}}\Delta\omega^*/\omega_n^*\right)}{1 + 4Q_{\text{tot}}^2(\Delta\omega^*/\omega_n^*)^2}\,. \tag{3.16}$$

Due to the small coupling capacitance C_c the Norton equivalent resistance R_L^* will be very large so that $R_{\text{tot}} \approx R$, $\omega_n^* \approx \omega_n$ and

$$Z \approx \frac{R\left(1 - 2\text{j}Q_{\text{tot}}\Delta\omega/\omega_n\right)}{1 + 4Q_{\text{tot}}^2(\Delta\omega/\omega_n)^2}\,. \tag{3.17}$$

Near the resonance frequency the denominator will be close to one because $\frac{\Delta\omega^2}{\omega_n^2} \ll 1$,

$$Z \approx R\left(1 - 2\text{j}Q_{\text{tot}}\Delta\omega/\omega_n\right)\,. \tag{3.18}$$

With the condition that from the resonator the characteristic impedance of the line looks like $Z_0 = R_\text{L}^*$ and remembering the relations for the quality factors

$$Q_{\text{int}} = \omega_n RC\,, \tag{3.19}$$

$$Q_{\text{ext}} = \frac{\omega_n R_\text{L}^* C}{2}\,, \tag{3.20}$$

we can express Z_0 as a ratio of internal and external quality factors

$$Z_0 = \frac{2Q_{\text{ext}}}{\omega_n C} = \frac{2Q_{\text{ext}}}{Q_{\text{int}}}R\,. \tag{3.21}$$

Inserting Eq. (3.18) and (3.21) into Eq. (3.14) yields

$$S_{21} = \frac{2R\left(1 - 2\text{j}Q_{\text{tot}}\Delta\omega/\omega_n\right)}{2R\left(1 - 2\text{j}Q_{\text{tot}}\Delta\omega/\omega_n\right) + 2RQ_{\text{ext}}/Q_{\text{int}}} \tag{3.22}$$

$$= \frac{1 - 2\text{j}Q_{\text{tot}}\Delta\omega/\omega_n}{1 + Q_{\text{ext}}/Q_{\text{int}} - 2\text{j}Q_{\text{tot}}\Delta\omega/\omega_n} \tag{3.23}$$

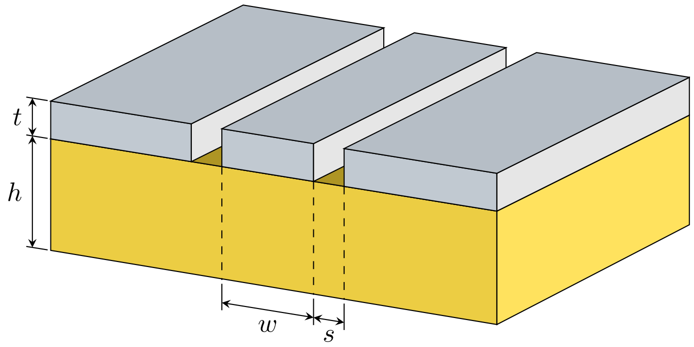

Figure 3.5.: A short piece of a coplanar waveguide (CPW) on a substrate (yellow) with a dielectric constant ϵ_r and height h. The superconducting film has a thickness t and a central conductor of width w which is separated from the ground planes by the distance s.

On resonance, characterized by $\Delta\omega = 0$, the transmission and also the scattering parameter exhibits a maximum giving the important result

$$S_{21}(\Delta\omega = 0) = S_{21}^{\mathrm{max}} = \frac{Q_{\mathrm{int}}}{Q_{\mathrm{int}} + Q_{\mathrm{ext}}}\,. \tag{3.24}$$

Substituting the fraction with S_{21}^{max} in Eq. (3.23) eventually leads to

$$S_{21} = \frac{1 + 2\mathrm{j}Q_{\mathrm{tot}}\Delta\omega/\omega_n}{1/S_{21}^{\mathrm{max}} + 2\mathrm{j}Q_{\mathrm{tot}}\Delta\omega/\omega_n}\,. \tag{3.25}$$

3.4. Coplanar waveguide resonator

In the previous sections the fundamental concepts of transmission line resonators have been discussed but until now we have not considered a specific transmission line geometry. The actual design we use for our $\lambda/2$-resonator[4] is a $12 \times 4\,\mathrm{mm}$ coplanar waveguide (CPW) structure[5] depicted in Fig. 3.5 and 3.6. A niobium film[6] of 200 nm is deposited on a sapphire substrate, which has a dielectric constant $\epsilon_\mathrm{r} = 10.4$ and a relative permeability $\mu_\mathrm{r} = 1$. The central conductor has a length $l = 21.571\,\mathrm{mm}$, a width $w = 10\,\mathrm{\mu m}$ and is separated from the ground planes by a gap $s = 4.15\,\mathrm{\mu m}$. These specific values of w and s ensure a $50\,\Omega$ impedance.The coupling capacitors are simple gap capacitors with a spacing of $s_c = 5\,\mathrm{\mu m}$ resulting in an input and output capacitance of $C_\mathrm{c} = 0.45\,\mathrm{fF}$. Due to the very small coupling capacitance the resonator is *undercoupled*, so that the loss is primarily determined by the internal losses, which we want to study. All these parameters lead to a designed resonance frequency at

---

[4] Model number: R3-3-111-1

[5] The coplanar waveguide design was first proposed by Wen in 1969 [Wen69].

[6] The niobium layer will be in the superconducting state for all measurements, since we are always below the critical temperature $T_\mathrm{c} = 9.2\,\mathrm{K}$.

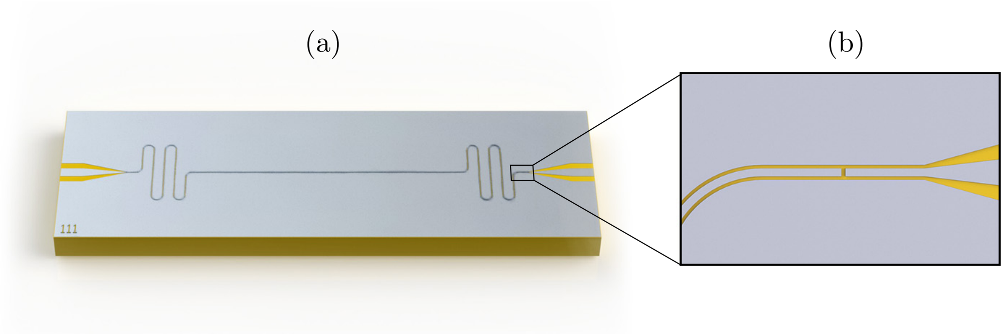

Figure 3.6.: (a) A rendering of the actual design of the resonator and (b) the magnification of the coupling capacitance C_c. The color code has been chosen in accordance with Fig. 3.5.

$f_0 = 2.87\,\mathrm{GHz}$. More details concerning the fabrication process can by found in the thesis of Koller [Kol12].

As indicated above the three dimensional geometry of coplanar waveguides will entail deviations from "ideal" transmission lines ("ideal" in the sense that the components have no physical dimension except for a length l). Due to their asymmetric composition with respect to the superconducting layer[7] a CPW will not support TEM modes anymore. The dielectric will cause an electromagnetic field traveling in the direction of the central conductor to exhibit longitudinal components. Luckily in the microwave regime these components are small enough so that they can be neglected [Gao08]. In the lossless case this so-called quasi-TEM approximation enables us to express an effective dielectric constant ϵ_eff, the phase velocity v_p and the characteristic impedance Z_0 [CC97]

$$\epsilon_\mathrm{eff} = \frac{C_l}{C_l^0}\,, \quad v_\mathrm{p} = \frac{c}{\epsilon_\mathrm{eff}} \quad \text{and} \quad Z_0 = \frac{1}{C_l v_\mathrm{p}}\,, \tag{3.26}$$

in terms of the capacitance per unit length C_l, capacitance per unit length without any dielectric C_l^0 and the speed of light in vacuum c.

The capacitance can be calculated via conformal mapping techniques. The basic idea is to map the geometry of our coplanar waveguide onto another geometry where it is easier to solve the problem. For a CPW similar to Fig. 3.5 – but with two semi-infinite ground planes, where the lower half space is filled with a dielectric ϵ_sub and the upper with ϵ_top and an infinitely thin superconducting layer – the capacitance and inductance can be derived as [Sim04; Gao08]

$$C_l = \epsilon_0 \epsilon_\mathrm{eff} \frac{4K(k)}{K(k')}\,, \tag{3.27}$$

$$L_l = \mu_0 \frac{K(k)}{4K(k')}\,, \tag{3.28}$$

---

[7] Above there is no dielectric, while below there is the sapphire substrate.

where K is the complete elliptic integral of the first kind [AS64], $k = \frac{w}{w+2s}$, $k' = \sqrt{1-k^2}$, μ_0 is the vacuum permeability and the effective dielectric constant is given by $\epsilon_{\text{eff}} = \left(\epsilon_{\text{sub}} + \epsilon_{\text{top}}\right)/2 \approx \left(\epsilon_{\text{sub}} + 1\right)/2$ (in our case there is no upper dielectric). The validity of these approximations for our designs has been confirmed in previous experiments [Kol12].

For a more detailed treatment of coplanar waveguides on dielectrics with finite thickness, finite ground planes, etc. we refer to Simons [Sim04].

Additionally to the geometry dependent changes we have to consider the effects of niobium in the superconducting state. As it turns out the superconducting charge carriers, the Cooper pairs, give rise to an extra term in the inductance, the so-called kinetic inductance, which will be the topic of the next chapter.

4. Kinetic inductance of a superconductor

In the treatment up to now, we mostly worked with ideal or low-loss conductors whereas the superconducting nature of the resonator material has been neglected. However, some aspects of superconducting materials like the kinetic inductance can play an important role in superconducting resonators.

Ideally, any electric or magnetic field should be expelled from the inside of the superconductor. In practice, those fields will not immediately drop to zero at the surface of a superconductor, but instead penetrate into the superconductor on a small length scale. The aim of this chapter is to look at the consequences arising from those non-vanishing fields inside the superconductor.

If electromagnetic fields didn't penetrate into niobium film the total inductance L_l^{tot} would be equal to the inductance L_l calculated in Eq. (3.28).[1] However, as we have just mentioned for every superconductor the fields extend into the medium with a characteristic penetration depth λ_{eff} that depends e. g. on temperature, the frequency of the fields and the geometry. The intruding field will exert a force on the charge carriers, which accelerates them and thereby adds kinetic energy to the system.

It can be shown that the additional kinetic energy acts like an additional series inductance [MT69; Ham11].[2] Any variation in the Cooper pair density will therefore also affect the inductance of a CPW resonator. The inductance can be split into two parts, a fixed one that arises from the geometry dependent magnetic field of the resonator and a variable one that stems from the kinetic energy of Cooper pairs near the surface

$$L_l^{\mathrm{tot}} = L_l^{\mathrm{m}} + L_l^{\mathrm{ki}} \,. \tag{4.1}$$

The field outside of the superconductor very closely resembles the field of a perfect conductor (which has an infinitely small penetration depth) so that $L_l^{\mathrm{m}} \approx L_l$ [Gao08], with L_l from Eq. (3.28). For $\lambda/2$-resonators similar to ours Frunzio et al. [Fru+05] have found ratios of $L_l^{\mathrm{ki}}/L_l^{\mathrm{m}} \approx 4\%$.

Often it is common not to consider the kinetic inductance itself but the kinetic inductance fraction

$$\alpha = \frac{L_l^{\mathrm{ki}}}{L_l^{\mathrm{tot}}} \,. \tag{4.2}$$

Kinetic inductance also occurs in normal conducting materials, but due to the resistance and therefore the small drift velocity of electrons it is usually negligible compared

---

[1] Note that the conformal mapping techniques used to calculate L_l use the approximation of a perfect conductor and therefore an infinitely small penetration depth.

[2] See also Appendix E, where this behavior is illustrated by looking at the kinetic inductance of a simple wire.

to the magnetic inductance [Her96; MT69].[3]

To actually calculate the kinetic impedance L_l^{ki} and the kinetic inductance fraction α the subsequent sections will feature a short review of the theory of superconductivity and introduce the surface impedance concept of superconductors.

4.1. Introduction to the theory of superconductivity

The response of a superconductor to external fields is governed by the relation between the London penetration depth λ_{L}^0 at absolute zero, the Pippard coherence length for pure superconductors ξ_0 and the electron mean free path l_{e}. According to Tinkham [Tin96] ξ_0 represents the minimal size of a Cooper pair and is the analog to the mean free path l_{e} for normal metals.

If $\xi_0 \ll \lambda_{\mathrm{L}}^0$ or $l_{\mathrm{e}} \ll \lambda_{\mathrm{L}}^0$ the field seen by a superconducting or normal charge carrier is more or less constant over the length of a Cooper pair and we can expect a local relationship between superconducting current density $\boldsymbol{J_s}$ and the electric field $\boldsymbol{E}$.[4] With the assumption of the two-fluid model (see Appendix D), $\boldsymbol{J_s}$ is given by the famous London equations [LL35]

$$\boldsymbol{J_s} = \frac{1}{\mathrm{j}\omega\mu_0\lambda_{\mathrm{L}}^2}\boldsymbol{E}\,, \tag{4.3}$$

$$\nabla \times \boldsymbol{J_s} = -\frac{1}{\lambda_{\mathrm{L}}^2}\boldsymbol{H}\,, \tag{4.4}$$

where μ_0 is the vacuum permeability, λ_{L} the London penetration depth and $\boldsymbol{H}$ the magnetic field. The first equation describes the perfect conductor property of superconductors while the second equation illustrates the expulsion of the magnetic field (the Meissner effect). The field decays exponentially from the surface into the superconductor on a length scale corresponding to the penetration depth λ_{L}, which for zero Kelvin can be expressed as

$$\lambda_{\mathrm{L}}^0 = \lambda_{\mathrm{L}}\left(T = 0\right) = \sqrt{\frac{m}{\mu_0 n_{\mathrm{se}} e^2}}\,, \tag{4.5}$$

with the mass of the electron m and the density of superconducting electrons n_{se}. However experiments show that the penetration depth always seems to be larger than λ_{L}.

Especially if $\xi_0 \gg \lambda_{\mathrm{L}}^0$ and $l_{\mathrm{e}} \gg \lambda_{\mathrm{L}}^0$, which is the case for clean superconductors at low temperatures, the local model breaks down and Eq. (4.3) and (4.4) have to be replaced with a phenomenological non-local relation [Pip53]

$$\boldsymbol{J_s}(\boldsymbol{r}) = \frac{3}{4\pi\xi_0\lambda_{\mathrm{L}}^2}\int_V \frac{\boldsymbol{R}\left(\boldsymbol{R}\cdot\boldsymbol{A}(\boldsymbol{r}')\right)\mathrm{e}^{-R/\xi}}{R^4}\,\mathrm{d}V'\,, \tag{4.6}$$

---

[3] For a detailed explanation we refer to Appendix E.

[4] In the literature there exist slightly different definitions for the local as well as the later following non-local regime, we follow the one outlined in Gao's thesis [Gao08].

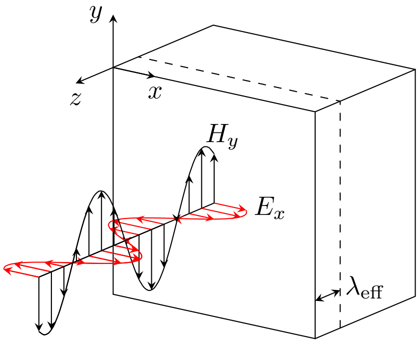

Figure 4.1.: A superconductor with an incident electromagnetic wave. After a penetration depth λ_{eff} the magnitude of $H_y(z)$ drops by a factor of e compared to $H_y(0)$. The same holds for the electric field $E_x(z)$ and would also be valid for the field components of a wave traveling parallel to the surface of the superconductor.

where $\boldsymbol{R} = \boldsymbol{r} - \boldsymbol{r}'$, $\boldsymbol{A}$ is the vector potential[5] and ξ is the coherence length for impure superconductors. This coherence length ξ can be calculated from

$$\frac{1}{\xi} = \frac{1}{\xi_0} + \frac{1}{\alpha_{\mathrm{p}} l_{\mathrm{e}}}\,, \tag{4.7}$$

where α_{p} is an empirical constant and ξ_0 is the coherence length of the pure superconductor. It is interesting to note that this treatment and the results of the local and non-local response of a superconductor are very similar to the classical normal and anomalous skin effect [Pöp89].

In 1957 Bardeen, Cooper and Schrieffer [BCS57] published the first microscopic theory of superconductivity and introduced the energy gap $\Delta(T)$. Adding a frequency dependency to the equations of the BCS theory finally led Mattis and Bardeen [MB58] to a non-local relationship reading

$$\boldsymbol{J}_{\mathbf{tot}}(\boldsymbol{r}) = \frac{3}{4\pi^2 v_0 \hbar \lambda_{\mathrm{L}}^0} \int_V \frac{\boldsymbol{R}\,(\boldsymbol{R}\cdot\boldsymbol{A}(\boldsymbol{r}'))\,I(\omega,R,T)\mathrm{e}^{-R/l_{\mathrm{e}}}}{R^4}\,\mathrm{d}V'\,, \tag{4.8}$$

where $I(\omega, R, T)$ is a function decaying on a length scale ξ_0, which in combination with the exponential factor $\mathrm{e}^{-R/l_{\mathrm{e}}}$ gives a total decay dominated by the smaller of ξ_0 and l_{e}. The precise form of $I(\omega, R, T)$ and solutions to Eq. (4.8) in certain limits can be found by Pöpel [Pöp89] or Gao [Gao08].

---

[5] In general the vector potential is defined via the equation $\boldsymbol{B} = \nabla \times \boldsymbol{A}$, but since Mattis and Bardeen [MB58], Pippard [Pip53], Pöpel [Pöp89] and Gao [Gao08] use $\boldsymbol{H} = \nabla \times \boldsymbol{A}$ we will also adopt this convention for this thesis.

4.2. Surface impedance

We will now establish the concept of surface impedance Z_s. Suppose we have a configuration like Fig. 4.1, with an incident electromagnetic wave, then the surface impedance is defined as the ratio of the transverse field components

$$Z_s = \left.\frac{E_x}{H_y}\right|_{z=0} . \tag{4.9}$$

Using the two Maxwell equations $\nabla \times \boldsymbol{E} = -\mathrm{j}\omega\mu_0\boldsymbol{H}$ and $\nabla \times \boldsymbol{H} = \boldsymbol{J} + \partial_t\boldsymbol{D}$, where we ignore the displacement current since its much smaller than $\boldsymbol{J}$ in metals, and $\boldsymbol{H} = \nabla \times \boldsymbol{A}$ we arrive at

$$E_x = -\mathrm{j}\omega\mu_0 A_x\,, \quad H_y = \frac{\mathrm{d}A_x}{\mathrm{d}z}\,, \quad J_x = \frac{\mathrm{d}^2 A_x}{\mathrm{d}z^2}\,, \quad Z_s = -\mathrm{j}\omega\mu_0 \left.\frac{A_x}{\mathrm{d}A_x/\mathrm{d}z}\right|_{z=0} . \tag{4.10}$$

From the third equation we see that the current density J_x can be expressed in terms of the vector potential A_x. Inserting into Eq. (4.8) leads to an integro-differential equation for the vector potential, with which the equation for the surface impedance can be solved under certain assumptions [Gao08].

In general the solution to this equation will be complex which allows us to write the surface impedance as

$$Z_s = R_s + \mathrm{j}\omega L_s = R_s + \mathrm{j}\omega\mu_o\lambda_{\text{eff}}\,, \tag{4.11}$$

with the surface resistance R_s, the surface inductance L_s and the effective penetration depth λ_{eff}. This effective penetration depth λ_{eff} describes the decay of the fields, which can be seen if we assume that all fields (H_y, E_x, A_x and J_x) decay proportional to $\mathrm{e}^{-z/\lambda_{\text{eff}}}$ from the surface toward the inside of the superconductor. After we reinsert the exponential behavior into Eq. (4.10) we get

$$Z_s \approx \mathrm{j}\omega\mu_o\lambda_{\text{eff}}\,, \tag{4.12}$$

which justifies our initial assumption to replace L_s with $\mu_o\lambda_{\text{eff}}$. A simple exponential decay with $\mathrm{e}^{-z/\lambda_{\text{eff}}}$ of all fields is only valid for temperatures $T \ll T_c$ where R_s is usually small enough compared to the imaginary part of the surface impedance so that it can be neglected. But nevertheless it nicely shows the motivation behind the substitution.

4.3. Complex conductivity

Often the surface impedance is evaluated as a function of the complex conductivity $\sigma(\omega) = \sigma_1(\omega) - \mathrm{j}\sigma_2(\omega)$, a concept introduced by Tinkham [Tin56] to describe the transmission through superconducting films.

The derivation of the complex conductivity for the local limit is outlined in Appendix D. For the general case Mattis and Bardeen [MB58] derived

$$\begin{aligned}\frac{\sigma_1}{\sigma_\mathrm{n}} &= \frac{2}{\hbar\omega}\int_\Delta^\infty \frac{[f(E)-f(E+\hbar\omega)](E^2+\Delta^2+\hbar\omega E)}{\sqrt{E^2-\Delta^2}\sqrt{(E+\hbar\omega)^2-\Delta^2}}\,\mathrm{d}E \\ &\quad+\frac{1}{\hbar\omega}\int_{\Delta-\hbar\omega}^{-\Delta} \frac{[1-2f(E+\hbar\omega)](E^2+\Delta^2+\hbar\omega E)}{\sqrt{E^2-\Delta^2}\sqrt{(E+\hbar\omega)^2-\Delta^2}}\,\mathrm{d}E\,, \end{aligned} \tag{4.13}$$

$$\frac{\sigma_2}{\sigma_\mathrm{n}} = \frac{1}{\hbar\omega}\int_{\max\{\Delta-\hbar\omega,-\Delta\}}^{\Delta} \frac{[1-2f(E+\hbar\omega)](E^2+\Delta^2+\hbar\omega E)}{\sqrt{\Delta^2-E^2}\sqrt{(E+\hbar\omega)^2-\Delta^2}}\,\mathrm{d}E\,, \tag{4.14}$$

where σ_n is the conductivity from normal conducting electrons, E is the particle energy, $\Delta(T)$ is the temperature dependent gap parameter and $f(E)$ is the Fermi-Dirac distribution given by

$$f(E) = \frac{1}{1+\mathrm{e}^{E/k_\mathrm{B}T}}\,, \tag{4.15}$$

where k_B is Boltzmann's constant. Furthermore the second integral of Eq. (4.13) is equal to zero if $\hbar\omega < 2\Delta$. An analytical solution of Eq. (4.13) and (4.14) is only possible for $T = 0$, as soon as $T > 0$ the integral has to be solved numerically. But under the conditions[6] that $\hbar\omega$, $k_\mathrm{B}T \ll 2\Delta$ the Fermi-Dirac distribution can be approximated by a Maxwell-Boltzmann distribution $f(E) \approx \mathrm{e}^{-E/k_\mathrm{B}T}$ and the expressions for the complex conductivity simplify to [Bar09]

$$\frac{\sigma_1}{\sigma_\mathrm{n}} \approx \frac{4\Delta}{\hbar\omega}\mathrm{e}^{-\Delta/k_\mathrm{B}T}\sinh\left(\frac{\hbar\omega}{2k_\mathrm{B}T}\right)K_0\left(\frac{\hbar\omega}{2k_\mathrm{B}T}\right)\,, \tag{4.16}$$

$$\frac{\sigma_2}{\sigma_\mathrm{n}} \approx \frac{\pi\Delta}{\hbar\omega}\left[1-2\mathrm{e}^{-\Delta/k_\mathrm{B}T}\mathrm{e}^{-\hbar\omega/2k_\mathrm{B}T}I_0\left(\frac{\hbar\omega}{2k_\mathrm{B}T}\right)\right]\,, \tag{4.17}$$

where I_0 and K_0 are the modified Bessel functions of the first and second kind, respectively [AS64].

4.4. Local response

Approximating Eq. (4.8) in the local limit, where $\xi_0 \ll \lambda_\mathrm{L}^0$ or $l_\mathrm{e} \ll \lambda_\mathrm{L}^0$ and expressing the surface impedance Z_s in terms of complex conductivity leads to [Gao08]

$$Z_s = \mathrm{j}\mu_0\omega\left(\frac{\omega l_\mathrm{e}}{v_\mathrm{F}\left(\lambda_\mathrm{L}^0\right)^2}\frac{\sigma_2+\mathrm{j}\sigma_1}{\sigma_\mathrm{n}}\right)^{-\frac{1}{2}}\,, \tag{4.18}$$

with the Fermi velocity v_F, the electron mean free path l_e and the London penetration depth λ_L^0 at absolute zero.

---

[6] In our system we use microwave frequencies in the GHz range ($\hbar\omega = hf \approx 2\cdot 10^{-24}$ J, for $f = 3$ GHz) and we measure at temperatures of about 30 mK ($k_\mathrm{B}T \approx 4\cdot 10^{-25}$ J) so the conditions are easily fulfilled for niobium, where $T_\mathrm{c} = 9.2$ K and the energy gap from BCS-theory [BCS57] $2\Delta(T) \approx 2\Delta(0) \approx 3.5k_\mathrm{B}T_\mathrm{c} \approx 2.5\cdot 10^{-22}$ J.

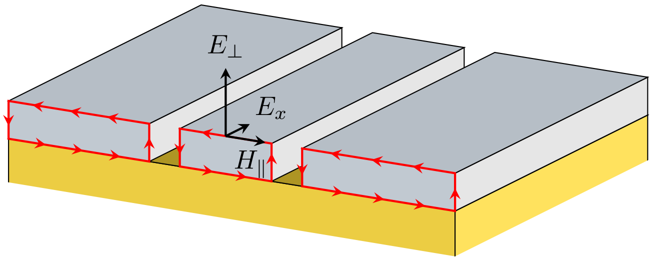

Figure 4.2.: Due to the relative permittivity of the substrate the phase velocities of an electromagnetic wave traveling in x-direction are different above and below the superconducting film of a coplanar waveguide (CPW). The result is a small component E_x on the surface layer of the superconductor causing a flow of power into the superconductor which can be calculated with the help of Poynting's theorem. The necessary integration is carried out along the red paths and will also yield the connection between surface and kinetic inductance $L_l^{\mathrm{ki}} = gL_s$.

The response of the surface impedance to a small change in complex conductivity can be calculated with

$$\delta \ln Z_s = -\frac{1}{2}\delta \ln \sigma\,, \tag{4.19}$$

$$\frac{\delta Z_s}{Z_s} = -\frac{1}{2}\frac{\delta\sigma}{\sigma}\,. \tag{4.20}$$

4.5. Non-local response, the extreme anomalous limit

In the extreme anomalous limit, characterized via $\xi_0 \gg \lambda_{\mathrm{L}}^0$ and $l_{\mathrm{e}} \gg \lambda_{\mathrm{L}}^0$, we get [Gao08]

$$Z_s = \frac{\mathrm{j}\sqrt{3}\mu_0\omega}{2}\left(\frac{3\pi\omega}{4v_{\mathrm{F}}\left(\lambda_{\mathrm{L}}^0\right)^2}\frac{\sigma_2+\mathrm{j}\sigma_1}{\sigma_{\mathrm{n}}}\right)^{-\frac{1}{3}}\,. \tag{4.21}$$

Using the same little trick with the logarithm as in Eq. (4.19) we derive

$$\frac{\delta Z_s}{Z_s} = -\frac{1}{3}\frac{\delta\sigma}{\sigma}\,. \tag{4.22}$$

4.6. From surface inductance to kinetic inductance

The surface impedance derived in the previous sections describes the electromagnetic response of a superconducting sheet of some thickness t. But we want to ascertain the response of a coplanar waveguide geometry. So how do we get from the surface impedance Z_s with the surface inductance L_s to the kinetic inductance L_{ki} for a coplanar waveguide (CPW) geometry?

The answer is Poynting's theorem, a statement of energy conservation and power balance. We have pointed out before that electromagnetic fields will penetrate a superconductor on a characteristic length scale λ_{eff}. This penetration of the magnetic field and the affected Cooper pairs in this region will contribute to the total inductance. Furthermore, due to the asymmetry of the CPW structure (see Fig. 4.2) the waveguide will not support true TEM waves. There will be a small contribution E_x to the electric field in the direction of propagation which leads to a component of the Poynting vector $\boldsymbol{S} = \boldsymbol{E} \times \boldsymbol{H}$ normal to the surface. Integrating it along the red path of Fig. 4.2 then yields according to Poynting's theorem[7] the complex power delivered into the system

$$\frac{1}{2} \int_{\mathcal{C}} \boldsymbol{E} \times \boldsymbol{H}^* \, \mathrm{d}\boldsymbol{l} = \frac{1}{2} \int_{\mathcal{C}} E_x \cdot H_{\|}^* \, \mathrm{d}l = \frac{I^2}{2} \left(R_l + \mathrm{j}\omega L_l^{\mathrm{ki}} \right) , \tag{4.23}$$

and if we insert the definition of the surface impedance $Z_s = E_x / H_{\|}$ the relation with the surface impedance reads

$$R_l = g R_s \, , \quad L_l^{\mathrm{ki}} = g L_s \quad \text{with} \quad g = \frac{\int_{\mathcal{C}} H_{\|}^2 \, \mathrm{d}l}{I^2} \, . \tag{4.24}$$

The calculation of the geometric factor g (it has the unit of an inverse length) is not straight forward, but in principle it is just a geometry factor only depending on the film thickness t, the central conductor width w and the gap to the ground planes s.[8] For thick films conformal mapping techniques can be applied once again but for films where $t < \lambda_{\mathrm{eff}}$ other ways have to be found. The reason why $H_{\|}$ can no longer be derived from conformal mapping lies in the fact that the assumption that the field outside of a superconductor is very well approximated by the field of a perfect conductor breaks down when the magnetic field penetrates the whole film.

---

[7] We use the convention where the surface normal points into the superconductor.

[8] Approximate formulas for the calculation of g can be found in the works of Collin [Col92] or Yoshida [Yos+95]. Caution has to be taken with the formula of Yoshida, because g is defined differently there. It has to be divided by the central conductor width w to convert to the g values of Collin. For our configuration the values calculated using Collin's formula ($g \approx 0.13\,\mathrm{\mu m}^{-1}$) differ by a factor of 2.4 from Yoshida's ($g \approx 0.31\,\mathrm{\mu m}^{-1}$).

5. Cooper pair break-up and quasiparticle recombination

The previous chapter indicated the dependency of the surface impedance on the effective penetration depth and the complex conductivity. Now those results will be linked to the characteristics of the charge carriers and thereby to the microscopic picture of a superconductor.

A simple description of metals is given by Sommerfeld's theory [AM76] which describes the conduction electrons as a free gas. This is quite remarkable since the Coulomb interaction of the negatively charged electrons usually can't be neglected. There is the repulsion between the electrons, which is screened to some extent by the many surrounding electrons and there is also the attraction of the positively charged atomic cores.

The reason why some metals can be treated with the free electron model, is that actually it doesn't describe electrons but quasiparticles. Those quasiparticles are a many-body system more or less consisting of an electron and its screening cloud. But despite the complicated nature of the quasiparticles, the Sommerfeld theory can be adapted simply by substituting the electron mass with a new effective mass m_{eff}. The powerful concept of quasiparticles can be applied in many cases (e. g. phonons) and dates back to Landau, who introduced it in his theory of Fermi liquids [AM76].

A similar kind of quasiparticles also exist in superconductors, the so-called Bogoliubov quasiparticles [Tin56]. When a Cooper pair is broken up due to the absorption of a phonon, photon or any other kind of excitation two quasiparticles are formed. After a characteristic time τ_{qp} the excited system will relax back into the equilibrium state by recombination of two quasiparticles to a Cooper pair.

The dominant mechanism just below the critical temperature seems to be electron-phonon relaxation [Bar+08], where two electrons recombine to a Cooper pair and a phonon is emitted. For even smaller temperatures a saturation of the relaxation time has been observed that can't be explained in this picture. As of yet the responsible processes are still unknown, although some attempts at explaining the data have been made [Rei00].

As we will see the break-up of Cooper pairs and the resulting creation of quasiparticles has a significant effect on the complex conductivity and therefore also on resonator properties like the resonance frequency or the quality factor. In our experiment this dependency is utilized to measure the impact of laser irradiation on microwave resonators in order to investigate and understand quasiparticle creation and recombination processes. In current experiments we have also started using the laser to polarize NV^{-} centers in a diamond which is placed directly on top of the resonator. For this kind of experiments it is obviously crucial to know and consider the effects of the laser light not only on the diamond but also on the resonator. Another possible application of this effect, that we have already mentioned, is the usage as microwave kinetic inductance detectors (MKIDs) for astronomy. The primary advantage is the relatively easy fabrication of large arrays of MKIDs [Day+03]. Because of this interesting prospect many people are actively working on this field and to get a more in-depth analysis of quasiparticle effects it is worth looking into the theses of Mazin [Maz04], Gao [Gao08], Barends [Bar09], Noroozian [Nor12] and the review of Zmuidzinas [Zmu12].

5.1. The influence of quasiparticle density on the complex conductivity

At finite temperatures every superconductor will contain thermally excited quasiparticles and for $\hbar\omega$, $k_\mathrm{B}T \ll 2\Delta$ their density can be approximated by [Bar09]

$$n_\mathrm{qp} \approx 2N_0\sqrt{2k_\mathrm{B}T\Delta_0}\,\mathrm{e}^{-\Delta_0/k_\mathrm{B}T}\,, \tag{5.1}$$

where N_0 is the single spin density, k_B is Boltzmann's constant and $\Delta_0 = \Delta(T=0)$ is once again the energy gap of superconductors at absolute zero.

Looking back at the equations for the complex conductivity, Eq. (4.16) and (4.17), we see that the exponential terms $\mathrm{e}^{-\Delta/k_\mathrm{B}T}$ look very similar to the quasiparticle density. The only difference is that the former still feature the temperature dependent gap parameter Δ. In the lowest order the gap parameter can be written as [Gao+08a]

$$\frac{\Delta}{\Delta_0} = 1 - \sqrt{\frac{2k_\mathrm{B}T}{\Delta_0}}\,\mathrm{e}^{-\Delta_0/k_\mathrm{B}T}\,. \tag{5.2}$$

Now that we have an expression for the gap parameter we can insert it into Eq. (4.16) and (4.17). Replacing the according exponentials with the quasiparticle density from Eq. (5.1) and only keeping the lowest order terms yields

$$\frac{\sigma_1(n_\mathrm{qp},T)}{\sigma_\mathrm{n}} = \frac{2\Delta_0}{\hbar\omega}\frac{n_\mathrm{qp}}{N_0\sqrt{2\pi k_\mathrm{B}T\Delta_0}}\sinh\left(\frac{\hbar\omega}{2k_\mathrm{B}T}\right)K_0\left(\frac{\hbar\omega}{2k_\mathrm{B}T}\right)\,, \tag{5.3}$$

$$\frac{\sigma_2(n_\mathrm{qp},T)}{\sigma_\mathrm{n}} = \frac{\pi\Delta_0}{\hbar\omega}\left[1 - \frac{n_\mathrm{qp}}{2N_0\Delta_0}\left(1+\sqrt{\frac{2\Delta_0}{\pi k_\mathrm{B}T}}\,\mathrm{e}^{-\hbar\omega/2k_\mathrm{B}T}I_0\left(\frac{\hbar\omega}{2k_\mathrm{B}T}\right)\right)\right]\,, \tag{5.4}$$

The important message of these equations is that both σ_1 and σ_2 depend linearly on the quasiparticle density, which allows us to rewrite Eq. (4.20) and (4.22)

$$\frac{\delta Z_s}{Z_s} = \gamma\frac{\delta\sigma}{\sigma} = \gamma\kappa\,\delta n_\mathrm{qp}\,, \tag{5.5}$$

where we have introduced

$$\kappa = \frac{\sigma_1+\sigma_2}{\sigma}\,, \tag{5.6}$$

and

$$\gamma = \begin{cases} -\frac{1}{2} & \text{thick superconductor, local limit} \\ -\frac{1}{3} & \text{thick superconductor, non-local limit} \end{cases} \tag{5.7}$$

5.2. Resonator response to quasiparticle fluctuations

In this section we will collect the results from the previous sections to derive the response of the CPW resonator to quasiparticle density fluctuations and perturbations in general.

First let us consider Eq. (5.5) again. In case of low temperatures and for good conductors[1] we can usually write $R_s \ll \omega L_s$ as well as $\sigma_1 \ll \sigma_2$, which leads to

$$\frac{\delta Z_s}{Z_s} \approx \frac{\delta R_s + \mathrm{j}\omega \delta L_s}{\mathrm{j}\omega L_s} \approx \gamma \frac{\delta\sigma_1 - \mathrm{j}\delta\sigma_2}{-\mathrm{j}\sigma_2}\,, \tag{5.8}$$

or

$$\frac{\delta R_s}{\omega L_s} = -\gamma \frac{\delta\sigma_1}{\sigma_2}\,, \tag{5.9}$$

$$\frac{\delta L_s}{L_s} = \gamma \frac{\delta\sigma_2}{\sigma_2}\,. \tag{5.10}$$

For a half-wave transmission line resonator the resonance frequency is given by (see Appendix C).

$$\omega_0 = \frac{2\pi}{2l\sqrt{L_l^{\mathrm{tot}} C_l}} = \frac{\pi}{l\sqrt{(L_l^{\mathrm{m}} + L_l^{\mathrm{ki}})C_l}} \tag{5.11}$$

A perturbation of the quasiparticle density changes the surface impedance and thereby also the kinetic inductance. From Eq. (5.11) we calculate

$$\delta \ln \omega_0 = -\frac{1}{2}\delta \ln L_l^{\mathrm{tot}} \tag{5.12}$$

$$\frac{\delta\omega_0}{\omega_0} = -\frac{\alpha}{2}\frac{\delta L_l^{\mathrm{ki}}}{L_l^{\mathrm{ki}}} \tag{5.13}$$

$$= -\frac{\alpha}{2}\frac{\delta L_s}{L_s}\,, \tag{5.14}$$

where α is the kinetic inductance fraction from Eq. 4.2. The internal quality factor, defined by $Q_{\mathrm{int}} = \omega_0 RC$, can be written in terms of transmission line parameters as

$$Q_{\mathrm{int}} = \omega_0 \frac{L_l^{\mathrm{tot}}}{R_l}\,. \tag{5.15}$$

This result can easily be obtained by using Eq. (C.3) and (C.4) of Appendix C and putting all the losses into R_l, which allows us to discard G_l. Perturbations of the

---

[1] Both conditions are fulfilled for our system, since we operate at 30 mK and use niobium in the superconducting state.

inverse quality factor can then be expressed as

$$\delta Q_{\mathrm{int}}^{-1} = \delta \frac{R_l}{\omega_0 L_l^{\mathrm{tot}}} \tag{5.16}$$

$$\approx \frac{\delta R_l}{\omega_0 L_l^{\mathrm{tot}}} \tag{5.17}$$

$$= \alpha \frac{\delta R_s}{\omega_0 L_s}\,, \tag{5.18}$$

for $R_s \ll \omega_0 L_l^{\mathrm{tot}}$. So far we have connected the frequency shift and the quality factor perturbation to the complex conductivity σ. Furthermore Eq. (5.5) tells us that both the frequency as well as the inverse quality factor shift depend linearly on the quasiparticle density.

Equations (5.14) and (5.18) are fine for analyzing data from continuous perturbations like a constant light flux, where we have time to sweep a whole frequency range and record a spectrum. If we want to measure time dependent effects which are shorter than the sweep time a different approach has to be taken. Instead of sweeping the frequency, we keep the frequency fixed at the undisturbed resonance frequency and measure the phase

$$\tan\phi = \frac{\operatorname{Im} S_{21}}{\operatorname{Re} S_{21}}\,, \tag{5.19}$$

and the amplitude

$$A = |S_{21}| = \sqrt{\operatorname{Re}(S_{21})^2 + \operatorname{Im}(S_{21})^2}\,. \tag{5.20}$$

Substituting S_{21} by Eq. (3.25) together with the assumption of only small phase changes $\tan\phi \approx \phi$ yields[2]

$$\phi \approx (1 - S_{21}^{\mathrm{max}}) 2 Q_{\mathrm{tot}} \frac{\delta\omega_0}{\omega_0}\,. \tag{5.21}$$

The calculation for the amplitude at the resonance frequency, where we use Eq. (3.24), results in

$$\delta A \approx -\frac{Q_{\mathrm{ext}}}{(1 + Q_{\mathrm{ext}}/Q_{\mathrm{int}})^2} \delta Q_{\mathrm{int}}^{-1}\,. \tag{5.22}$$

We see that the phase and the amplitude should also be linearly proportional to fluctuations of the quasiparticle density.[3] Since we want to investigate the effects of photon irradiation on microwave resonators the last missing piece is now the dependence of the quasiparticle density n_{qp} on the laser power P_{lp}, which is given by [Maz04]

$$\delta n_{\mathrm{qp}} = \frac{\tau_{\mathrm{qp}} \eta}{V \Delta} \delta P_{\mathrm{lp}}\,, \tag{5.23}$$

where τ_{qp} is the quasiparticle lifetime, V the resonator volume, η is the photon to quasiparticle conversion efficiency and Δ is the energy gap. The conversion efficiency is usually about $\eta \approx 0.6$ [Gao08; Maz04].

---

[2] This approximation for the phase ϕ and amplitude A is derived in Appendix G.

[3] Combining Eq. (5.5), (5.23), (5.14), (5.10), (5.18) and (5.9) leads to $\phi \propto \frac{\delta\omega_0}{\omega_0} \propto \delta n_{\mathrm{qp}} \propto \delta P_{\mathrm{lp}}$ and $A \propto \delta Q_{\mathrm{int}}^{-1} \propto \delta n_{\mathrm{qp}} \propto \delta P_{\mathrm{lp}}$.

6. Two level fluctuators

In order to perform measurements on our resonator we have to probe the microwave system with a measurement power P_{mw}. We have argued before that additional energy introduced into the system can break up Cooper pairs thus reducing the total conductivity which then should reduce the quality factor of the resonator.

But up to a certain power something curious happens. The quality factor increases simultaneously with the microwave measurement power. This shouldn't happen for a superconducting niobium resonator but it is a well-known phenomenon in glasses and amorphous materials in general. In those materials a similar unexpected behavior has been measured for the low-temperature dependence of the heat capacity, the sound velocity and other parameters [Esq98].

Unlike crystalline solids, amorphous materials don't have any kind of long-range order. A result of the disordered structure is that there exist metastable atomic states and atoms can tunnel in between different positions (see Fig. 6.1). At low temperatures these two-level fluctuators[1] constitute the main loss mechanism.

To explain the measurement data a phenomenological two-level system model, as can be seen in Fig. 6.2, was proposed by both Anderson [AHV72] and Phillips [Phi72] at a similar time.

As for the question of where those two-level fluctuators (TLFs) are located in CPW resonators, until now there is no definitive answer. For our resonators there exist various possibilities. The TLFs could be located in the bulk volume of the dielectric substrate or inside the niobium film. Aside from that it is known that amorphous layers can be formed by niobium oxides $\mathrm{Nb}_x\mathrm{O}_y$ on the metal surface or some other oxides at the substrate–air interfaces [Gra75; LS74; Sag+11]. Additionally amorphous layers are also formed at the metal–substrate interfaces due to oxides and a mismatch of the substrate and metal lattice. It seems fairly certain that the bulk volume can be eliminated as TLF source, because Gao et al. [Gao+08b] as well as Wenner et al. [Wen+11] found evidence for a surface effect. But it is not yet clear whether the main source for two-level fluctuators are the metal–substrate, metal–air or substrate–air interfaces.

The following short review of the main results for two-level systems (TLSs) will mostly follow the treatment of the subject in Gao's thesis [Gao08].

---

[1] In recent literature the term two-level system (TLS) has been used to describe coherent systems, whereas two-level fluctuator (TLF) has been coined to describe incoherent systems. In this thesis TLS and TLF are used rather synonymously, but we always mean TLFs. Interestingly just a few years ago (2010), Lisenfeld et al. [Lis+10] have shown that it is possible to couple a superconducting qubit coherently to a single TLS.

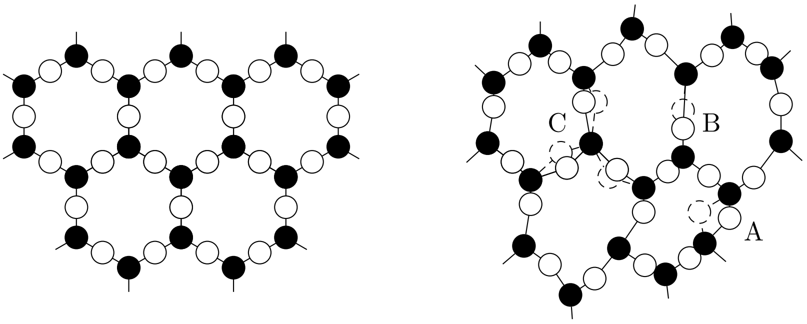

(a) (b)

Figure 6.1.: Reproduction of a figure by Hunklinger and Arnold [HA76] to visualize the concept of two level fluctuators. (a) Shows the crystalline state of SiO_2 while (b) depicts the amorphous state of SiO_2. The characters A, B and C point out possible metastable states, which could be modeled with a two level system (TLS). In case of superconducting coplanar waveguide resonators the idea is that there may be an amorphous surface layer due to oxidation which is responsible for TLS effects [Gao+08b].

6.1. Two-level system model

Figure 6.1 shows the double-well potential to model a TLS, which consists of two superimposed harmonic-shaped potentials. The basis states of the two individual parabolic-shaped potentials are denoted ϕ_1 and ϕ_2, respectively. The Hamiltonian of the combined system can be written in terms of those basis states and reads

$$H_0 = \frac{1}{2}\begin{pmatrix} -\Delta & \Delta_0 \\ \Delta_0 & \Delta \end{pmatrix}, \tag{6.1}$$

where Δ is the asymmetry energy and Δ_0 is the so-called tunnel splitting, describing the coupling of the states. Although Δ_0 depends on the precise shape of the potential, and therefore on the material, often it can be approximated with [Phi87]

$$\Delta_0 = \hbar\omega_0 \mathrm{e}^{-\lambda}, \quad \text{with} \quad \lambda = \sqrt{\frac{2mV}{\hbar^2}}\, d, \tag{6.2}$$

where V is the tunnel barrier height, d the separation of the potential minima and $\hbar\omega_0$ is approximately the mean value of the two ground state energies. Since we are dealing with an amorphous solid there will be a certain distribution of values for Δ and Δ_0. Anderson [AHV72] and Phillips [Phi72] suggested

$$P(\Delta, \Delta_0)\, \mathrm{d}\Delta \mathrm{d}\Delta_0 = \frac{P_0}{\Delta_0}\, \mathrm{d}\Delta \mathrm{d}\Delta_0\,. \tag{6.3}$$

A short summary of the reasoning behind this choice can be found here [Phi87].

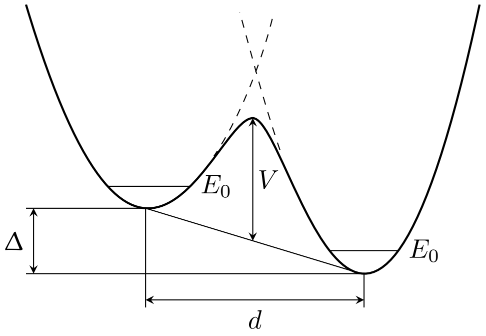

Figure 6.2.: The double-well potential of a two level system (TLS), where Δ is the asymmetry energy, E_0 the respective ground state energy, d the well separation and V is the barrier height.

Diagonalizing the Hamiltonian of Eq. (6.1), hence transforming to the energy eigenstates, gives

$$H_0 = \frac{1}{2}\varepsilon\sigma_z \tag{6.4}$$

with the energy splitting of the states ε and the Pauli matrix σ_z (see Appendix F).

To describe excitation and relaxation processes we need to couple the TLS system to some external field or phonons. Mathematically this means adding an interaction Hamiltonian to the Hamiltonian from Eq. (6.4). According to Phillips [Phi87] perturbations by electromagnetic or strain fields mainly change the asymmetry energy Δ while leaving the tunnel splitting Δ_0 more or less unaffected. So in the local basis (ϕ_1, ϕ_2) the perturbation will be diagonal, but after transformation to the energy basis states the interaction hamiltonian for electric excitations is

$$H^{\mathrm{e}}_{\mathrm{int}} = \left[\frac{\Delta}{\varepsilon}\sigma_z + \frac{\Delta_0}{\varepsilon}\sigma_x\right] \boldsymbol{d_0} \cdot \boldsymbol{E}\,, \tag{6.5}$$

with the Pauli matrices σ_i, the electric dipole moment $\boldsymbol{d_0}$ and the electric field $\boldsymbol{E}$. For interactions with phonons the Hamiltonian reads

$$H^{\mathrm{a}}_{\mathrm{int}} = \left[\frac{\Delta}{\varepsilon}\sigma_z + \frac{\Delta_0}{\varepsilon}\sigma_x\right] \gamma_{\mathrm{e}} e_{\mathrm{s}}\,, \tag{6.6}$$

where γ_{e} is the elastic dipole moment and e_{s} is the strain field. A similar expression can be found for the magnetic problem with the magnetic dipole moment $\boldsymbol{\mu}$ and the magnetic field $\boldsymbol{B}$. In our experiments the two-level systems will couple to the microwave field as well as to phonons that get excited by the heat, which is deposited by the laser.

As the usage of Pauli matrices maybe already indicated, the Hamiltonian of the complete system $H = H_0 + H_{\mathrm{int}}$ bears a great resemblance to the Hamiltonian for the dynamics of a spin 1/2 system in a magnetic field. A problem which has been considered for a long time in the understanding of nuclear magnetic resonances (NMRs) and whose answer can be found by solving the Bloch equations [Blo46]. This analogy between the two systems allows us to translate the TLS system into a spin 1/2 system, get the solution via the Bloch equations and then transforming it back.

After a lengthy derivation eventually the TLS contribution to the dielectric constant due to electric perturbations is obtained as [Gao08]

$$\epsilon_{\mathrm{TLS}} = -\frac{2P_0 d_0^2}{3}\left[\Psi\left(\frac{1}{2} - \frac{\hbar\omega - \mathrm{j}\Gamma}{2\mathrm{j}\pi k_{\mathrm{B}}T}\right) - \ln\frac{\varepsilon_{\mathrm{max}}}{2\pi k_{\mathrm{B}}T}\right], \tag{6.7}$$

where P_0 is from the density of states in Eq. (6.3), d_0 the electric dipole moment, Ψ the complex digamma function [AS64], Γ an average dephasing linewidth for the TLS distribution and $\varepsilon_{\mathrm{max}}$ is the maximum energy splitting of the TLSs.

6.2. Resonator response for two-level systems

The change of the dielectric constant described by Eq. (6.7) will influence the resonator properties like the resonance frequency and the quality factor, since both the phase velocity and the loss in the system depend on the dielectric constant. For small perturbations the according frequency shift of a resonator can be derived as [Poz11]

$$\frac{\delta\omega_0}{\omega_0} \simeq -\frac{\int_V \left(\Delta\epsilon'|\boldsymbol{E}|^2 + \Delta\mu'|\boldsymbol{H}|^2\right)\,\mathrm{d}V}{\int_V \left(\epsilon'|\boldsymbol{E}|^2 + \mu'|\boldsymbol{H}|^2\right)\,\mathrm{d}V}, \tag{6.8}$$

where prime denotes the real part of $\epsilon = \epsilon' - \mathrm{j}\epsilon''$ and $\mu = \mu' - \mathrm{j}\mu''$. As we will see below the imaginary parts of the permittivity ϵ and the permeability μ describe the losses and are therefore important for the quality factor shift. Due to the assumed small perturbations the frequency will stay close to resonance and so $W_{\mathrm{e}} = W_{\mathrm{m}}$ follows. With this, $\Delta\mu' = 0$ and $\Delta\epsilon' = \epsilon'_{\mathrm{TLS}}$ we can rewrite Eq. (6.8) and get

$$\frac{\delta\omega_0}{\omega_0} = -\frac{\int_{V_{\mathrm{h}}} \epsilon'_{\mathrm{TLS}}|\boldsymbol{E}|^2\,\mathrm{d}V}{2\int_V \epsilon'|\boldsymbol{E}|^2\,\mathrm{d}V}, \tag{6.9}$$

where V_{h} is the host volume of the two-level fluctuators, which considers the fact that TLFs may not be distributed over the whole resonator volume V. The corresponding shift of the quality factor Q_{tot} can be calculated from Eq. (3.6) and with [Poz11]

$$P_{\mathrm{loss}} = \frac{\omega}{2}\int_V \left(\epsilon''|\boldsymbol{E}|^2 + \mu''|\boldsymbol{H}|^2\right)\,\mathrm{d}V, \tag{6.10}$$

which, for $\Delta\mu'' = 0$ and $\Delta\epsilon'' = \epsilon''_{\mathrm{TLS}}$, yields

$$\delta Q_{\mathrm{tot}}^{-1} = -\frac{\int_{V_{\mathrm{h}}} \epsilon''_{\mathrm{TLS}}|\boldsymbol{E}|^2\,\mathrm{d}V}{\int_V \epsilon'|\boldsymbol{E}|^2\,\mathrm{d}V}. \tag{6.11}$$

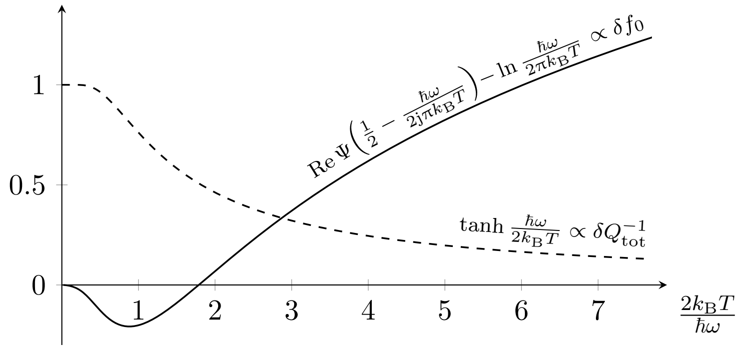

Figure 6.3.: Temperature dependence of the frequency shift δf_0 and the change of the inverse quality factor $\delta Q_\mathrm{tot}^{-1}$ predicted by the two-level system model.

Putting everything together finally results in [Gao08]

$$\frac{\delta\omega_0}{\omega_0}=\frac{F\delta_\mathrm{TLS}^0}{\pi}\left[\mathrm{Re}\,\Psi\left(\frac{1}{2}-\frac{\hbar\omega}{2\mathrm{j}\pi k_\mathrm{B}T}\right)-\ln\frac{\hbar\omega}{2\pi k_\mathrm{B}T}\right], \tag{6.12}$$

$$\delta Q_\mathrm{tot}^{-1}=F\delta_\mathrm{TLS}^0\tanh\left(\frac{\hbar\omega}{2k_\mathrm{B}T}\right), \tag{6.13}$$

with $\delta_\mathrm{TLS}^0=3P_0d_0^2/2\epsilon_\mathrm{h}$ and a filling factor

$$F=-\frac{\int_{V_\mathrm{h}}\epsilon_\mathrm{h}|\boldsymbol{E}|^2\,\mathrm{d}V}{\int_V\epsilon'|\boldsymbol{E}|^2\,\mathrm{d}V}\,. \tag{6.14}$$

7. Experimental setup

This chapter will give a description of the setup and measurement techniques used in our experiments. Since we wanted to study the effects of quasiparticles and two level fluctuators (TLFs) in superconducting microwave resonators there are a few requirements we need to meet.

First of all our measurements need a cryogenic environment. This is provided by a dilution refrigerator whose basic principle of operation will be explained in the first section.

Then there has to be some way to excite the quasiparticles and the TLFs. This can happen for instance with phonons through an increase of temperature or with photons from a light source. In most of the discussed experiments photons from a green laser will be the source of excitations. Therefore, we also need an optical setup which will be the topic of the next section.

Finally we need to be able to measure these effects via probing the resonators in the microwave domain which is done with a vector network analyzer (VNA) for constant light flux and with a fast digitizer card for experiments with pulsed light. The microwave setup will be treated in the last section.

7.1. Dilution refrigerator

The requirement of a cryogenic environment stems from the fact that we don't want any thermal photons in the resonator, because they would distort the measurement results and excite the TLFs and quasiparticles we want to investigate. The thermal photon occupation is given by the Bose-Einstein distribution

$$\bar{n}(\omega, T) = \frac{1}{\mathrm{e}^{\frac{\hbar\omega}{k_\mathrm{B}T}} - 1}\,, \tag{7.1}$$

which should fulfill $\bar{n} < 1$ so that the resonator is in the ground state. To give an example, for our microwave resonators with a resonance frequency of approximately 3 GHz and a temperature of 50 mK a thermal occupation of $\bar{n} \approx 0.06$ would be obtained.

To reach the necessary low temperatures we use a Triton dilution refrigerator from Oxford Instruments. It is a cryogen-free system due to the usage of a pulse tube refrigerator for precooling instead of liquid Helium. This precooling unit allows achieving temperatures of about 4 K, further cooling is done by exploiting the special properties of ^{3}He/^{4}He mixtures.

Below a critical temperature the ^{3}He/^{4}He mixture separates into two distinct phases. One with an abundance of ^{3}He, the concentrated phase, and another one with an

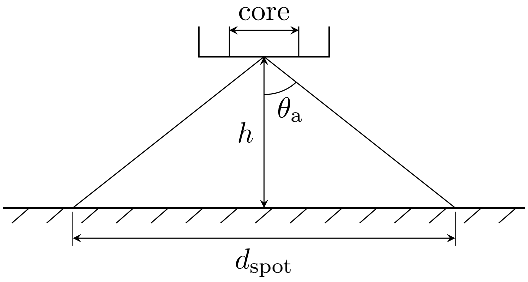

Figure 7.1.: The size of the light spot on the resonator is determined by the numerical aperture (NA) of the fiber and the distance h from the fiber end to the resonator. For our configuration, NA $= 0.48$ and $h \approx 3.3\,\mathrm{mm}$, we get $d_{\mathrm{spot}} \approx 3.6\,\mathrm{mm}$.

abundance of ^{4}He, the dilute phase. In a somewhat simplified view the concentrated phase can be considered as liquid ^{3}He while the ^{3}He gas moving through the inert ^{4}He behaving similar to a gas. At the phase boundary the liquid ^{3}He can absorb thermal energy from the surroundings and evaporate from the concentrated into the dilute phase, increasing its entropy and thereby lowering the temperature of the surrounding environment. Since there is always a finite amount of ^{3}He in the dilute phase – even if the temperature decreased to absolute zero – cooling works for arbitrarily low temperatures and is only limited by heat leaking into the system and heat exchanger performance [Bal07].

With our dilution refrigerator (see Fig. 7.9) we are able to reach temperatures in the range of 20 mK to 30 mK at the lowest temperature stage, while having a cooling power of 400 µW at 110 mK. At the moment a fully automatic cool-down takes approximately 50 h, but this value strongly depends on the extent of additionally built-in microwave wiring for the experiments.

The big advantage of dilution refrigerators is the possibility to construct the ^{3}He/^{4}He dilution unit as a closed-loop system which easily allows a few weeks of continuous operation without intervention and warm-up.

More information on the characteristics of our dilution refrigerator can be found in the theses of Amsüss [Ams12] and Koller [Kol12].

7.2. Optical setup

As mentioned before we want to use light to study quasiparticle and two level fluctuator phenomena of our resonator. Therefore, we have to find a way to get the light from a laser into the cryogenic environment of the dilution refrigerator. Our setup consists mainly of two parts, on the one hand there is the optics outside of the dilution refrigerator which is located on an optical table and on the other hand there are the fibers which guide the light to the 20 mK stage of the dilution refrigerator.

A sketch of the complete experimental setup including the optical setup can be seen

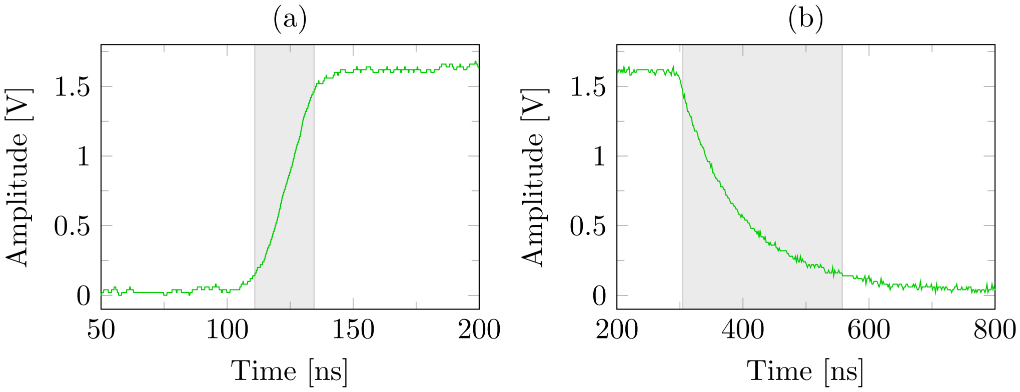

Figure 7.2.: Laser pulses are created by applying a TTL pulse to the AOM. In the "off"-state all laser light is in the zeroth mode, which is blocked by a aperture, but in the "on"-state some light is scattered into the first mode, which can pass the aperture (see Fig. 7.9). This plot shows the rise and fall time (width of the gray area) of such a laser pulse measured with a photodiode. The times are determined by the 10 and 90 percent mark of the step height. (a) The rise time is 23.5 ns and (b) the fall time is 250 ns.

in Fig. 7.9. The laser light is created with a green laser (532 nm) and is then guided through a shutter to a lens in order to focus the light at the subsequent acousto-optic modulator (AOM). In the AOM a piezo element creates a standing wave within a crystal so that an incident electromagnetic wave is Bragg reflected into different orders. The ratio that is reflected into higher orders is determined by the amplitude of the standing wave. By positioning an aperture after the AOM, where only the first order of reflection can pass, we can therefore adjust the transmitted power by varying the standing wave amplitude. The great advantage of controlling the transmitted laser power with an AOM and not with the laser source itself is the very fast time response of the AOM (see Fig. 7.2), that we need for creating short laser pulses. After the AOM and aperture follows another lens collimating the laser beam again. Right before coupling into the multimode fiber (200 µm core diameter) with a fiber collimator there is an optical attenuator, which is necessary for very small laser powers[1]. The fiber then guides the light to the top of the dilution refrigerator where we couple via commercially bought SMA couplers to the fiber on the inside of the cryostat. On the other end of this fiber is a simple SMA connector that can be screwed on the lid of our resonator sample box (see Fig. 7.6). The end of the SMA connector terminates in the plane of the lid bottom. The spot size on the resonator can be calculated from the fibers numerical aperture (NA)

$$\mathrm{NA} = n_0 \sin \theta_\mathrm{a} \,, \tag{7.2}$$

where n_0 is the index of refraction outside the fiber ($n_0 = 1$ since we operate in vacuum) and θ_a is the acceptance angle. The acceptance angle is measured from the central

---

[1] For the two-level fluctuator measurements we are in the range of 0 to 50 nW.

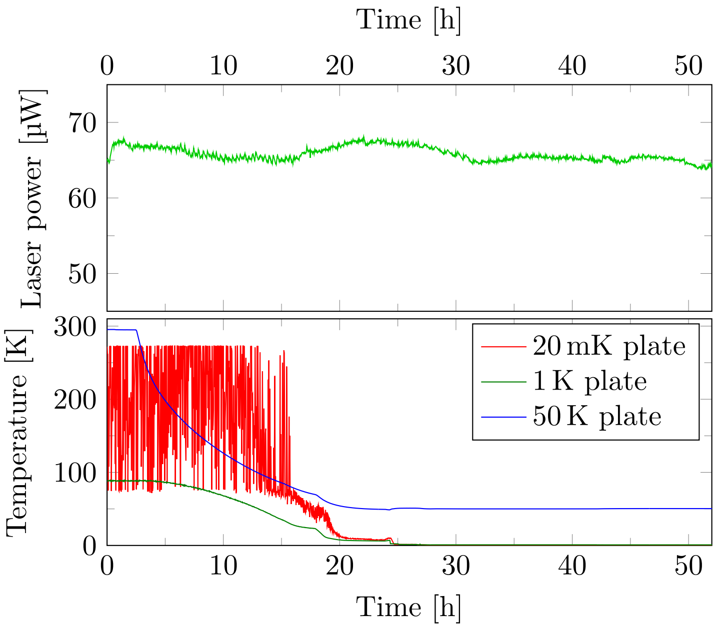

Figure 7.3.: The upper plot depicts the light power transmitted through an optical fiber during a full cool-down. The fiber goes from the top of the cryostat (which is at room temperature) to the 20 mK stage and then back up again to the top where the laser power has been measured with a power meter. The lower plot shows the corresponding temperatures measured at three different stages during the cool-down. We don't see any dependency of transmitted light power on temperature and the fluctuations, which are about 6.5 % of the maximum power, are from the laser itself.

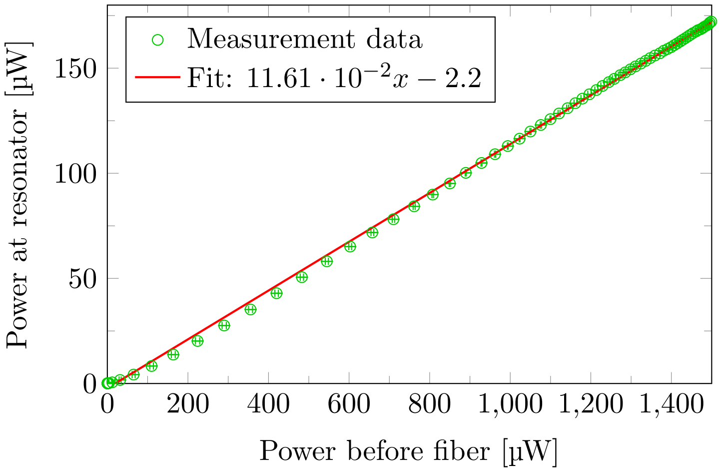

Figure 7.4.: Measurement to determine the loss of laser power both from coupling into the fiber and the optical vacuum feedthrough (commercially bought SMA couplers from *Optocon*) on top of the dilution refrigerator. We measured the laser power with a power meter once directly before coupling into the fiber and once at the position of the resonator, see also Fig. 7.9. The output power at the resonator grows linearly with the input power and from the fit we see that about 88 percent of the incident light is lost.

axis of the fiber and determines the angle at which light can either be transmitted into or emitted from the fiber, see Fig. 7.1. For a numerical aperture NA $= 0.48$ and a distance of $h \approx 3.3\,\mathrm{mm}$ from the fiber to the resonator the spot size in our system is given by $d_{\mathrm{spot}} \approx 3.6\,\mathrm{mm}$.

Since we can't measure the light power reaching the resonator while the dilution refrigerator is cooled down, we have to calibrate with measurements when the setup is warmed up and can be opened. Therefore, it is important to know if the cool-down process has any influence on the light transmission. To test the temperature dependence we built a second fiber that goes from the top of the dilution refrigerator to the lowest temperature stage and the up again to the SMA couplers where the power can be measured with a power meter. The results are shown in Fig. 7.3 and we conclude that temperature effects can be neglected and the results from the measurements during the warmed-up period can be applied.

The stability of the laser on the other hand could definitely be better, which is the reason why there are considerations to build a PID[2] controller for future measurements.

Another crucial point is the determination of very small laser powers. According to the data sheet our power meter only allows measurements from 50 nW upward[3],

---

[2] PID is the acronym for proportional-integral-derivative.

[3] In our measurements about 80 nW was the lowest possible value to be measured with the power meter directly.

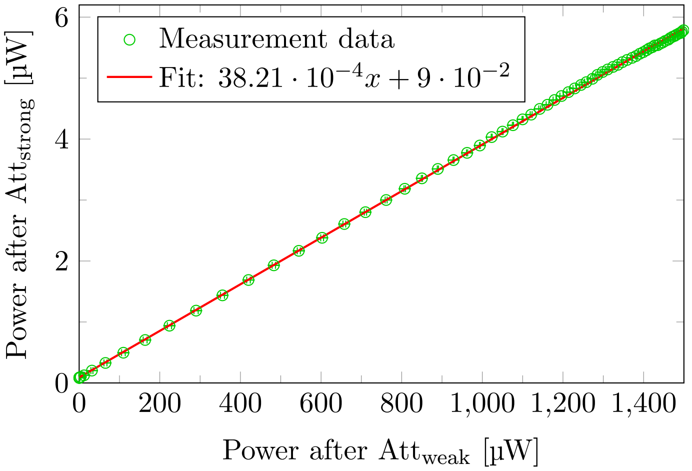

Figure 7.5.: For most of the measurements we use one of the two attenuators $\mathrm{Att}_{\mathrm{weak}}$ or $\mathrm{Att}_{\mathrm{strong}}$. The attenuation ratio of those two attenuators displays a linear behavior over the full range of measured light powers. The result of a linear fit gives an attenuation factor of about 260 for $\mathrm{Att}_{\mathrm{strong}}$ compared to $\mathrm{Att}_{\mathrm{weak}}$.

but two-level fluctuator (TLF) effects take place below this limit[4]. So we have to extrapolate from measurements with higher powers. Figure 7.4 depicts the ratio of the laser power before coupling into the fiber and the laser power at the resonator. The dependency exhibits a linear behavior although unfortunately at low laser powers there seems to be a small deviation from the linear decline and the losses seem to be a bit larger. Since the deviation is only small we will nevertheless assume a linear dependency even for low laser powers. We also see that coupling into the fiber plus coupling into the cryostat causes quite a lot of loss, in that only about 12 % of the incident power get transmitted to the resonator.

To get to the low power regime in the experiment we switch the weak optical attenuator $\mathrm{Att}_{\mathrm{weak}}$ (filters out half of the incident power) with the strongly attenuating $\mathrm{Att}_{\mathrm{strong}}$. The attenuation ratio of those two attenuators is linear over the full range of incident optical power, as can be seen from the measurement data in Fig. 7.5, and from the fit we can extract a factor of about 260 to scale down the measurements for higher powers to small powers.

7.3. Microwave setup

Similar to the optical setup the microwave setup can be divided into two parts. There is the wiring leading to and from the resonator inside the dilution refrigerator and then there is the microwave source and the microwave detection system outside (see

---

[4] We know this from prior measurements on a resonator of a similar design done by Koller [Kol12].

Fig. 7.9).

We'll start with the microwave wiring in the dilution refrigerator. The microwave signal is transmitted into the cryostat via a standard SMA vacuum feedthrough (details to the used components can be found in Table 7.1). Since keeping low base temperatures is crucial, the microwave line connecting the room temperature stage with the 20 mK stage consists of stainless steel cables which have a small heat conductivity while still retaining sufficient electrical conductivity. At room temperature the cable loss from the input port of the dilution refrigerator to the resonator is about -9 dBm. Additionally there are three attenuators, with a total of −60 dB attenuation, on the downward line in order to minimize the thermal noise[5].

From Fig. 7.9 we also see, that within the same temperature stage copper cables were used. In this case good heat conductivity is actually desired, because at the lowest temperature stage the microwave line helps cooling the resonator to the base temperature. Due to their much better electrical (as well as thermal) conductivity the signal loss is equally lowered.[6] Furthermore, the copper cables are easier to bend and to solder, as well as more economical in costs.

The resonator itself is mounted in a gold-plated copper box (the "sarcophagus"), as can be seen in Fig. 7.6. The sarcophagus fulfills several functions, it shields the resonator from outside electrical fields as well as dirt in general and because of its good thermal conductivity also acts as heat sink for the resonator. According to simulations the resonance frequencies of cavity modes introduced by the sample box are beyond 10 GHz and therefore shouldn't influence measurements of the resonator at approximately 3 GHz.

The output signal of the resonator is amplified once inside the dilution refrigerator with a LNF amplifier from *Low Noise Factory* (G = 42 dB) and then again at the top of the cryostat with an AFS amplifier from *Miteq* (G = 32 dB).

The microwave wiring outside of the dilution fridge depends on whether we want to do spectroscopic measurements or measure time-dependent processes. For the former we use vector network analyzer (VNA) whereas for the latter an homodyne detection scheme is applied.

7.3.1. The vector network analyzer and spectroscopic measurements

For the experiments where the resonator is irradiated with a constant light flux and the response is not time-dependent a vector network analyzer (VNA) is used. The VNA functions simultaneously as signal generator and as microwave detection system. It supplies coherent continuous wave signals and measures the S-parameters of the scattering matrix from Eq. (2.12).

A spectroscopic measurement of the resonator without light irradiation can be seen in Fig. 7.7. Usually we only consider the forward scattering parameter S_{21}, which tells us something about the transmission from port 1 to port 2. As we already know from

---

[5] Details on the necessity of attenuation are covered in the thesis of Schuster [Sch07].

[6] More information on the heat conductivity and attenuation of copper and stainless steel cables can be found in the thesis of Fink [Fin10].

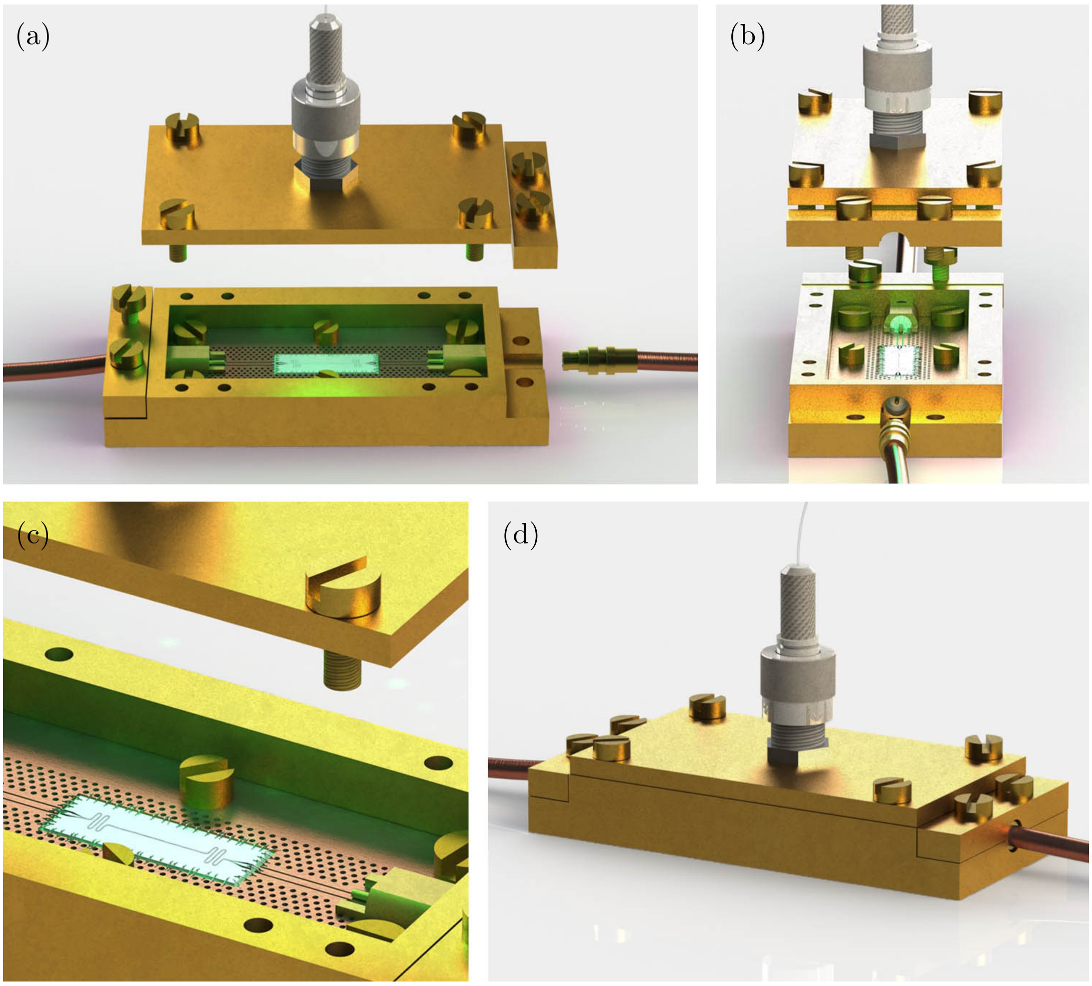

Figure 7.6.: A rendering of the resonator and the gold-plated copper sample box. (a) View of the resonator with an opened lid. At the top we see the optical fiber and the SMA connector that is screwed onto the lid of the sample box. The resonator is placed inside the gap of a printed circuit board (PCB), which connects it via Mini SMP connectors to to microwave input and output lines. (b) View from a different angle. (c) Close-up of the resonator were we can see the aluminum bonds that anchor the chip to the PCB and therefore also connect it to ground. (d) The fully assembled sample box.

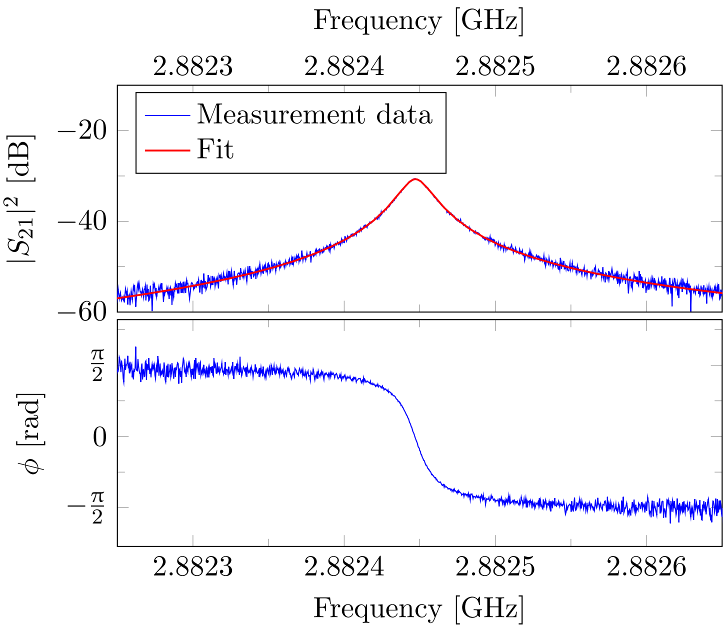

Figure 7.7.: Spectroscopic measurement of the resonator with the vector network analyzer (VNA). The upper plot shows the magnitude $|S_{21}(t)|^2 = (\mathrm{Re}\, S_{21})^2 + (\mathrm{Im}\, S_{21})^2$ and below is the phase $\phi = \tan^{-1} \frac{\mathrm{Im}\, S_{21}}{\mathrm{Re}\, S_{21}}$, where we have shifted the phase by a constant factor so that $\phi(f_0) = 0$. The resonance frequency $f_0 = 2.882\,447\,\mathrm{GHz}$ and quality factor $Q_{\mathrm{tot}} = 137\,851$ are obtained by a non-linear least squares fit with a skewed Lorentzian.

Eq. (3.9) and (3.11) the resonance of a half wave transmission line resonator can be fitted with a Lorentzian function

$$|S_{21}|^2 = \frac{|A|^2}{1 + 4Q_{\mathrm{tot}}^2 (\Delta f / f_0)^2}\,, \tag{7.3}$$

where the fit parameters are the amplitude A, the resonance frequency f_0 and the quality factor Q_{tot}.

Unfortunately often some background signals (e. g. from nearby resonances) lead to deviations from the ideal behavior and so-called Fano resonances occur. To extract the resonance frequency f_0 and quality factor Q_{tot} more accurately from the transmission data, we use a non-linear least squares fit with a skewed Lorentzian [Gao08; PA98]

$$|S_{21}|^2 = A_1 + A_2(f - f_0) + \frac{A_3 + A_4(f - f_0)}{1 + 4Q_{\mathrm{tot}}^2 (\Delta f / f_0)^2}\,, \tag{7.4}$$

where the fit parameters are now the various amplitudes A_i, the resonance frequency f_0 and the quality factor Q_{tot}.

7.3.2. Homodyne detection of time-dependent processes

For very fast time-dependent processes where the VNA isn't sufficient any more we have implemented an homodyne detection scheme exploiting the properties of an quadrature mixer[7]. Once again the basic setup is displayed in Fig. 7.9.

An quadrature mixer is a four port device that mixes the RF signal coming from the dilution fridge with the signal of a local oscillator (LO). The output of the device is an in-phase component ($I(t)$), proportional to the real part of the original RF signal, and a quadrature component ($Q(t)$), proportional to the imaginary part of the original RF signal. Using this we can calculate the amplitude and phase of the output signal

$$|S_{21}(t)|^2 = |I(t) + \mathrm{j}Q(t)|^2 \,, \tag{7.5}$$

$$\phi(t) = \tan^{-1} \frac{Q(t)}{I(t)} \,. \tag{7.6}$$

The ingenious idea behind the mixing of signals is that very high frequencies can be down-converted to lower frequencies, where detection is a lot easier. Mathematically the underlying principle can easily be understood by multiplying two cosine functions

$$\begin{aligned} \cos\left(\omega_{\mathrm{RF}} t + \phi(t)\right) \cdot \cos \omega_{\mathrm{LO}} t =& \frac{1}{2} \left[\cos\left(\left(\omega_{\mathrm{RF}} - \omega_{\mathrm{LO}}\right) t + \phi(t)\right)\right. \\ & \left. + \cos\left(\left(\omega_{\mathrm{RF}} + \omega_{\mathrm{LO}}\right) t + \phi(t)\right)\right] \,, \end{aligned} \tag{7.7}$$

where ω_{LO} is the frequency at the LO input, ω_{RF} is the frequency at the RF input and ϕ is just some additional phase, which later on will be a phase-lag caused by the resonator. By applying a low-pass filter to suppress the high frequency term we immediately recognize the down-conversion. Homodyne detection is now defined by the fact that the LO frequency equals the RF frequency. In the experimental setup this is done by installing a splitter directly after the signal generator. The first line runs through a digital attenuator, a fast microwave switch and the dilution refrigerator afterward being connected to the RF input of the quadrature mixer. The second line is directly connected to the LO input[8].

After the quadrature mixer, the low-pass filters and preamplification the detection and measurement of the down-converted signals is done with a digitizer card from *Acqiris*. A typical measurement using this homodyne detection scheme is depicted in Fig. 7.8.

---

[7] Also called IQ mixer.

[8] To prevent ground-loops we installed DC blocks right before the RF and LO inputs of the quadrature mixer.

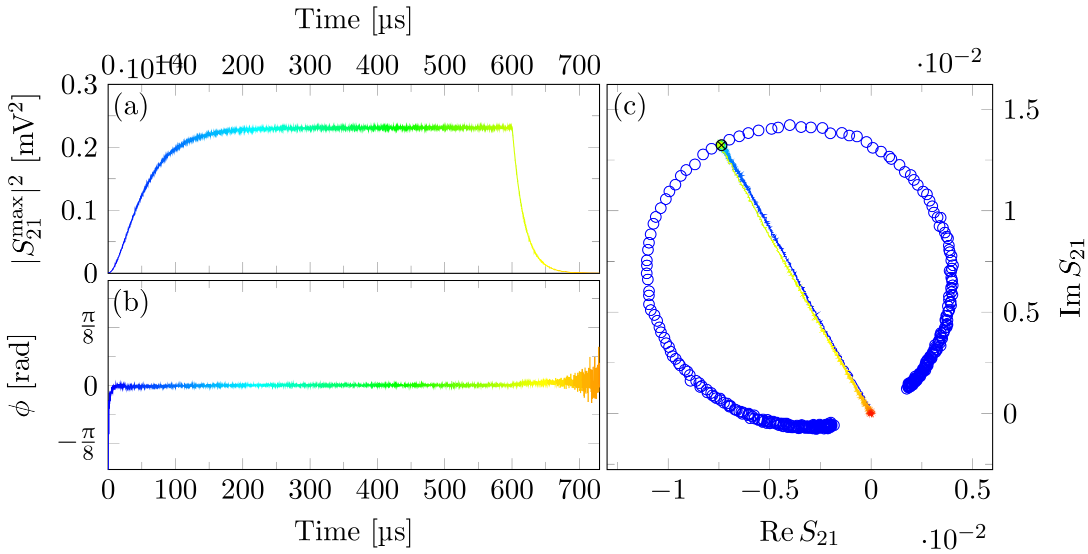

Figure 7.8.: Time-dependent measurement (in the absence of light) at the resonance frequency f_0 of the resonator using the homodyne detection scheme, where the color is coding the elapsed time. (a) Shows $|S_{21}(f = f_0, t)|^2 = |S_{21}^{\max}(t)|^2$ and we clearly see the opening of the switch that is blocking the microwave source at $t = 0\,\mu\text{s}$, then the reaching of an equilibrium state and finally the closing of the switch at $t = 600\,\mu\text{s}$. In (b) the phase $\phi = \tan^{-1}\frac{Q(t)}{I(t)}$ is depicted. (c) An alternative way to look at the transmission data: Instead of plotting the amplitude and the phase, the data is plotted in the complex plane $(x(t), y(t)) = (\operatorname{Re} S_{21}(f_0, t), \operatorname{Im} S_{21}(f_0, t))$. Using the same color code we start at (0,0) (blue) and then, during the transient phenomenon of the resonator, move toward the steady state of the system at the black crossed-out circle (turquoise to green). After closing the switch the resonator relaxes back to the starting point at(0,0) (red). In the complex plane the scattering parameter S_{21} traces out a circle for a frequency range near the resonance frequency. This blue circle represents the same information as a spectroscopic measurement, where we usually plot $|S_{21}(f)|^2 = (\operatorname{Re} S_{21}(f))^2 + (\operatorname{Im} S_{21}(f))^2$ (see Fig. 7.7). A point on the circle is given by $(x, y) = (\operatorname{Re} S_{21}(f), \operatorname{Im} S_{21}(f))$ and varying the frequency from $f_0 - \frac{f_\text{range}}{2}$ to $f_0 + \frac{f_\text{range}}{2}$ yields the complete circle. The resonance frequency f_0 is indicated by the black crossed-out circle.

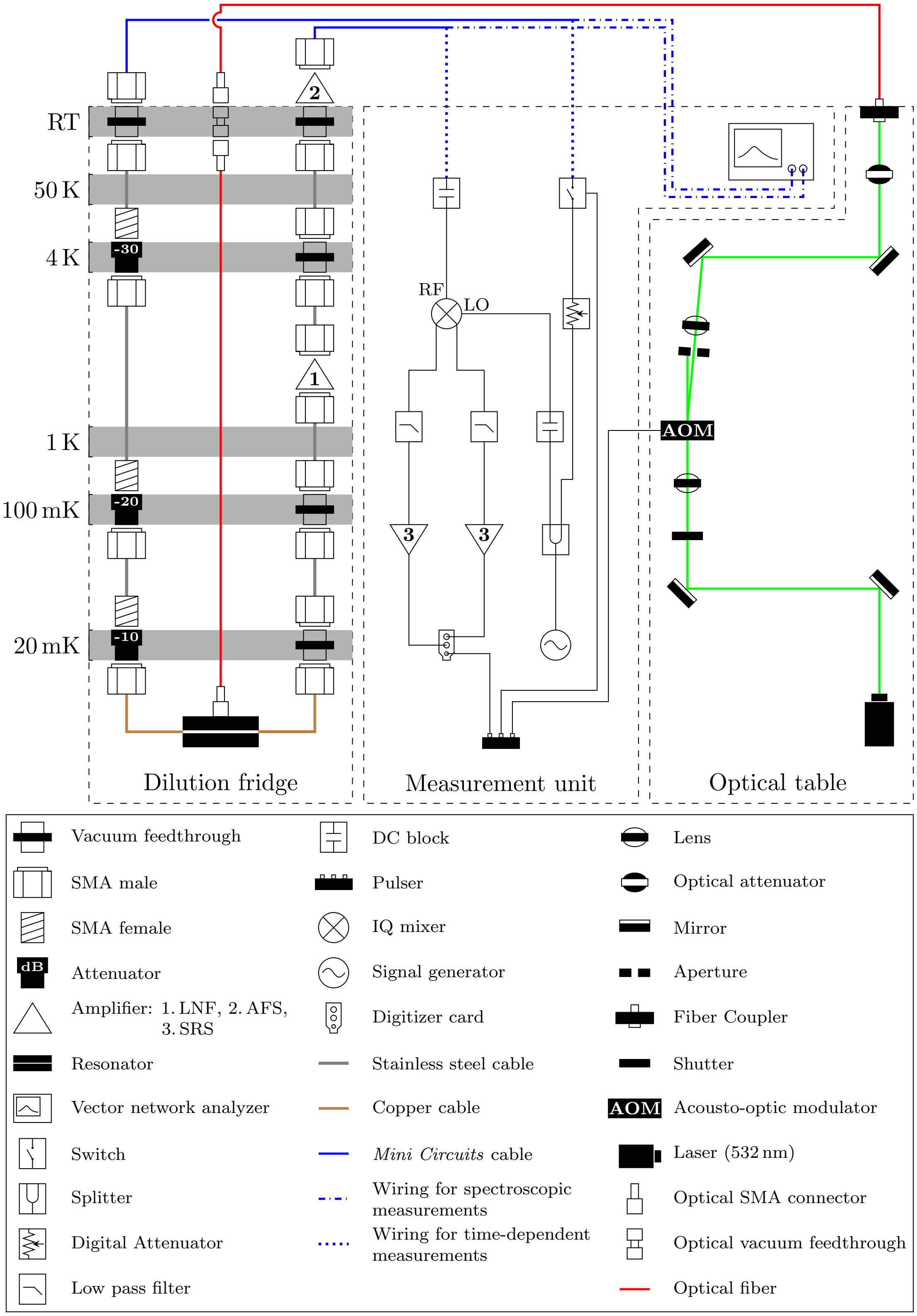

Figure 7.9.: Experimental setup

Table 7.1.: Part specifications.

Part	Model
Resonator	R3-3-111-1, see Sec. 3.4
Amplifier 1	LNF-LNC1.8-2.8A, *Low Noise Factory*
Amplifier 2	AFS3-02000400-06-10P-4, *Miteq*
Amplifier 3	SR445A 350 MHz preamplifier, *Stanford Research Systems*
Copper cable	UT-085C, *Micro-Coax*
Stainless steel cable	UT-085-SS-SS, *Micro-Coax*
Mini Circuits cable	CBL-XXX-SMSM+, *Mini Circuits*
Splitter	ZAPD-4+, *Mini Circuits*
Switch	ZASWA-2-50DR+, *Mini Circuits*
Digital Attenuator	ZX76-15R5-SP+, *Mini Circuits*
Low pass filter	VLFX-300, *Mini Circuits*
Vacuum feedthrough	SM4944, *Fairview Microwave Inc.*
Attenuators	SA18H-XX, *Fairview Microwave Inc.*
DC block	SD3258, *Fairview Microwave Inc.*
quadrature mixer	IQ-0255, *Marki microwave*
Vector network analyzer	E5071, *Agilent*
Signal generator	E8257C PSG, *Agilent*
Digitizer card	U1084A Acqiris card, *Agilent*
Acousto-optic modulator	3350-198, *Crystal Technology*
Optical fiber	BFL48-200 (200 µm core), *Thorlabs*
Laser (532 nm)	MXL-III-532, *Changchun New Industries*
Pulser	FPGA based pulser card, home-built

8. Results

In this chapter the results of our experiments will be collected and discussed. The focus will be on the change of resonator properties due to light irradiation with a green 532 nm laser. Nevertheless, at the beginning we will start by looking at the influence of microwave probing power and dilution fridge temperature. Afterward continuous light irradiation will be discussed and the final parts of this chapter will be devoted to pulsed light measurements.

Before we get to the measurement results let's briefly recapitulate what it is that we want to measure. The most important properties to characterize a resonator are its resonance frequency f_0, the quality factor Q_{tot} and the amplitude on resonance $|S_{21}(f_0)|$. A perturbation, e. g. light irradiation, will change those parameters according to Ch. 5 and 6. The microscopic reasons for this change are the excitation of two-level fluctuators (TLFs) and quasiparticles. The former are most likely metastable atomic states in amorphous layers or at the interface of the superconductor. The latter are created by breaking apart Cooper pairs, the charge carriers of superconductivity.

To study those excitations we basically perform two different sorts of measurements: Spectroscopic measurements with the vector network analyzer (VNA) and time-dependent measurements with the digitizer card. Figure 8.1 depicts the difference between the spectroscopic measurements and the time-dependent measurements. For the power and temperature dependent experiments as well as the experiments with a continuous light flux, we have enough time to do a full spectroscopic measurement. We can fit the resonances and directly extract the shifted resonance frequency f_0^*, quality factor Q_{tot} and amplitude $|S_{21}(f_0^*)|$. For the pulsed light measurements this is not an option, since there is not enough time to scan a whole range of frequencies and record a trace. Instead the frequency is set to the undisturbed resonance frequency f_0 at which the amplitude $|S_{21}^{\mathrm{max}}(f_0, t)|$ and the phase $\phi(f_0, t)$ is measured.[1]

8.1. Microwave probing power and temperature

Taking measurements on the resonator[2] is by itself a perturbation of the system. To measure means sending microwaves through the resonator. However, not the entire microwave probing power P_{mw} entering the resonator is transmitted. Some part of the inserted power will excite TLFs. To quantify the extent of excitations through the microwave probing power we have measured the shift of the resonance frequency

---

[1] Recording a full trace with the VNA is on the order of seconds, therefore faster processes have to be measured applying a different technique, e. g. quadrature mixing. See also Sec. 7.3.

[2] All measurements have been performed with the resonator R3-3-111-1, although similar results have been obtained with different resonator models.

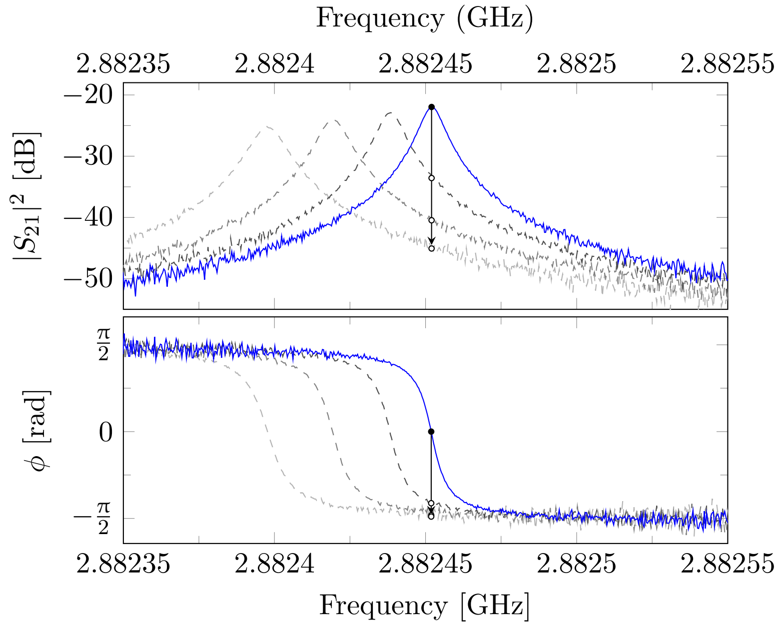

Figure 8.1.: Light irradiation, temperature change or even a change in the microwave probing power influences the quality factor Q_{tot} as well as the resonance frequency f_0, thereby also changing the phase ϕ. For the measurements with a continuous perturbation we perform a spectroscopic measurement from which we extract the current resonant frequency f_0^*, the quality factor Q_{tot} and the amplitude at the current resonance frequency $|S_{21}^*|^2$. For the time-dependent measurements we set the measurement frequency to the resonance frequency of the undisturbed system (blue) and then measure the amplitude and phase response to a light pulse of the perturbed system (gray).

δf_0, the change of Q_{tot} and the amplitude at the shifted resonance frequency using spectroscopic measurements (see Fig. 8.2). The resonance frequency itself should not be dependent on the microwave probing power. Due to the frequency response of the resonator microwaves are transmitted in a very narrow range around the resonance frequency f_0. Therefore only TLFs close to the resonance frequency should be excited, which wouldn't cause a shift of the resonance frequency. However, the measurement data clearly depicts a downward shift, as can be seen from Fig. 8.2. There has to be a secondary process exciting TLFs with resonance frequencies lower than the resonator's undisturbed resonance frequency f_0. The cause for this excitation of TLFs is probably a heating effect, where part of the inserted microwave power generates a small rise of the resonator's temperature. The created phonons then in turn excite TLFs with resonance frequencies below f_0. The power dependency of the inverse quality factor Q_{tot}^{-1}

Table 8.1.: Two-level fluctuator fit functions with the fit parameters $a, \dots, h$.

	$1/Q$	δf_0
T	$a \tanh\left(\frac{\hbar\omega}{2k_\mathrm{B}T}\right) + b$	$c\left[\mathrm{Re}\,\Psi\left(\frac{1}{2} - \frac{\hbar\omega}{2\mathrm{j}\pi k_\mathrm{B}(T-d)}\right) - \ln \frac{\hbar\omega}{2\pi k_\mathrm{B}(T-d)}\right] + e$
$^{1)}P_\mathrm{lp}$	$a \tanh(\frac{c}{P_\mathrm{lp}-d}) + b$	$e\left[\mathrm{Re}\,\Psi\left(\frac{1}{2} - \frac{f}{\mathrm{j}(P_\mathrm{lp}-g)}\right) - \ln \frac{f}{P_\mathrm{lp}-g}\right] + h$
$^{2)}P_\mathrm{lp}$	$a \tanh(\frac{c}{\sqrt[4]{P_\mathrm{lp}-d}}) + b$	$e\left[\mathrm{Re}\,\Psi\left(\frac{1}{2} - \frac{f}{\mathrm{j}\sqrt[4]{P_\mathrm{lp}-g}}\right) - \ln \frac{f}{\sqrt[4]{P_\mathrm{lp}-g}}\right] + h$
P_mw	$a\,(1 + bP_\mathrm{mw})^c$	——

at a fixed temperature is determined by a function proportional to [Phi87; Mac+10]

$$f(P_\mathrm{mw}) = \left(1 + \frac{P_\mathrm{mw}}{P^0_\mathrm{mw}}\right)^\varphi , \tag{8.1}$$

with P^0_mw being the probing power where effects on Q^{-1}_tot become negligible. The two-level system theory predicts a value of $\varphi_\mathrm{th} = -0.5$ for the exponent [Phi87]. A fit to the data results in $\varphi = -0.15$, which deviates from the theoretical value but agrees with similar measurements carried out by Macha et al. [Mac+10] and Koller [Kol12].[3] The increase of the quality factor can be interpreted in the following way. Given that the temperature is small enough, most of the two-level fluctuators will be in the lower energy state. When we are probing the resonator with microwaves, some part of the inserted power will be lost due to the excitation of TLFs mentioned above. Increasing the probing power causes more and more TLFs to be excited thereby removing the source of the loss. If we only considered TLF effects the rise in the quality factor would continue until all TLFs are in an incoherent 50:50 superposition, at which point the quality factor saturates at its maximum value.[4]

Equally important as the impact of the microwave probing power is the knowledge about the influence of the dilution refrigerator temperature on the CPW resonator (also Fig. 8.2). Therefore we have measured the characteristics of the resonator in the temperature range from 50 mK to 450 mK. The resonance frequency shift shows a shape characteristic for the two-level fluctuator model. For small temperatures only TLFs with resonance frequencies below the resonator frequency f_0 get excited, which causes a downward shift of the overall resonance frequency. With increasing temperature also TLFs with frequencies above f_0 will be excited, now causing a shift in the opposite direction. From TLS theory the position of the minimum is determined by $\frac{2k_\mathrm{B}T}{\hbar\omega} \approx 0.9$, see Fig. 6.3. Inserting $\omega \approx 2.882\,39\,\mathrm{GHz}$ and solving for the temperature gives $T \approx 62\,\mathrm{mK}$. For unknown reasons the measurement data shows a slightly higher temperature for the minimum at about $T \approx 100\,\mathrm{mK}$. Possible sources of error are the position of the temperature sensors, which are not directly next to the resonator, and

---

[3] See also Table 8.1 and 8.2.

[4] We will see later on that at some point quasiparticle excitation effects take over and will cause a decrease of the quality factor.

Table 8.2.: Two-level fluctuator fit parameters.

	Parameters
T	$a = 6.3 \cdot 10^{-6}$, $b = 1.9 \cdot 10^{-6}$, $c = 3996$, $d = 4.3 \cdot 10^{-2}$, $e = -1197$
$^{1)}P_{\mathrm{lp}}$	$a = 4.0 \cdot 10^{-5}$, $b = 2.9 \cdot 10^{-6}$, $c = 0.172$, $d = 0.26$, $e = -$, $f = -$, $g = -$, $h = -$
$^{2)}P_{\mathrm{lp}}$	$a = 2.2 \cdot 10^{-5}$, $b = 2.1 \cdot 10^{-6}$, $c = 0.114$, $d = -1.3$, $e = 9626$, $f = 0.364$, $g = 0.3$, $h = 346$
P_{mw}	$a = 8.6 \cdot 10^{-6}$, $b = 1.2 \cdot 10^{8}$, $c = -0.15$

the position of the heaters, which regulate the temperature of the dilution refrigerator. Due to this fact the measured temperature might differ from the actual temperature at the resonator. Fitting with Eq. (6.12) yields a qualitative agreement, but for low temperatures the predicted resonance frequency shift is too small while it is too large for temperatures above 350 mK. Furthermore we have to introduce a temperature shift $d = 43 \pm 15\,\mathrm{mK}$ in the fit model (see Table 8.1 and 8.2). The quality factor Q_{tot} on the other hand is very well described with the TLF model given by Eq. (6.13).[5] The prefactors $a = F\delta^0_{\mathrm{TLS}}$ and $c = f_0 F\delta^0_{\mathrm{TLS}}/\pi$ of the fit models are in good agreement with each other. Calculating the factor c by inserting a into the previous equation results in $c_a = 5735$ which is close to the fitted value of $c = 3996$. The amplitude $|S^*_{21}|^2$ behaves very similar to the quality factor for both of the measurements, which is not that surprising since Eq. (5.22) tells us that the amplitude only reacts to changes in the quality factor for small perturbations.

The resonator response to different microwave probing powers and temperatures illustrates, that it is necessary to measure at microwave probing powers $\leq -80\,\mathrm{dBm}$ and the lowest possible temperature to observe the complete two-level fluctuator response. Almost all of the following measurements have been carried out close to $-80\,\mathrm{dBm}$.[6] The downside of smaller microwave probing powers is the inferior signal-to-noise ratio (SNR).

8.2. Continuous light irradiation

Now we turn to the effects of light irradiation by a green laser (532 nm) on the resonator. We will distinguish between a low and a high laser power regime. For the low laser power measurements the strong attenuator $\mathrm{Att}_{\mathrm{strong}}$ is used, see Fig. 7.5 and 7.9. This allows us to vary the optical power P_{lp} in between a few nanowatt and 300 nW. In the high laser power regime the weak attenuator $\mathrm{Att}_{\mathrm{weak}}$ is mounted on the optical

---

[5] For all fits of the quality factor, we actually fitted $1/Q_{\mathrm{tot}}$ and then inverted the fit.

[6] One exception are the time-dependent measurements in the high power regime in Sec. 8.3.1, where we wanted to measure quasiparticle effects. Due to the better signal-to-noise ratio a microwave probing power of about $-70\,\mathrm{dBm}$ was chosen.

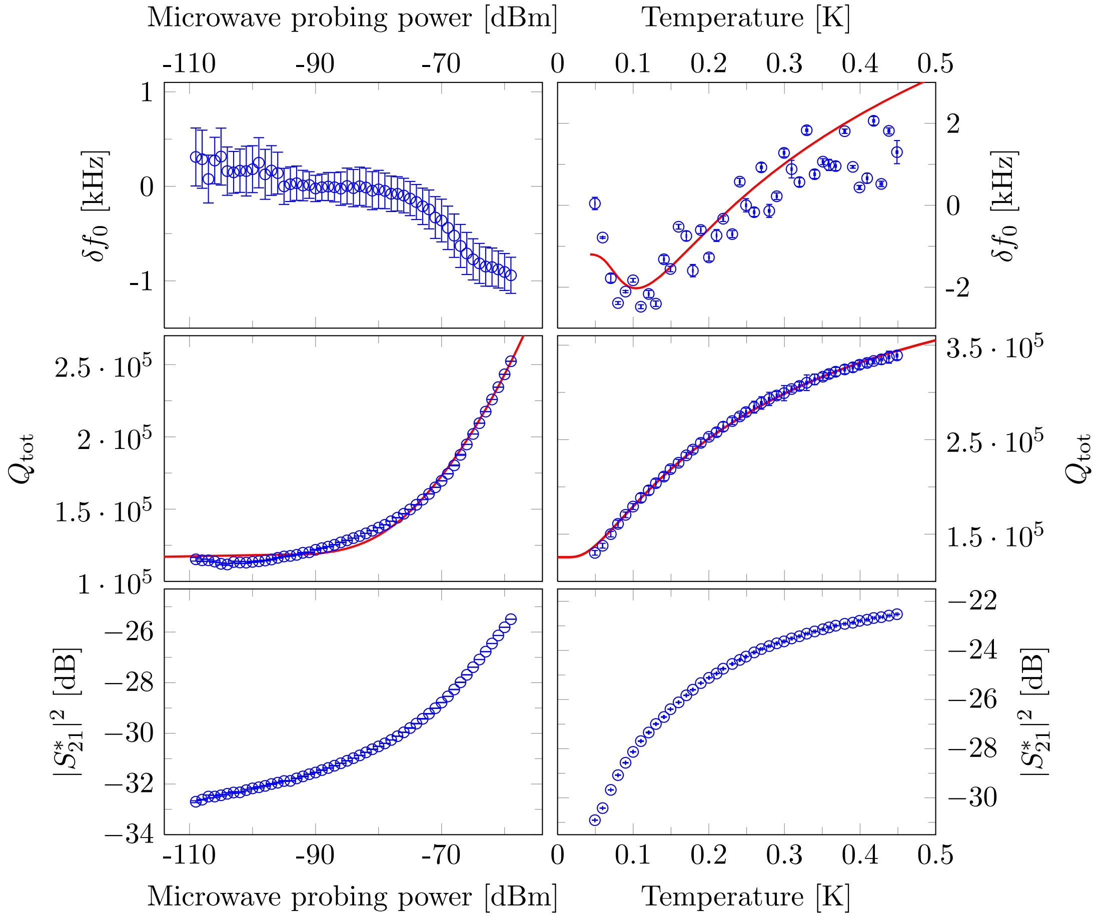

(a) (b)

Figure 8.2.: Dependency of the resonator properties on the microwave probing power and the temperature, where we can clearly identify two-level fluctuator (TLF) effects. (a) Since only microwaves in a narrow frequency range around the resonance frequency f_0 are transmitted through the resonator no frequency shift would be expected. Nevertheless a shift to lower frequencies can be observed which probably stems from a heating effect caused by the microwaves. This causes an excitation of TLFs with a resonance frequency lower than the resonator, leading to a downward shift. The power dependence of the quality factor is given by Eq. (8.1). As expected from Eq. (5.22) the maximum amplitude $|S_{21}^*|^2$ mostly follows the quality factor. (b) The resonance frequency shift shows the same behavior as predicted by Eq. (6.12) but the data exhibits a larger shift downward in the beginning and a slower shift upward above 350 mK. Unlike the resonance frequency the quality factor Q_{tot} agrees very well with Eq. (6.13).

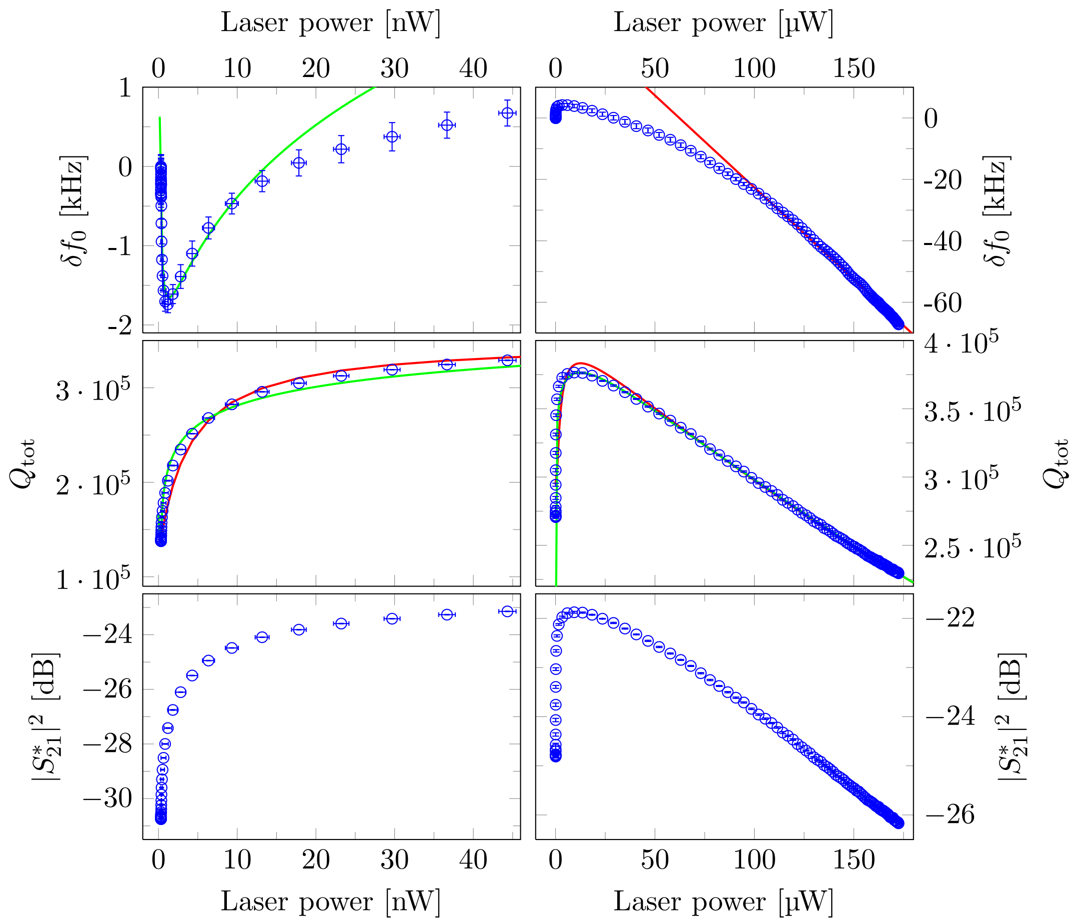

(a) (b)

Figure 8.3.: Resonator properties under constant light irradiation. (a) The left column shows the results from measurements with a very low laser power, where two-level fluctuator (TLF) effects govern the resonator response. The red fits correspond to the fit functions of $^{1)}P_{\mathrm{lp}}$ while the green fits correspond to the fit functions of $^{2)}P_{\mathrm{lp}}$ in Table 8.1. A fit of the frequency shift was not feasible with the $^{1)}P_{\mathrm{lp}}$ fit model. The green fit agrees well with the characteristic TLF dip but deviates for higher powers. This deviation cannot be explained by quasiparticle excitation, which would only account for a downward shift of 0.6 Hz per nW (b) For higher optical powers the response is dominated by quasiparticle excitations. According to chapter 5, a linear frequency shift (slope $k = 609\,\mathrm{Hz}/\mu\mathrm{W}$) is expected which is true for powers above 100 µW. The quality factor should be inversely proportional to the laser power. Adding a term of the form $e(P_{\mathrm{lp}} + f)^{-1}$ to the inverse of the TLF fit function (see Table 8.1) produces a good fit (red and green) of the quality factor over the full range of laser powers P_{lp}.

table instead of the strong attenuator, yielding laser powers from a few microwatt to 170 µW.

For continuous light irradiation measurements the laser is set to a specific power[7] and the resonator is probed with the vector network analyzer (VNA) after equilibrium is attained. The results for continuous irradiation are depicted in Fig. 8.3. In the low laser power regime once again the characteristic TLF shape of the frequency shift δf_0 is observed. The magnitude of the downward shift is about 2 kHz. We tried to fit the data by replacing the temperature in Eq. (6.12) with a power dependency. However, a simple substitution of the temperature with a factor proportional to the laser power $T \rightarrow P_{\mathrm{lp}}$ didn't yield usable results.[8] There might be several reasons why the measurement data can't be reproduced with a fit. One problem could be that the small laser powers have never really been measured, but have only been extrapolated from the linear fit in Fig. 7.4. Deviations from the linear slope for small laser powers can influence the shape of the resonance shift curve. It is also possible that photons excite a different spectrum of TLFs than phonons and therefore the resonance shift might not be of the same form as Eq. (6.12) suggests. A slightly different approach is to substitute the temperature with a factor proportional to the fourth root of the power $T \rightarrow \sqrt[4]{P_{\mathrm{lp}}}$. This ansatz is inspired by the Stefan-Boltzmann law for black-body radiation. It states that the total power radiated from a black body is proportional to the temperature to the power of four. For our resonators the situation is inversed. The superconducting CPW resonators are irradiated with a laser power P_{lp} which heats the resonator and increases the temperature. The created phonons in turn excite the TLFs creating the measured response. The first plot in Fig. 8.3 shows that the dip in the frequency shift δf_0 can be fitted after applying the new substitution. For powers above 15 nW the measured behavior differs from the fit. This deviation can't be explained with quasiparticle excitations. From the linear fit in the high power regime it can be determined that quasiparticle excitations cause a downward shift of only 0.6 Hz per nW.[9] The possible causes for this discrepancy are the same as for the linear substitution and have already been mentioned above. The quality factor Q_{tot} agrees very well with the TLF model for both the linear and the non-linear substitution of the temperature. Partly this comes from the fact that, contrary to the resonance frequency shift, the shape of the quality factor shift is not as sensitive to measurement errors and perturbations.

The high laser power regime is governed by the effects of quasiparticle excitations, because most of the two-level fluctuators (TLFs) should already be saturated. According to Eq. (5.14), (5.10), (5.5) and (5.23) the frequency shift is proportional to the variation of the laser power $\delta f_0 \propto \delta P_{\mathrm{lp}}$. The measurement data agrees with this linear dependency for laser powers P_{lp} above 100 µW. For small powers we also see the upward shift from the TLFs. In total a resonance frequency shift of about 65 kHz

---

[7] Actually it is not really the laser that is set to a specific power but rather the acousto-optic modulator (AOM). The AOM controls the amount of power transmitted into the fiber and therefore also onto the resonator.

[8] All fit models for TLFs are summarized in Table 8.1.

[9] See the first plot in the right column of Fig. 8.3.

can be observed. Combining Eq. (5.18), (5.9) and (5.23) shows that the quality factor is inversely proportional to the quasiparticle density and therefore also inversely proportional to the laser power $Q_{\mathrm{tot}} \propto \delta P_{\mathrm{lp}}^{-1}$. As before for the resonance frequency data, an increase of the quality factor caused by TLFs can be observed for small laser powers. Due to this fact we fitted the quality factor with the inverse of the according TLF fit function from Table 8.1 plus a term accounting for quasiparticle excitation $e(P_{\mathrm{lp}} + f)^{-1}$, with the additional fit parameters e and f. Figure 8.3(b) illustrates that the behavior of the quality factor can accurately be described with this function over the full range of laser powers.

8.3. Pulsed laser light

Up to this point we have only dealt with continuous perturbations, e. g. we exposed the resonator to green laser light, waited till equilibrium was reached, then measured the resonator response with the VNA. However, now we want to measure the effects of short laser pulses where the sampling rate of the VNA doesn't suffice anymore and we have to use the digitizer card explained in Sec. 7.3.2.

The measurement process is as follows: The AOM[10] is switched from the continuous mode of operation to the pulsed mode. Applying a TTL[11] pulse from the home-built FPGA[12] pulser card to the AOM is basically like switching the light on and off, but in a very fast way[13]. Then we take a spectroscopic measurement to determine the resonance frequency. This is necessary before every measurement because of two reasons. Firstly there might be some long term resonance frequency drifts due to temperature instabilities of the dilution refrigerator or some other perturbations, but secondly, and by far more important, some light leaks through the AOM even in the "off" state. As we have seen in the section above, even small light powers can have a considerable effect on the resonance frequency and the quality factor of a CPW resonator. Therefore the resonance frequency has to be determined before every measurement and for every new optical power the laser is set to. Subsequently the probing frequency is fixed to the previously attained resonance frequency and the quadratures $I(t)$ and $Q(t)$ are measured during the whole period of opening the microwave switch, reaching equilibrium, applying the laser pulse, waiting until equilibrium is reached again and the closing of the microwave switch. From the quadratures the time-dependent amplitude $|S_{21}^{\mathrm{max}}(t)|^2$ and phase $\phi(t)$ are calculated. Furthermore the data will also be plotted in the complex plane offering a different perspective. One advantage of this view is given by the fact that it is relatively easy to tell if we hit the resonance frequency of the system or not. If we are on resonance the sections of the data corresponding to the opening and closing of the microwave switch (red and blue) should be congruent with each other and pass through the center of the circle, see Fig. 7.8 for more information.

---

[10] The AOM is briefly explained in Sec. 7.2.

[11] Transistor-transistor logic.

[12] Field-programmable gate array.

[13] See Fig. 7.2.

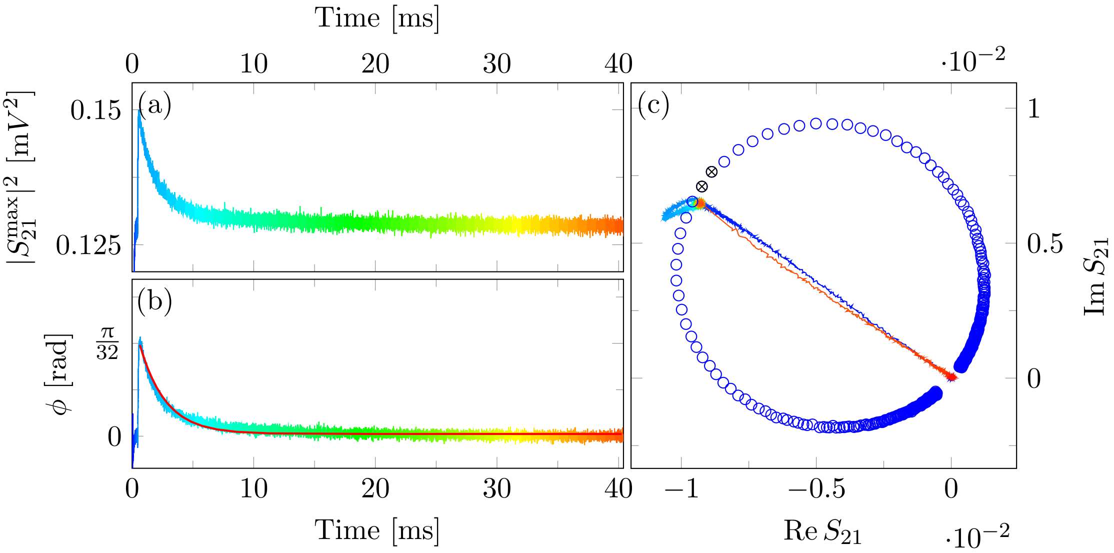

Figure 8.4.: Time-dependent measurement of the amplitude and phase at the resonance frequency f_0 for a 1 µs laser pulse with a power of 170 µW. Due to the "high" power we expect to be in the regime governed by quasiparticles excitation, see Fig. 8.3. (a) Interestingly the behavior of the amplitude is still dominated by TLF effects otherwise a decrease of the amplitude should be observed. (b) From the exponential fit (red) of the phase a quasiparticle lifetime of about 2 ms is calculated. (c) Plot of the data in the complex plane. The two points marked with black crossed-out circles are closest to the undisturbed resonance frequency f_0. Further information on the complex plot can be found in the caption of Fig. 7.8.

As in the case of continuous irradiation we will differentiate between a high (170 µW) and a low (260 nW) laser power regime. The former serves to investigate quasiparticle excitations while the latter explores time-dependent TLF effects.

8.3.1. High power regime

For the high power regime an optical power of $P_{\text{lp}} = 170\,\mu\text{W}$ was chosen and we investigated the impact of different pulse lengths from 0.5 µs to 8 µs. The optical power of these measurements corresponds to the outmost right point in the continuous light measurements of Fig. 8.3(b).

The plots of Fig. 8.4 depict the effects of a 1 µs laser pulse. The complex plot immediately shows that we are slightly off-resonance.[14] Since the amplitude is mostly determined by the losses of the system we would expect a reduction of the amplitude

---

[14] In this plot the frequency interval between adjacent points of the blue resonance circle is $\Delta f = 300\,\text{Hz}$. For comparison the bandwidth of the resonator is about $BW \approx 10\,\text{kHz}$.

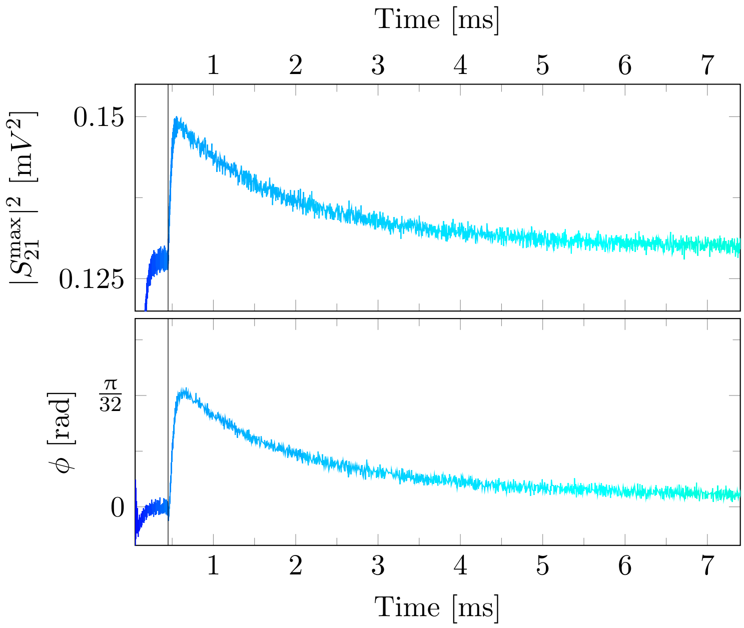

Figure 8.5.: Magnification of the plots from Fig. 8.4. The gray vertical line marks the beginning (and also the end, because of the short pulse length) of the laser pulse.

due to the breaking up of Cooper pairs. Contrary to the anticipated behavior for quasiparticle excitation the amplitude increases. So the amplitude response caused by two-level fluctuators outweighs the quasiparticle effects. The phase response on the other hand is consistent with a shift of the resonance frequency to lower frequencies because of quasiparticle excitation. An exponential fit of the phase yields a quasiparticle lifetime of $\tau_{\mathrm{qp}} = 2\,\mathrm{ms}$. It is difficult to compare this value to theoretical predictions, because at the moment the responsible relaxation processes remain to be understood. Kaplan et al. [Kap+76] tried to explain the quasiparticle lifetimes with the recombination of two quasiparticles and the emission of a phonon. This quasiparticle recombination time τ_{r} is given by[15]

$$\frac{1}{\tau_{\mathrm{r}}} = \frac{1}{\tau_0}\sqrt{\pi}\left(\frac{2\Delta_0}{k_{\mathrm{B}}T_{\mathrm{c}}}\right)^{5/2}\sqrt{\frac{T}{T_{\mathrm{c}}}}\,\mathrm{e}^{-\frac{\Delta_0}{k_{\mathrm{B}}T}}\,, \tag{8.2}$$

where τ_0 is a material dependent electron-phonon relaxation time, Δ_0 is the energy gap of the superconductor at the temperature $T = 0$, k_{B} is Boltzmann's constant and T_{c} is the critical temperature of the superconductor.

To investigate if the behavior of our resonator agrees with the theory of recombination by electron-phonon interaction we also measured the quasiparticle relaxation

---

[15] Note that τ_{r} is the relaxation time for a single quasiparticle, but since always two quasiparticles recombine to a Cooper pair the experimentally measured time is $2\tau_{\mathrm{r}}$.

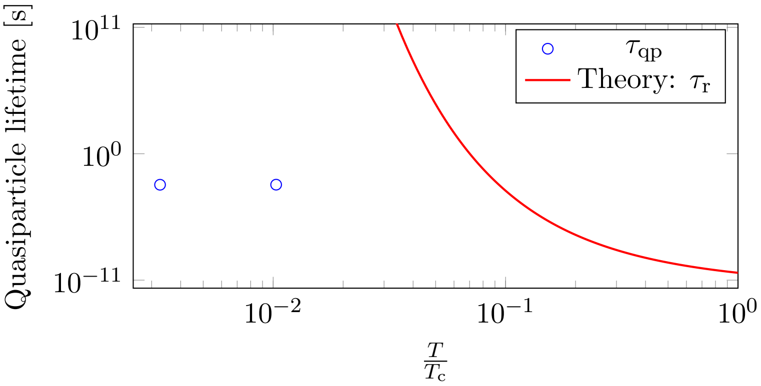

Figure 8.6.: Plot of the measured quasiparticle lifetime τ_{qp} for two different temperatures $T = 30\,\text{mK}$ and $T = 95\,\text{mK}$. For both measurements a relaxation time of $\tau_{\text{qp}} \approx 2\,\text{ms}$ is obtained from an exponential fit. If the quasiparticle relaxation depended solely on electron-phonon relaxation the points should lie on the red curve for the recombination time τ_{r} [Kap+76]. This saturation of quasiparticle lifetimes for temperatures below $T/T_{\text{c}} \approx 0.1$ has also be seen for instance in experiments by Barends et al. [Bar+08], but as of yet the reason for this behavior is not known.

time at a higher temperature of $T = 95\,\text{mK}$. Figure 8.6 shows that the predicted values are much too high for low temperatures.[16] In recent experiments carried out by Barends et al. [Bar+08] a similar response of the relaxation times has been observed. They measured that for temperatures smaller than $T/T_{\text{c}} \lesssim 0.1$ the relaxation times are temperature independent, near $T/T_{\text{c}} \sim 0.15$ a small peak can be seen for some samples and above $T/T_{\text{c}} \gtrsim 0.175$ the quasiparticle relaxation times follow the prediction of Eq. (8.2). For the low temperature saturation of quasiparticle relaxation times a few models have been proposed, e. g. by Reizer [Rei00], but no definitive answer has been provided yet.

The initial increase of the amplitude and phase response depends on the time constant τ_{res} of the resonator. This is the time it takes the resonator to react to any changes or perturbations of the system. The definition of the quality factor in Eq. (3.7) can also be expressed as $Q_{\text{int}} = \omega_0 \tilde{\tau}_{\text{res}}$, where $\tilde{\tau}_{\text{res}}$ is the time until the energy stored in the resonator decays to 1/e of its initial value or it can just as well be the time for the build-up. Consequently $\tau_{\text{res}} = \frac{\tilde{\tau}_{\text{res}}}{2}$ is the characteristic time for the decay (build-up) of the fields. For our resonator this time is calculated to be $\tau_{\text{res}} \approx 33\,\mu\text{s}$ which agrees reasonably well with the values extracted from an exponential fit of the measurement data for the phase $\tau_{\text{res}}^{\phi} \approx 56\,\mu\text{s}$ and the amplitude $\tau_{\text{res}}^{A} \approx 33\,\mu\text{s}$.[17]

---

[16] For the calculation of Eq. (8.2) the electron-phonon relaxation time of niobium $\tau_0 = 0.15\,\text{ns}$ and the critical temperature of niobium $T_{\text{c}} = 9.2$ are used [Kap+76].

[17] For the calculation of τ_{res} the values $f_0 = 2.882\,39\,\text{GHz}$ and $Q_{\text{int}} = 300000$ have been used. The higher quality factor compared to the one from Fig. 7.7 is caused by the light leaking through the AOM.

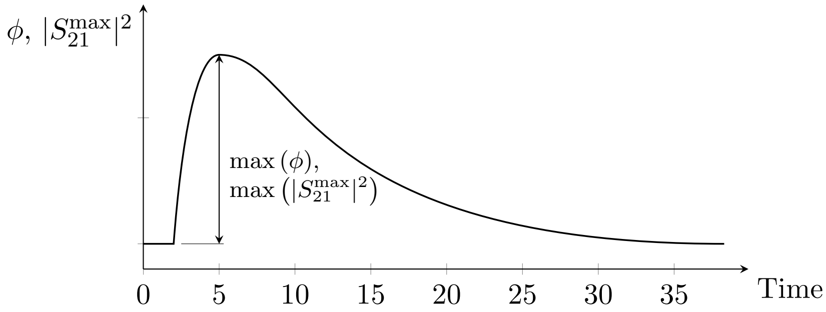

Figure 8.7.: To show the effects of different pulse lengths we have plotted the maximum amplitude and phase shifts in Fig. 8.14 and 8.10. This plot illustrates how we get the data points of those two plots: The maximum displacement of the amplitude and the phase is determined and afterward the shift max (ϕ) and max $\left(|S_{21}^{\max}|^2\right)$ with respect to the equilibrium value is calculated.

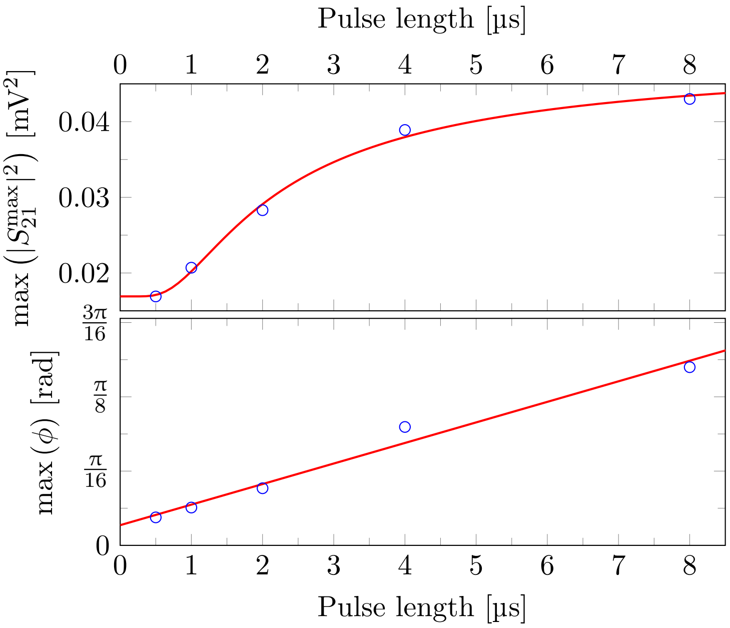

Figure 8.8.: A plot of the maximum amplitude and phase shift for different pulse lengths (or in other words: total energy deposited) at a laser power of 170 µW. The amplitude is fitted with a function corresponding to the TLF model of Eq. 6.13 and the phase is fitted by a linear function with a slope of $k = 0.054\,\mathrm{s}^{-1}$.

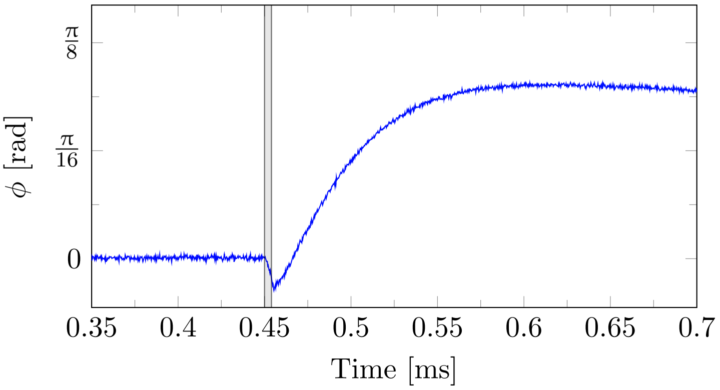

Figure 8.9.: Magnification of a phase plot from laser pulse with 4 µs and a power of 170 µW. The gray area shows again the duration of the laser pulse. For increasing pulse lengths a dip starts to emerge. The origin of this behavior is not understood as of yet.

The results for five different pulse lengths are summarized in Fig. 8.8, where we plotted the maximum shift of the amplitude and the phase for every pulse. With the maximum shift we mean the distance from the equilibrium value to the maximum displacement of the respective variable, see Fig. 8.7. If we neglect the changes in the prefactor of Eq. (5.22) and assume they are small in the considered range of pulse lengths t_{pl} the maximum amplitude follows the change of $\delta Q_{\mathrm{int}}^{-1}$ and can be described by the TLF model $a \tanh \frac{c}{t_{\mathrm{pl}}} + b$. The maximum phase shift shows a linear behavior in the pulse length range from 0.5 µs to 8 µs.

We would also like to point out that for increasing pulse lengths (or laser powers) we noticed the emergence of a dip in the phase shift directly after the start of the laser pulse. This dip is depicted in Fig. 8.9 for a 4 µs laser pulse at a power of 170 µW. To date we have not been able to explain and understand the occurrence of this shift. For very high powers of $P_{\mathrm{lp}} = 3.5\,\mathrm{mW}$ and a pulse length of 8 µs we even measured a phase shift of this dip exceeding 2π, as can be seen in Fig. 8.10. However, the quasiparticle relaxation time agrees with the previous measurements since an exponential fit yields $\tau_{\mathrm{qp}} \approx 2.8\,\mathrm{ms}$. For such high powers a large fraction of the two-level fluctuators is saturated solely from the light leaking through the AOM. Hence a decrease of the amplitude caused by the light pulse can finally be seen. The exact behavior of the amplitude is difficult to describe since the frequency shift, which lowers the amplitude, and the decrease of the quality factor, which lowers the amplitude near the resonance frequency but increases it far off resonance, have to be considered.

8.3.2. Low power regime

In the low power regime we concentrate on measuring time-dependent two-level fluctuator effects. The optical power is set to 260 nW which is just before the turning point in Fig. 8.3(b) where quasiparticle effects start to take over.

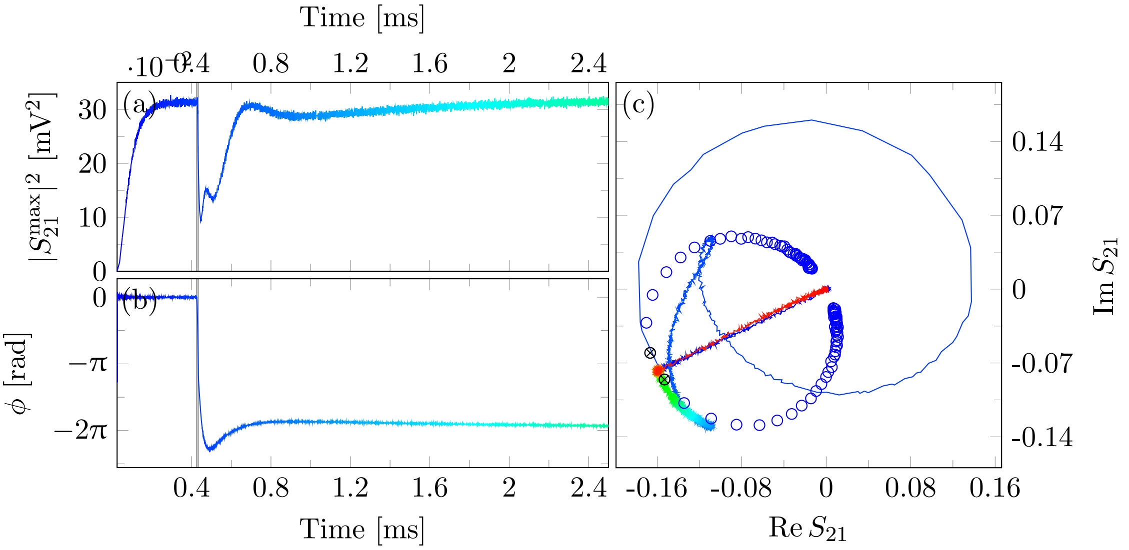

Figure 8.10.: Measurement for a 8 µs with a very high laser power of 3.5 mW. (a) The excitation of quasiparticles causes a decrease of the amplitude, but we also see shifts in the other direction possibly coming from TLF effects. (b) The emerging dip we mentioned in the caption of Fig. 8.9 has become a phase shift of 2π. As we have already noted before, the reason for this phase rotation is not yet clear. A fit of the quasiparticle relaxation time yields a similar value to the previous measurements with lower power $\tau_{\mathrm{qp}} \approx 2.8\,\mathrm{ms}$.

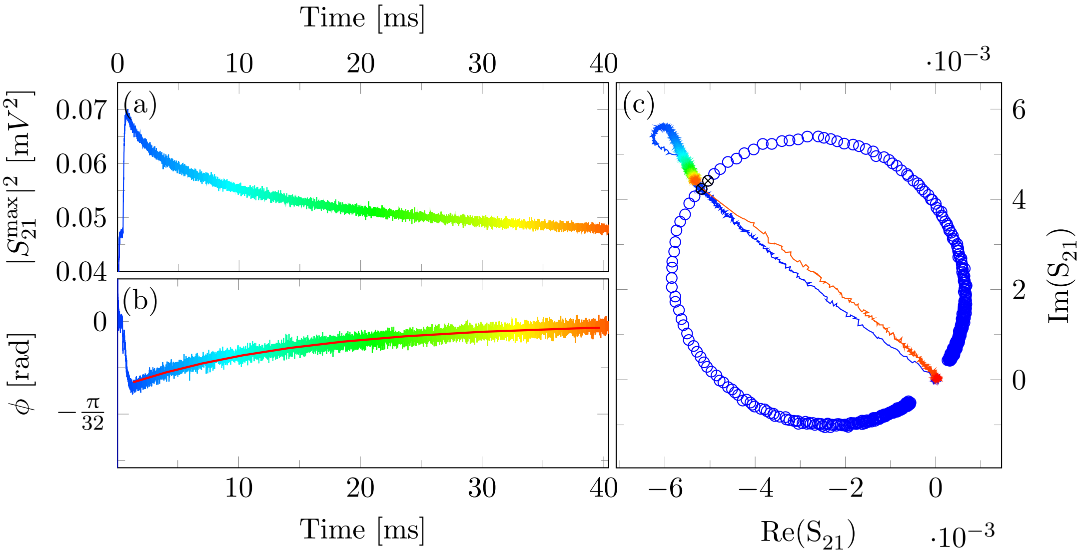

Figure 8.11.: Time-dependent measurement of the amplitude and phase at the resonance frequency f_0 for a 32 µs laser pulse with a power of 260 nW. (a) The amplitude shows an increase due to the excitation of two-level fluctuators. The reason is that TLFs constitute the main loss mechanism at low temperatures. (b) The phase shows a complex behavior that is better visualized in Fig. 8.12 or also in (c). The fit (red) yields a lifetime of about 15 ms.

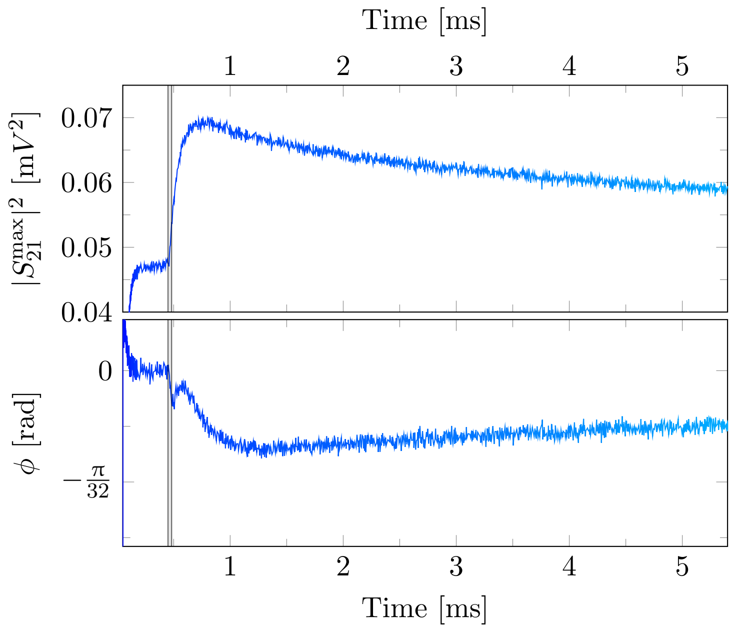

Figure 8.12.: Magnification of Fig. 8.11 which features the resonator response to a 32 µs laser pulse with 260 nW. The gray area shows again the duration or the pulse.

A typical measurement in this regime can be seen in Fig. 8.11 and 8.12 Those plots show the consequences of a 32 µs pulse. By now we are familiar with the increasing amplitude due to TLF effects. The phase illustrates a more complex behavior caused by the upward shift of the overall resonance frequency[18] due to TLFs with a resonance frequency greater than the resonator $f_0^{\mathrm{TLF}} > f_0$ and the downward shift of the overall resonance frequency due to TLFs with a resonance frequency smaller than the resonator $f_0^{\mathrm{TLF}} < f_0$. Figure 8.12 shows first a decreasing phase, then a small increase followed by another decrease and then a final relaxation back to the equilibrium. An exponential fit of this last part gives a two-level fluctuator lifetime of $\overline{\tau}_{\mathrm{TLF}} \approx 15.4$ ms. A bit of caution may be advisable regarding this value since there are definitely many different TLFs with different resonance frequencies and lifetimes in our sample. So this lifetime should be considered more of an average value for the different distributions of TLFs. For different pulse lengths from 8 µs to 64 µs average lifetimes in the range of 10.6 ms to 25.5 ms have been extracted from exponential fits.

Interestingly, for pulse lengths above 64 µs the phase shift looks very similar to the high power measurements with 170 µW. The calculated lifetimes of 1 ms to 3 ms agree with the quasiparticle relaxation times. It seems that by irradiating long enough we are able to excite a sufficient amount of quasiparticles so that they become the dictating

---

[18] It is important to note that an upward shift of the resonance frequency causes a negative phase shift, while a shift to lower resonance frequencies results in a positive phase shift.

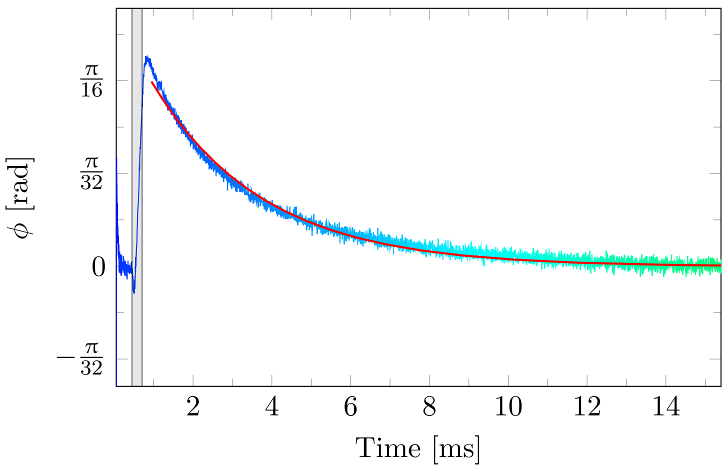

Figure 8.13.: A long pulse (256 µs) at low laser power (260 nW) can yield similar results to a short pulse with high power. An exponential fit gives a lifetime of about 2.8 ms which is almost the same result as for a fit of Fig. 8.4.

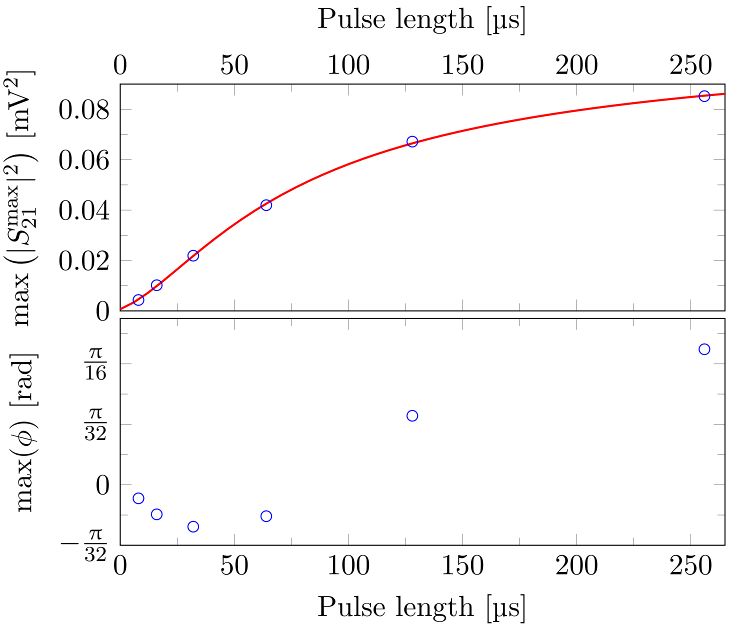

Figure 8.14.: A plot of the maximum amplitude and phase shift for different pulse lengths for a small laser power (260 nW). An explanation of the plot can be found in the caption of Fig. 8.7.

Table 8.3.: Energetically equivalent pulses.

	$\max(\phi)$ [rad]	$\max\left(\lvert S_{21}^{\max}\rvert^2\right)$ [a. u.]
$P_{\mathrm{lp}} = 160\,\mu\mathrm{W},\ t_{\mathrm{pl}} = 0.5\,\mu\mathrm{s}$	0.1137	0.397
$P_{\mathrm{lp}} = 80\,\mu\mathrm{W},\ t_{\mathrm{pl}} = 1\,\mu\mathrm{s}$	0.038	0.175
$P_{\mathrm{lp}} = 160\,\mu\mathrm{W},\ t_{\mathrm{pl}} = 1\,\mu\mathrm{s}$	0.1418	0.489
$P_{\mathrm{lp}} = 80\,\mu\mathrm{W},\ t_{\mathrm{pl}} = 2\,\mu\mathrm{s}$	0.0441	0.203

process once again.

The maximum amplitude shift and the maximum phase shift caused by different pulse lengths are summed up in Fig. 8.14. Like before[19] the amplitude response can accurately be described with the TLF model. The maximum phase shift $\max(\phi)$ nicely shows shows the transition from the TLF governed regime to the regime where quasiparticle excitations play the dominant role.

First the TLFs cause a negative phase shift and then when quasiparticle excitation effects start to become more important a shift in the opposite direction can be observed.

In light of these results we also wanted to test if maybe it isn't so much the pulse power but rather the total energy deposited that is important. Or in other words, does a pulse A of length $t_{\mathrm{pl}}^{A} = a$ and power $P_{\mathrm{lp}}^{A} = b$ have the same effect as a pulse B twice as long $t_{\mathrm{pl}}^{B} = 2a$ but with only half the power $P_{\mathrm{lp}}^{B} = b/2$?

The short answer to this is no, we find that a short pulse with a higher power has a larger effect than an "equivalent" pulse with twice the pulse length but half the power. The measurement results are summarized in Table 8.3.

---

[19] See Fig. 8.8.

9. Summary and Outlook

In the course of this thesis we have treated the fundamentals of superconducting coplanar waveguide (CPW) resonators, outlined the experimental setup and measurement processes and finally discussed the measurement results in the last chapter. We will now conclude with a short summary of the most important results and a brief glimpse at current and future developments regarding the topics of this thesis.

The purpose of this work was to investigate the properties of superconducting CPW resonators exposed to continuous and pulsed light irradiation. The resonator response to perturbations is mostly determined by two-level fluctuators (TLFs) and quasiparticle excitations. Roughly speaking, the former govern the behavior for small perturbations while the latter dictate the response caused by strong perturbations.

For small laser powers (0 nW to 50 nW) and continuous irradiation the frequency response shows the characteristic shape expected from TLF excitations. The same is true for the quality factor which exhibits a significant increase due to the saturation of TLFs, thereby removing the leading loss mechanism at low temperatures. A fit to the formulas derived from the standard two-level system model, which have been modified to be dependent on light power rather than on temperature, yields very good agreement for the quality factor but is unsuccessful for the frequency shift.

Continuous irradiation with higher laser powers (~0.2 µW to 170 µW) illustrates the transition from a regime governed by TLFs to one determined by quasiparticle excitations. Above 100 µW a linear decrease of the resonance frequency shift is observed, due to the fact that the shift is proportional to the quasiparticle density which in turn is directly proportional to the optical power. The response of the quality factor to quasiparticle excitations on the other hand is indirectly proportional to quasiparticle excitations and therefore also the laser power. The quality factor can be fitted with a single function, composed of a part describing the TLF response and a second part for quasiparticle excitations, over the full range of optical powers.

Concerning the perturbations of the resonance frequency we found that the maximum magnitude of the frequency shifts is on the order of a few kHz for two-level fluctuator effects and about 65 kHz for quasiparticle excitations.

Furthermore the resonator response to different microwave probing powers and temperature changes was measured and compared to the measurements with continuous laser irradiation. The experimental results in the limited range of microwave probing powers and temperatures considered by us is consistent with TLF effects.

Pulsed light measurements have been carried out for various optical powers and pulse lengths. From these measurements a quasiparticle lifetime of $\tau_{\mathrm{qp}} \approx 2\,\mathrm{ms}$ and an average TLF lifetime of $\overline{\tau}_{\mathrm{TLF}} \approx 15\,\mathrm{ms}$ was extracted. To our knowledge the time-dependent response of a CPW resonator to optically excited two-level fluctuators has been measured for the first time. For low (260 nW) as well as high (170 µW) optical powers the maximum shift of the amplitude at the equilibrium resonance frequency as a function of the pulse length shows a behavior consistent with the TLF excitations. In case of high powers the maximum phase shift follows a positive linear slope caused by quasiparticle excitations, while for low powers first TLFs are responsible for a negative phase shift which is then turned around by quasiparticle effects for pulse lengths greater than 40 µs. The low power behavior shows that it is possible to control the amount of quasiparticle excitations compared to TLF excitations via the pulse duration.

Finally we were able to prove that two pulses with the same energy but different pulse lengths (and therefore different powers) won't cause the same resonator response. A shorter pulse with higher power will be more effective than an energetically equivalent longer pulse with lower power.

This last result brings us back into the present and to the current state of the experiment. When we started the experiments, which are now collected in this master thesis, the optical measurements and the NV^- measurements were two separate experiments. At the moment we have just begun to conduct the first measurements of a resonator with a diamond on top where we try to polarize the NV^-centers with the laser, thus merging the two experiments into a single one.

Another interesting continuation of the work from this thesis, that hopefully will be done some time in the near future, would be the exchange of the simple planar terminated fiber with a lensed fiber. The big advantage would be the ability to locally probe a small number of two-level fluctuators and investigate their characteristics and spatial distribution.

The understanding of superconducting microwave resonators as well as their applications have seen substantial progress over the past years, many questions remain and many new ones opened up. Personally, it will be very interesting to see the future progress and the significance of superconducting microwave resonators, especially in the field of quantum information processing, in the years to come.

Appendix

A. Maxwell's equations in matter

$$\nabla \cdot \boldsymbol{D} = \rho\,, \tag{A.1}$$

$$\nabla \times \boldsymbol{E} = -\frac{\partial \boldsymbol{B}}{\partial t}\,, \tag{A.2}$$

$$\nabla \cdot \boldsymbol{B} = 0\,, \tag{A.3}$$

$$\nabla \times \boldsymbol{H} = \boldsymbol{J} + \frac{\partial \boldsymbol{D}}{\partial t}\,, \tag{A.4}$$

where ρ is the free charge density, $\boldsymbol{J}$ the free current density, $\boldsymbol{D} = \epsilon \boldsymbol{E}$ and $\boldsymbol{B} = \mu \boldsymbol{H}$.

B. Impedance - parallel resonant circuit

Near the resonance frequency, where $\omega = \omega_0 + \Delta\omega$ and $\omega_0 = 1/\sqrt{LC}$ the last term of Eq. (3.1) can be expanded for small $\Delta\omega$

$$\begin{aligned}
Z(\omega) &= \left(\frac{1}{R} + \mathrm{j}(\omega_0 + \Delta\omega)C + \frac{1}{\mathrm{j}(\omega_0 + \Delta\omega)L}\right)^{-1} && \text{(B.1)}\\
&= \left(\frac{1}{R} + \mathrm{j}(\omega_0 + \Delta\omega)C + \frac{1}{\mathrm{j}\omega_0 L}\frac{1}{1 + \Delta\omega/\omega_0}\right)^{-1} && \text{(B.2)}\\
&\approx \left(\frac{1}{R} + \mathrm{j}(\omega_0 + \Delta\omega)C + \frac{1}{\mathrm{j}\omega_0 L}\left(1 - \Delta\omega/\omega_0 + \dots\right)\right)^{-1} && \text{(B.3)}\\
&= \left(\frac{1}{R} + \mathrm{j}(\omega_0 + \Delta\omega)C - \mathrm{j}\omega_0 C + \mathrm{j}\Delta\omega C\right)^{-1} && \text{(B.4)}\\
&= \frac{R}{1 + 2\mathrm{j}\Delta\omega RC} = \frac{R}{1 + 2\mathrm{j}Q_{\mathrm{int}}\Delta\omega/\omega_0} && \text{(B.5)}
\end{aligned}$$

Equation (B.5) also delivers us a link between the fractional bandwidth BW_{frac} and the quality factor of the resonator. The fractional bandwidth is defined by the two points in frequency $\frac{\omega_1}{\omega_0}$ and $\frac{\omega_2}{\omega_0}$ where the real power delivered to the circuit is divided in half: $BW_{\mathrm{frac}} = \frac{\Delta\omega_{\mathrm{FWHM}}}{\omega_0}$, where $\Delta\omega_{\mathrm{FWHM}} = 2\Delta\omega = \omega_2 - \omega_1$ is now the full width at half maximum (see Fig. 3.2). According to Eq. (3.2) the dissipated power is given by

$$P_{\mathrm{loss}}(\omega) = \frac{1}{2}\frac{|V|^2}{R} = \frac{1}{2}\frac{|I|^2|Z|^2}{R}\,, \tag{B.6}$$

so the half power points are occur at $|Z|^2 = R^2/2$. Combined with Eq. (B.5) we get

$$\frac{R^2}{2} = \left|\frac{R}{1 + \mathrm{j}Q_{\mathrm{int}}\Delta\omega_{\mathrm{FWHM}}/\omega_0}\right|^2 \tag{B.7}$$

$$\frac{R^2}{2} = \frac{R^2}{1 + Q_{\mathrm{int}}^2(\Delta\omega_{\mathrm{FWHM}}/\omega_0)^2} \tag{B.8}$$

$$2 = 1 + Q_{\mathrm{int}}^2\left(\frac{\Delta\omega_{\mathrm{FWHM}}}{\omega_0}\right)^2 \tag{B.9}$$

$$Q_{\mathrm{int}} = \frac{\omega_0}{\Delta\omega_{\mathrm{FWHM}}} = \frac{1}{BW_{\mathrm{frac}}} \tag{B.10}$$

C. Lumped element and transmission line parameters for a half wave resonator

The comparison of Eq. (3.9) and Eq. (3.11) directly leads to

$$R = \frac{Z_0}{\alpha l}\,, \quad C = \frac{\pi}{2\omega_0 Z_0}\,, \tag{C.1}$$

and the inductance close to resonance can be found from Eq. (3.5)

$$L = \frac{1}{\omega_0^2 C}\,. \tag{C.2}$$

With the assumption of a low-loss transmission line the characteristic impedance is given by $Z_0 \approx \sqrt{L_l/C_l}$ and by expanding Eq. (2.5) the propagation constant becomes $\beta \approx \omega\sqrt{L_l C_l}$. So the phase velocity is $v_{\mathrm{p}} = \frac{\omega}{\beta} \approx \frac{1}{\sqrt{L_l C_l}}$ and $\omega_0 = 2\pi f = 2\pi\frac{v_{\mathrm{p}}}{\lambda} = \frac{2\pi}{2l\sqrt{L_l C_l}}$. Inserting these relations into Eq. (C.1) and (C.5) gives

$$R = \frac{Z_0}{\alpha l}\,, \quad C = \frac{C_l l}{2}\,, \quad L = \frac{2L_l l}{\pi^2}\,. \tag{C.3}$$

The Taylor expansion of Eq. (2.5) also relates α with Z_0, R_l and G_l

$$\alpha \simeq \frac{1}{2}\left(\frac{R_l}{Z_0} + G_l Z_0\right)\,. \tag{C.4}$$

For higher modes with frequencies $\omega_n = n\omega_0$ one can introduce a mode-dependent inductance L_n so that Eq. (C.5) reads

$$L = \frac{1}{\omega_n^2 C} = \frac{2L_l l}{n^2\pi^2}\,. \tag{C.5}$$

D. Complex conductivity in the Drude model

We start from the Drude model for metals which assumes a free electron gas

$$m\frac{\mathrm{d}\boldsymbol{v}}{\mathrm{d}t} = e\boldsymbol{E} - \frac{m\boldsymbol{v}}{\tau}\,, \tag{D.1}$$

where m is the mass of the electron, v the drift velocity, e the elementary charge, E the electric field and τ a phenomenological relaxation time. By multiplying with the charge density n and the electron charge e the drift velocity can be replaced by the current density $\boldsymbol{J} = ne\boldsymbol{v}$. With the conjecture of a periodic field $\boldsymbol{E} = \boldsymbol{E_0}\mathrm{e}^{\mathrm{j}\omega t}$ and a linear response $\boldsymbol{J} = \boldsymbol{J_0}\mathrm{e}^{\mathrm{j}\omega t}$ Eq. (D.1) yields

$$\boldsymbol{J} = \frac{ne^2\tau}{m}\frac{\boldsymbol{E}}{1+\mathrm{j}\omega\tau} = \sigma(\omega)\boldsymbol{E}\,, \tag{D.2}$$

where $\sigma(\omega) = \sigma_1(\omega) - \mathrm{j}\sigma_2(\omega)$ is the complex conductivity. In the two-fluid model a superconductor can be described as a superposition of a normal and a superconducting fluid so that $\boldsymbol{J_{\mathrm{tot}}} = \boldsymbol{J_{\mathrm{n}}} + \boldsymbol{J_{\mathrm{s}}}$ and

$$\sigma_{1,i} = \sigma_{0,i}\frac{1}{1+\omega^2\tau_i^2}\,, \tag{D.3}$$

$$\sigma_{2,i} = \sigma_{0,i}\frac{\omega\tau_i}{1+\omega^2\tau_i^2}\,, \tag{D.4}$$

with $\sigma_{0,i} = \frac{n_i e^2 \tau_i}{m}$ and $i = \mathrm{n}, \mathrm{s}$. Superconducting electrons can be characterized via $\tau_{\mathrm{s}} \to \infty$ and for the normal conducting electrons we can usually assume $\omega\tau_{\mathrm{n}} \ll 1$ at microwave frequencies [AM76]. This lets us approximate the real and imaginary part of the total complex conductivity with

$$\sigma_1 = \frac{\pi n_{\mathrm{s}} e^2}{2m}\delta(\omega) + \frac{n_{\mathrm{n}} e^2 \tau_{\mathrm{n}}}{m}\,, \tag{D.5}$$

$$\sigma_2 = \frac{n_{\mathrm{s}} e^2}{m\omega}\,. \tag{D.6}$$

The derivation of Eq. (D.5) and (D.6) can be found in Tinkham [Tin96].

E. Kinetic inductance of a wire

The energy stored by a normal conducting wire carrying a current I with a length l and a cross-sectional area A consists of the energy stored inside the magnetic field plus the kinetic energy of the electrons [MT69]

$$E_{\mathrm{tot}} = E_{\mathrm{m}} + E_{\mathrm{kin}} = \int_{\text{all space}} \frac{\mu}{4}|\boldsymbol{H}|^2\,\mathrm{d}V + \int_{\text{wire}} \frac{1}{2} n_{\mathrm{n}} m v^2\,\mathrm{d}V\,, \tag{E.1}$$

where μ is the permeability, $\boldsymbol{H}$ the magnetic field, n_n the electron density, m the electron mass and v is the drift velocity of the electrons. From circuit theory we know that the first integral may be expressed as

$$E_\mathrm{m} = \frac{1}{2} L_\mathrm{m} I^2 \,, \tag{E.2}$$

with the magnetic inductance L_m. Inserting $I = n_\mathrm{n} e v A$, where e is the elementary electric charge, and $\mathrm{d}V = \mathrm{d}l\,\mathrm{d}A$ into the second integral allows us to write the kinetic energy in a similar form

$$E_\mathrm{kin} = \frac{1}{2} \frac{m}{n_\mathrm{n} e^2} \frac{l}{A} I^2 = \frac{1}{2} L_\mathrm{ki} I^2 \,. \tag{E.3}$$

The same derivation can be done for a superconducting wire, but we just have to replace the mass m with the mass of the superconducting charge carriers $m_\mathrm{s} = 2m$ and the charge e with $2e$ in Eq. (E.3) to get the correct result.

To see the influence of the kinetic inductance we will take a closer look at Eq. (D.2). Dividing by σ, multiplying with the length l of the wire and integrating over the cross-sectional area A of the wire yields

$$\int (1 + \mathrm{j}\omega\tau) \frac{ml}{n_\mathrm{n} e^2 \tau} \boldsymbol{J} \,\mathrm{d}\boldsymbol{A} = \int \boldsymbol{E} l \,\mathrm{d}\boldsymbol{A} \,, \tag{E.4}$$

$$(1 + \mathrm{j}\omega\tau) \frac{ml}{n_\mathrm{n} e^2 \tau} I = ElA = VA \,, \tag{E.5}$$

$$\left[\frac{m}{n_\mathrm{n} e^2 \tau} \frac{l}{A} + \mathrm{j}\omega \frac{m}{n_\mathrm{n} e^2} \frac{l}{A} \right] I = V \,, \tag{E.6}$$

$$(R + \mathrm{j}\omega L_\mathrm{ki}) I = Z \cdot I = V \,. \tag{E.7}$$

In the last step we arrived at the complex generalization of Ohm's law.

For normal metals the relaxation time τ at room temperature is on the order of picoseconds so the resistive term dominates strongly unless we have very high frequencies ($> 10\,\mathrm{THz}$). This is the reason why kinetic inductance usually doesn't play a significant role in normal metals. In other words, the resistance causes scattering of the electrons, which in turn keeps the drift velocity v and thereby also the kinetic inductance small.

Superconductors on the other hand can be described by $\tau \to \infty$ in this simple picture. By performing this limit we immediately see that kinetic inductance can become the dominating part of the impedance.

It is important to note, that for a fixed superconducting current I the kinetic inductance has its greatest value directly below the critical temperature T_c. This follows from the fact that the velocity v enters quadratically into Eq. (E.1). Near the critical temperature a small number of high velocity Cooper pairs has to sustain the fixed supercurrent I, whereas at lower temperatures the Cooper pair density increases while the the average velocity decreases.

F. Pauli matrices

$$\sigma_x = \begin{pmatrix} 0 & 1 \\ 1 & 0 \end{pmatrix} , \quad \sigma_y = \begin{pmatrix} 0 & -\mathrm{j} \\ \mathrm{j} & 0 \end{pmatrix} \quad \text{and} \quad \sigma_z = \begin{pmatrix} 1 & 0 \\ 0 & -1 \end{pmatrix} \tag{F.1}$$

G. Phase and amplitude perturbation

We begin by separating Eq. (3.25) into real and imaginary part while only considering the first order

$$\begin{aligned} S_{21} &= \frac{1}{(1/S_{21}^{\max})^2 + 4Q_{\text{tot}}^2 \delta\omega_0/\omega_0} \left[1 + 2\mathrm{j}Q_{\text{tot}}\frac{\delta\omega_0}{\omega_0}\right] \left[\frac{1}{S_{21}^{\max}} - 2\mathrm{j}Q_{\text{tot}}\frac{\delta\omega_0}{\omega_0}\right] && \text{(G.1)} \\ &\approx (S_{21}^{\max})^2 \left[\frac{1}{S_{21}^{\max}} + \frac{1}{S_{21}^{\max}} 2\mathrm{j}Q_{\text{tot}}\frac{\delta\omega_0}{\omega_0} - 2\mathrm{j}Q_{\text{tot}}\frac{\delta\omega_0}{\omega_0}\right] && \text{(G.2)} \\ &\approx S_{21}^{\max} + S_{21}^{\max}(1 - S_{21}^{\max}) 2\mathrm{j}Q_{\text{tot}}\frac{\delta\omega_0}{\omega_0} \,. && \text{(G.3)} \end{aligned}$$

With this we can calculate small phase changes

$$\tan\phi \approx \phi = (1 - S_{21}^{\max}) 2Q_{\text{tot}}\frac{\delta\omega_0}{\omega_0} \,. \tag{G.4}$$

For perturbations of the resonance we assume that close to resonance the real part of S_{21} is much larger than the imaginary part so that

$$A = \sqrt{\mathrm{Re}(S_{21})^2 + \mathrm{Im}(S_{21})^2} \approx \mathrm{Re}(S_{21}) \,. \tag{G.5}$$

On resonance $\mathrm{Re}(S_{21}) = S_{21}^{\max}$, as can be seen from Eq. (3.24). Calculating the amplitude change δA for small variations $\delta Q_{\text{int}}^{-1}$ from this directly gives the result of Eq. (5.22).

Bibliography

[AHV72] Phillip W. Anderson, Bertrand I. Halperin, and Chandra M. Varma. "Anomalous Low-Temperature Thermal Properties of Glasses and Spin Glasses". In: *Philosophical Magazine* 25.1 (1972), pp. 1–9. DOI: `10.1080/14786437208229210` (cit. on pp. 26, 27).

[AM76] Neil W. Ashcroft and Nathanial D. Mermin. *Solid State Physics*. Science: Physics. Saunders College, 1976. ISBN: 978-0-03083-993-1 (cit. on pp. 22, 66).

[Ams12] Robert Amsüss. "Strong Coupling of a NV Spin Ensemble to a Superconducting Resonator". PhD thesis. Vienna University of Technology, 2012 (cit. on pp. 2, 10, 32).

[AS64] Milton Abramowitz and Irene A. Stegun. *Handbook of Mathematical Functions: With Formulars, Graphs, and Mathematical Tables*. Applied mathematics series. New York : Dover Publications, 1964. ISBN: 978-0-48661-272-0 (cit. on pp. 14, 19, 29).

[Bal07] Nicholas H. Balshaw. *Practical Cryogenics – An Introduction to Laboratory Cryogenics*. Oxford Instruments NanoScience, 2007 (cit. on p. 32).

[Bar+08] Rami Barends et al. "Quasiparticle Relaxation in Optically Excited High-Q Superconducting Resonators". In: *Phys. Rev. Lett.* 100 (25 June 2008), p. 257002. DOI: `10.1103/PhysRevLett.100.257002` (cit. on pp. 22, 54).

[Bar09] Rami Barends. *Photon-detecting Superconducting Resonators*. Casimir PhD Series, Delft-Leiden. Barends, 2009. ISBN: 978-9-08593-052-5 (cit. on pp. 19, 23).

[BCS57] John Bardeen, Leon N. Cooper, and John R. Schrieffer. "Theory of Superconductivity". In: *Phys. Rev.* 108 (5 Dec. 1957), pp. 1175–1204. DOI: `10.1103/PhysRev.108.1175` (cit. on pp. 17, 19).

[Blo46] Felix Bloch. "Nuclear Induction". In: *Physical Review* 70.7-8 (1946), pp. 460–474 (cit. on p. 29).

[CC97] Erli Chen and Stephen Y. Chou. "Characteristics of Coplanar Transmission Lines on Multilayer Substrates: Modeling and Experiments". In: *Microwave Theory and Techniques, IEEE Transactions on* 45.6 (1997), pp. 939–945. ISSN: 0018-9480. DOI: `10.1109/22.588606` (cit. on p. 13).

[Col92] Robert E. Collin. *Foundations for Microwave Engineering*. An IEEE Press classic reissue. Wiley, 1992. ISBN: 978-0-78036-031-0 (cit. on p. 21).

[Day+03] Peter K. Day et al. “A Broadband Superconducting Detector suitable for Use in Large Arrays”. In: *Nature* 425.6960 (2003), pp. 817–821. DOI: `10.1038/nature02037` (cit. on pp. 7, 23).

[DiV00] David P. DiVincenzo. “The Physical Implementation of Quantum Computation”. In: *Fortschritte der Physik* 48.9-11 (2000), pp. 771–783. ISSN: 1521-3978. DOI: `10.1002/1521-3978(200009)48:9/11<771::AID-PROP771>3.0.CO;2-E` (cit. on p. 1).

[Esq98] Pablo Esquinazi. *Tunneling Systems in Amorphous and Crystalline Solids.* Springer, 1998. ISBN: 978-3-54063-960-2 (cit. on p. 26).

[Fin10] Johannes M. Fink. “Quantum Nonlinearities In Strong Coupling Circuit QED”. PhD thesis. ETH Zürich, 2010 (cit. on p. 37).

[Fru+05] Luigi Frunzio et al. “Fabrication and Characterization of Superconducting Circuit QED Devices for Quantum Computation”. In: *Applied Superconductivity, IEEE Transactions on* 15.2 (2005), pp. 860–863. ISSN: 1051-8223. DOI: `10.1109/TASC.2005.850084` (cit. on p. 15).

[Gao+08a] Jiansong Gao et al. “Equivalence of the Effects on the Complex Conductivity of Superconductor due to Temperature Change and External Pair Breaking”. In: *Journal of Low Temperature Physics* 151.1-2 (2008), pp. 557–563 (cit. on p. 23).

[Gao+08b] Jiansong Gao et al. “Experimental Evidence for a Surface Distribution of Two-Level Systems in Superconducting Lithographed Microwave Resonators”. In: *Applied Physics Letters* 92.15, 152505 (2008), p. 152505. DOI: `10.1063/1.2906373` (cit. on pp. 26, 27).

[Gao08] Jiansong Gao. “The Physics of Superconducting Microwave Resonators”. PhD thesis. California Institute of Technology, 2008 (cit. on pp. 13, 15–20, 23, 25, 26, 29, 30, 39).

[Göp+08] Martin Göppl et al. “Coplanar Waveguide Resonators for Circuit Quantum Electrodynamics”. In: *Journal of Applied Physics* 104.11, 113904 (2008), p. 113904. DOI: `10.1063/1.3010859` (cit. on p. 10).

[Gra75] Kenneth E. Gray. “ISS Depth Profile Analysis of Anodized Niobium”. In: *Applied Physics Letters* 27.8 (1975), pp. 462–464. DOI: `10.1063/1.88528` (cit. on p. 26).

[Gro96] Lov K. Grover. “A Fast Quantum Mechanical Algorithm for Database Search”. In: *Proceedings of the Twenty-eighth Annual ACM Symposium on Theory of Computing.* ACM, 1996, pp. 212–219. DOI: `10.1145/237814.237866` (cit. on p. 1).

[HA76] Siegfried Hunklinger and W. Arnold. In: *Physical Acoustics Vol. XII* (1976). Ed. by W. P. Mason and R. N. Thurston (cit. on p. 27).

[Ham11] Gerd Hammer. *Untersuchung der Eigenschaften von planaren Mikrowellenresonatoren für Kinetic-Inductance Detektoren bei 4,2 K*. KIT Scientific Publishing, 2011. ISBN: 978-3-86644-715-8 (cit. on p. 15).

[Her96] Heinrich Hertz. *Miscellaneous Papers*. Macmillan, 1896 (cit. on p. 16).

[Kap+76] Steven B. Kaplan et al. "Quasiparticle and Phonon Lifetimes in Superconductors". In: *Phys. Rev. B* 14 (11 Dec. 1976), pp. 4854–4873. DOI: `10.1103/PhysRevB.14.4854` (cit. on pp. 53, 54).

[Kol12] Christian Koller. "Towards the Experimental Realization of Hybrid Quantum Systems". PhD thesis. Vienna University of Technology, 2012 (cit. on pp. 13, 14, 32, 36, 46).

[Lis+10] Jürgen Lisenfeld et al. "Rabi Spectroscopy of a Qubit-Fluctuator System". In: *Phys. Rev. B* 81 (10 Mar. 2010), p. 100511. DOI: `10.1103/PhysRevB.81.100511` (cit. on p. 26).

[LL35] Fritz London and Heinz London. "The Electromagnetic Equations of the Supraconductor". In: *Proceedings of the Royal Society of London. Series A - Mathematical and Physical Sciences* 149.866 (1935), pp. 71–88. DOI: `10.1098/rspa.1935.0048` (cit. on p. 16).

[LS74] Ingolf Lindau and William E. Spicer. "Oxidation of Nb as studied by the UV-Photoemission Technique". In: *Journal of Applied Physics* 45.9 (1974), pp. 3720–3725. DOI: `10.1063/1.1663849` (cit. on p. 26).

[Mac+10] Pascal Macha et al. "Losses in Coplanar Waveguide Resonators at Millikelvin Temperatures". In: *Applied Physics Letters* 96.6, 062503 (2010), p. 062503. DOI: `10.1063/1.3309754` (cit. on p. 46).

[Maj+07] Johannes Majer et al. "Coupling Superconducting Qubits via a Cavity Bus". In: *Nature* 449.7161 (2007), pp. 443–447. DOI: `10.1038/nature06184` (cit. on p. 7).

[Maz04] Benjamin A. Mazin. "Microwave Kinetic Inductance Detectors". PhD thesis. California Institute of Technology, 2004 (cit. on pp. 23, 25).

[MB58] Daniel. C. Mattis and John Bardeen. "Theory of the Anomalous Skin Effect in Normal and Superconducting Metals". In: *Phys. Rev.* 111 (2 July 1958), pp. 412–417. DOI: `10.1103/PhysRev.111.412` (cit. on pp. 17, 19).

[MT69] Robert Meservey and Paul M. Tedrow. "Measurements of the Kinetic Inductance of Superconducting Linear Structures". In: *Journal of Applied Physics* 40.5 (1969), pp. 2028–2034. DOI: `10.1063/1.1657905` (cit. on pp. 15, 16, 66).

[NC10] Michael A. Nielsen and Isaac L. Chuang. *Quantum Computation and Quantum Information: 10th Anniversary Edition*. Cambridge University Press, 2010. ISBN: 978-1-13949-548-6 (cit. on p. 1).

[Nöb13] Tobias Nöbauer. "Sensing, Coherent Coupling and Optimal Control with Nitrogen-Vacancy Colour Centres in Diamond". PhD thesis. Vienna University of Technology, 2013 (cit. on p. 2).

[Nor12] Omid Noroozian. "Superconducting Microwave Resonator Arrays for Submillimeter/Far-Infrared Imaging". PhD thesis. California Institute of Technology, 2012 (cit. on p. 23).

[PA98] Paul J. Petersan and Steven M. Anlage. "Measurement of Resonant Frequency and Quality Factor of Microwave Resonators: Comparison of Methods". In: *Journal of Applied Physics* 84.6 (1998), pp. 3392–3402. DOI: `10.1063/1.368498` (cit. on p. 39).

[Phi72] William A. Phillips. "Tunneling States in Amorphous Solids". English. In: *Journal of Low Temperature Physics* 7 (3-4 1972), pp. 351–360. ISSN: 0022-2291. DOI: `10.1007/BF00660072` (cit. on pp. 26, 27).

[Phi87] William A. Phillips. "Two-Level States in Glasses". In: *Reports on Progress in Physics* 50.12 (1987), p. 1657 (cit. on pp. 27, 28, 46).

[Pip53] Alfred B. Pippard. "An Experimental and Theoretical Study of the Relation between Magnetic Field and Current in a Superconductor". In: *Proceedings of the Royal Society of London. Series A. Mathematical and Physical Sciences* 216.1127 (1953), pp. 547–568. DOI: `10.1098/rspa.1953.0040` (cit. on pp. 16, 17).

[Pöp89] Ralf Pöpel. "Electromagnetic Properties of Superconductors". English. In: *Superconducting Quantum Electronics*. Ed. by Volkmar Kose. Springer Berlin Heidelberg, 1989, pp. 44–78. ISBN: 978-3-64295-594-5. DOI: `10.1007/978-3-642-95592-1_3` (cit. on p. 17).

[Poz11] David M. Pozar. *Microwave Engineering*. Wiley, 2011. ISBN: 978-0-47063-155-3 (cit. on pp. 3, 6–8, 10, 11, 29).

[Rei00] Michael Reizer. "Electron-Electron Relaxation in Two-Dimensional Impure Superconductors". In: *Phys. Rev. B* 61 (10 Mar. 2000), pp. 7108–7117. DOI: `10.1103/PhysRevB.61.7108` (cit. on pp. 22, 54).

[Sag+11] Jeremy M. Sage et al. "Study of Loss in Superconducting Coplanar Waveguide Resonators". In: *Journal of Applied Physics* 109.6, 063915 (2011), p. 063915. DOI: `10.1063/1.3552890` (cit. on p. 26).

[Sch07] David I. Schuster. "Circuit Quantum Electrodynamics". PhD thesis. Yale University, 2007 (cit. on p. 37).

[Sho94] Peter W. Shor. "Algorithms for Quantum Computation: Discrete Logarithms and Factoring". In: *Foundations of Computer Science, 1994 Proceedings., 35th Annual Symposium on*. 1994, pp. 124–134. DOI: `10.1109/SFCS.1994.365700` (cit. on p. 1).

[Sim04] Rainee N. Simons. *Coplanar Waveguide Circuits, Components, and Systems.* Wiley Series in Microwave and Optical Engineering. Wiley, 2004. ISBN: 978-0-47146-393-1 (cit. on pp. 13, 14).

[Tin56] Michael Tinkham. “Energy Gap Interpretation of Experiments on Infrared Transmission through Superconducting Films”. In: *Phys. Rev.* 104 (3 Nov. 1956), pp. 845–846. DOI: `10.1103/PhysRev.104.845` (cit. on pp. 18, 22).

[Tin96] Michael Tinkham. *Introduction to Superconductivity.* McGraw Hill, 1996. ISBN: 978-0-07064-878-4 (cit. on pp. 16, 66).

[Wal+04] Andreas Wallraff et al. “Strong Coupling of a Single Photon to a Superconducting Qubit using Circuit Quantum Electrodynamics”. In: *Nature* 431.7005 (2004), pp. 162–167. DOI: `10.1038/nature02851` (cit. on p. 7).

[Wen+11] James Wenner et al. “Surface Loss Simulations of Superconducting Coplanar Waveguide Resonators”. In: *Applied Physics Letters* 99.11, 113513 (2011), p. 113513. DOI: `10.1063/1.3637047` (cit. on p. 26).

[Wen69] Cheng P. Wen. “Coplanar Waveguide, a Surface Strip Transmission Line Suitable for Nonreciprocal Gyromagnetic Device Applications”. In: *Microwave Symposium, 1969 G-MTT International.* 1969, pp. 110–115. DOI: `10.1109/GMTT.1969.1122668` (cit. on p. 12).

[Yos+95] Keiji Yoshida et al. “Evaluation of Magnetic Penetration Depth and Surface Resistance of Superconducting Thin Films using Coplanar Waveguides”. In: *Applied Superconductivity, IEEE Transactions on* 5.2 (1995), pp. 1979–1982 (cit. on p. 21).

[Zmu12] Jonas Zmuidzinas. “Superconducting Microresonators: Physics and Applications”. In: *Annual Review of Condensed Matter Physics* 3.1 (2012), pp. 169–214. DOI: `10.1146/annurev-conmatphys-020911-125022` (cit. on pp. 7, 23).

List of Figures

List of Tables